dCollection

공학박사 학위논문

연소기 내 연소특성 모사 및 불안정 원인 규명을 위한 해석적 연구

Numerical Investigation of Combustion

Characteristics aimed at Identifying the Cause of

Combustion Instability

2023년 8월

서울대학교 대학원

항공우주공학과

남 재 현

Numerical Investigation of Combustion Characteristics aimed at Identifying the Cause of Combustion Instability

지도교수 여 재 익

이 논문을 공학박사 학위논문으로 제출함

2023년 8월

서울대학교 대학원
항공우주공학과
남 재 현

남재현의 공학박사 학위논문을 인준함

2023년 8월

위 원 장 : _____

부위원장 : _____

위   원 : _____

위   원 : _____

위   원 : _____

Abstract

Numerical investigations are conducted on complex combustion systems to study combustion instabilities in the combustor. Three types of combustors, consisting of partially premixed gas turbine combustor, two premixed gas turbine combustors connected with cross-talk area, and the dual-mode scramjet combustor are numerically studied. Large-eddy simulations (LES) are performed for the high-fidelity simulation of the turbulent flames in the gas turbine combustors, and reduced-order simulations are performed for the dual-mode scramjet combustor. From the simulations, the characteristics and causes of instabilities in the combustors are intensely studied.

In the partially premixed combustor, the effects of hydrogen composition are investigated as a cause of combustion instability. To simulate hydrogen-enriched swirling flames in the gas turbine combustor, the LES turbulence model, finite-rate chemistry model, and turbulence-chemistry interaction model are implemented in the solver. Three different hydrogen compositions are employed, and the changes in flame structure and combustion instability are investigated. A comparison with the experimental data is conducted to validate the numerical results and good agreements are shown. The simulation results indicate that the flame structure is readily altered when changing the hydrogen composition. Due to the fast burning velocity and diffusivity of hydrogen, the flame structure becomes thicker and shorter with the increase of hydrogen. In certain hydrogen compositions, rigorous combustion instability is triggered and flame becomes highly unstable. In this unstable case, flame-vortex interaction appears as an unburnt mixture is periodically supplied into the near-wall recirculation zone, which results in heat release fluctuation in the combustor. It is also confirmed that the combustion instability dissipates when the hydrogen content or flow rate is changed, and flame-vortex interaction does not appear. Therefore, the change of swirl flame

structure and its interaction with recirculation zones causes intense heat release fluctuation, becoming the main factor in triggering combustion instability.

Further study is performed considering the fully premixed flame to investigate the role of premixedness and equivalence ratio on combustion instability. The simulation results demonstrate that the widely distributed premixed flame structures are shown, caused by the fuel injection direction. The mixing condition influenced triggering combustion instabilities in the combustor by inducing equivalence ratio fluctuation. The fluctuation of the equivalence ratio measured at the swirler shows similar spectra to the combustion instabilities in the combustor. Unstable mixing causes the formation of oscillating flame and heat release fluctuation. The equivalence ratio is fixed constant in the premixed combustion, and therefore, heat release fluctuation is suppressed, and combustion instability is not triggered inside the premixed combustor. Overall, two factors of hydrogen composition and mixing conditions are confirmed to cause heat release fluctuation, contributing to the thermoacoustic feedback mechanism in the combustor.

Simulations of flame transfer function excluding combustor acoustics are subsequently performed to clarify the role of fuel supply system−driven instability on the partially premixed combustor. Acoustically forced flame is considered, and forcing frequencies from 50 Hz to 400 Hz are implemented as a combustor inlet boundary condition. At a certain forcing frequency, a strong response of flame and flow is observed. Specifically, rotating vortices are generated at the swirler inlet and those appeared periodically due to the fuel feed line turbulence. The vortices block the flow supply entering the swirler, resulting in periodic fuel injection through the combustor. The oscillation frequency of vortices coincides with the maximum gain of the flame transfer function, implying the influence of internal instabilities in the fuel supply system caused the strong flow and flame response in the combustor. The simulation results of transfer function profiles are validated with the experimental data and good agreements are

confirmed.

Subsequently, the simulations are performed for the large-scale combustion system consisting of two premixed gas turbine combustors and a cross-talk area to investigate the interaction of two combustors and its effect on combustion instability. Both symmetric and asymmetric boundary conditions for each gas turbine are considered for explaining their effects on flame perturbation and instability mode during the operation. In the symmetric inlet condition of two combustors, a longitudinal mode combustion instability develops inside the combustors. A push-push mode occurred in the combustion system, which indicates that the instability phases in the two combustors are identical. In the asymmetric case, an inlet velocity pulsation with an opposite phase of combustion instability is applied, which results in the suppression of instability and the attenuation of acoustic energy transferred to the whole system through the cross-talk. The obtained results indicate the interaction between combustors and inlet symmetry affect the development and attenuation of combustion instabilities of a complex gas turbine system.

For the design and investigation of the dual-mode scramjet combustor, a novel one-dimensional combustion solver is developed. The developed solver is based on one-dimensional governing equations and includes models for combustion, mixing, and internal instabilities including ram-to-scram transition and thermal choking. The flight conditions are set as inputs of the solver and information on flow variables, thrust, and thermal choking are calculated as output. The simulation results show the change of thrust and combustion mode due to the equivalence ratio and flight condition. Validation of the solver is done by comparing 0-dimensional combustion results with reference, and further validation is planned with existing experimental data.

Table of Contents

LIST OF FIGURES

LIST OF TABLES

Nomenclature

p	Pressure
Q, q	Heat release rate
U, u	Velocity
ρ	Density
X	Mole fraction
Y	Mass fraction
T	Temperature
LES	Large eddy simulation
CI	Combustion instability
CFD	Computational fluid dynamics
FTF	Flame transfer function
CTF	Cold-flow transfer function
MFC	Mass flow controller
$slpm$	Standard liter per minute
NO_x	Nitrogen oxide
OH	Hydroxyl
PIV	Particle image velocimetry
$WALE$	Wall-adapting local eddy-viscosity
FFT	Fast Fourier transform
t	Time
y^+	Non-dimensional distance
K	Kelvin
f	Frequency
C	Progress variable
A	Cross-sectional area
M	Mach number
G	Mach number forcing function
γ	Ratio of specific heat
x	Axial spatial coordinate
$m_{i,added}$	Mass addition of fuel
c_p	Constant-pressure specific heat
w	Crocco's number
μs	Microsecond
AOA	Angle of attack

Overscripts

$\bar{}$	Averaged quantity
$\sim$	Favre-averaged quantity
$\cdot$	Time rate of change

Superscripts

| ' | Perturbation quantity |
| ° | Degree |

Overscripts

i, j	Index factor
mean	Mean value
z	Axial direction
r	Radial direction
t	Turbulence property

Preface

This thesis is based on the following publications and manuscripts.

Chapter 2
Jaehyun Nam, Younghun Lee, Seongpil Joo, Youngbin Yoon, and Jack J. Yoh, "Numerical analysis of the effects of the hydrogen composition on a partially premixed gas turbine combustor", *International Journal of Hydrogen Energy*, Vol. 44, 2019.

Jaehyun Nam, and Jack J. Yoh, "A numerical investigation of the effects of hydrogen addition on combustion instability inside a partially-premixed swirl combustor", *Applied Thermal Engineering*, Vol. 176, 2020.

Jaehyun Nam, and Jack J. Yoh, "On the influence of hydrogen composition and premixedness on turbulent flames in the gas turbine combustor", *In preparation*.

Chapter 3
Jaehyun Nam, and Jack J. Yoh, "Impact of fuel supply driven instability on the response of hydrogen-enriched methane-air partially premixed turbulent flames", *Combustion and Flame*, Vol. 245, 2022.

Chapter 4
Jaehyun Nam, and Jack J. Yoh, "Large eddy simulation of combustion instabilities in multiple combustors densely interacting with each other", *Applied Thermal Engineering,* Vol. 220, 2023.

Chapter 5
Jaehoon Yang, Jaehyun Nam, Sang-Hun Kang, and Jack J. Yoh, "Numerical investigation of dual mode ramjet combustor using quasi 1-dimensional solver", *Journal of the Korean Society for Aeronautical & Space Sciences,* Vol. 49, 2021.

Chapter 1. Introduction

Combustion instability has been a major concern in the propulsion systems such as rockets, gas turbines, and scramjet engines. Combustion instability primarily develops as non-linear interaction between heat release rate, acoustics, and flow fluctuations. Triggering combustion instabilities is not determined solely by a single factor like flame or acoustics. Rather, it is interrelated and numerous factors like flow turbulence, fuel-air mixing, and engine structure affect combustion instability feedback loops. Whether those interrelated factors trigger the instability in the combustor or stay in stable condition is depend on the phase of heat release rate and pressure fluctuation at the flame location. The stability criterion of combustion instability is proposed by lord Rayleigh and it shows the acoustic field and the heat fluctuation are enough to occur:

$$\oint p'Q'dt > 0 \tag{1}$$

where p' is pressure fluctuation and Q' is heat release rate fluctuation at the flame. The modeling and simulation of combustion instability is a challenging task since the complex effects like turbulence should be adequately calculated.

Numerical simulation of combustion instability is classified into two major methods. One is using the thermo-acoustic network model which only considers acoustic perturbations. In this model, mean flow is considered frozen and solved as a single parameter. The other is using high-fidelity CFD tools with a Large-eddy simulation (LES) turbulence model. LES calculates and shows detailed information on reactive flow, which possibly causes instabilities in combustion engines. LES of combustion instabilities have been carried out for decades, while the approach of the simulations is again divided into two approaches: one is full LES computing the self-excited combustion instabilities considering all non-linearities, and the second is computing flame transfer function (FTF) which

represents the dynamic heat release response of inlet velocity oscillations. The first method needs to implement all geometrical parts of the combustion systems in the simulation domain and use the compressible solver to naturally solve acoustics in the combustors. It requires massive computational costs, and therefore, hard to perform simulations in multiple conditions. The second method, which is called forced simulation, only simulates the dynamic responses of a flame excluding the acoustics of engines. The simulation of FTF is relatively easy to complete due to its lower cost and less complexity. FTF results from the simulation can be used as the input of thermo-acoustic network models, which provide the frequency and amplitude of combustion instability.

In the present thesis, both approaches are carried out to predict and find the causes of combustion instabilities in the gas turbine combustor. Hydrogen and hydrogen-enriched methane are considered a fuel, and the effects of hydrogen composition are mainly investigated. The target partially premixed gas turbine combustor was experimentally investigated and the flame structure was reported as a factor in triggering combustion instabilities. Based on previous findings and experimental data, the turbulent flame structures and combustion instabilities due to the hydrogen composition are simulated in chapter 2. The change in flame length and intensity are shown, and the results are validated with an experimental OH-chemiluminescence image. Flame fluctuation due to combustion instability and instability mode shifting are predicted from the simulations. The simulations are further expanded to premixed combustion, and the differences in flame structure and combustion instability with partially premixed combustion conditions are investigated. The factors triggering combustion instabilities consisting of flame-vortex interaction and equivalence ratio fluctuation are analyzed in chapter 2.

The FTF simulations are carried out in chapter 3 to find the cause of dynamic flame responses in the combustor by investigating hydrodynamic instabilities inside the fuel supply system. The simulation results show the rigorous flame response in a certain

forcing frequency, which is induced by oscillating vortices inside the fuel supply system.

In chapter 4, the multiple premixed combustors connected with the cross-talk area are considered to simulate combustion instability in the can-annular type combustion system, which is mainly used in the industrial gas turbine combustor. Interactions between combustors and those effects on developing and attenuating combustion instabilities are numerically studied.

In chapter 5, the one-dimensional simulation of supersonic and subsonic combustion in the dual-mode scramjet combustor using the novel reduced-order combustion solver. Through the simulations, disturbances that occurred during the combustion are numerically studied. Those disturbances include ram-to-scram transition and thermal choking, which should be considered in the design process of the hypersonic vehicle. Internal instabilities in the combustor consisting of mode transition, thermal choking phenomenon, and thrust variation are calculated depending on various flight conditions, and a discussion of them is conducted.

Chapter 2. Hydrogen−enriched partially premixed combustor: combustion instability

2.1. Background and objective

The demand for hydrogen (H_2) energy has gotten a lot of attention in the influence of environmental pollution and global warming issues worldwide. In 2015, Paris Agreement is adopted and all participating countries submitted low−carbon development plans. Since around a quarter of global energy is produced from industrial gas turbines [1], research on reducing pollutants from gas turbine combustors is essential. In this regard, developing fuel flexibility technology has become a major issue in gas turbine society to meet the carbon−neutral policy. The operation of a gas turbine using alternative fuels of H_2 or H_2−enriched gas is challenging but promises lower CO_2 emissions and higher efficiency of gas turbine combustor. Intense research has been conducted to replace conventional natural gas with H_2−enriched fuel as a future gas turbine energy source. However, using H_2−enriched fuels accompanies the problems of operability [2,3], storage [4], and NO_x emissions. The different chemical properties of H_2 require modifications to combustor design and combustion characteristics. Issues such as flame speed [5, 6], emission [7], lean blowout limit [8, 9], vortex field [10], and flame structure [11, 12] on the combustion of H_2−enriched fuels have been considered in the past. Among them, Cozzi et al. [11] investigate the effects of H_2 addition on a natural gas non−premixed flame. From the experimental result, it is confirmed that the H_2 blending increases the flame stability limit, decreases the flame length, and increases the CO, and NO_x emission content in the non−premixed flame. Similar work was conducted on H_2−enriched premixed flame and the experimental result reports the reduction of CO gas [13], which is a contrary result to non−premixed flame. It is also reported that the H_2 content induces a shorter and more robust flame [14], similar to the

non-premixed flame [11].

Previous experimental work [15] found that the profiles of combustion instability in a combustor also varied depending on the fuel conditions. Furthermore, the frequency of combustion instability was produced in proportion to the flame speed of the fuel, which is acoustically unpredictable. A similar experimental work by Lee et al. [16] has looked into the relationship between instability and flame structure for a varied composition of syngas. To complement the experiments, several numerical studies have reported on the effect of H_2 content on the global combustion process. The simulations were performed on the swirl-stabilized flames in gas turbine combustors using Reynolds-averaged Navier-Stokes (RANS), large eddy simulation (LES), and direct numerical simulation (DNS) [17-20]. Among them, Mansouri et al. [17] conducted RANS simulations to identify the changes of flammability limits, gas emissions, and flame structure when H_2 is added to propane fuel. Hernandez-Perez et al. [18] conducted LES on premixed H_2-enriched methane (CH_4) flames and investigated the effect of H2 on flame structure and wrinkling characteristics in combustor. Furthermore, DNS of H_2 blending effect in combustor has been reported [20]. However, only a limited number of studies have reported on numerical investigation of the fuel composition effect on combustion instability. While there exist numerical works that considered single hydrocarbon fuels during combustion [21-25], none have considered the effect of H_2 composition, specifically, on the combustion instability. Also, few works have been performed on the interaction of premixedness and H_2 addition effects on flame and stability, while many industrial gas turbines operate in partially premixed condition with various premixedness ratio [26].

Based on these issues, the present study considers the pure H_2 and H_2/CH_4 mixtures for operation and investigates the effect of H_2 composition on the flame structures and combustion instabilities inside the combustor. The flow rate is considered as an additional variable to determine how the flame structure and fuel composition are correlated. Simulations are performed both partially premixed

and fully premixed conditions. Therefore, the impact of H_2 addition and mixing method is simultaneously studied in the combustor, which was rarely reported in past research. By changing operating conditions, the effects on the flame structures and triggering combustion instabilities are discussed.

2.2. Experimental and numerical method
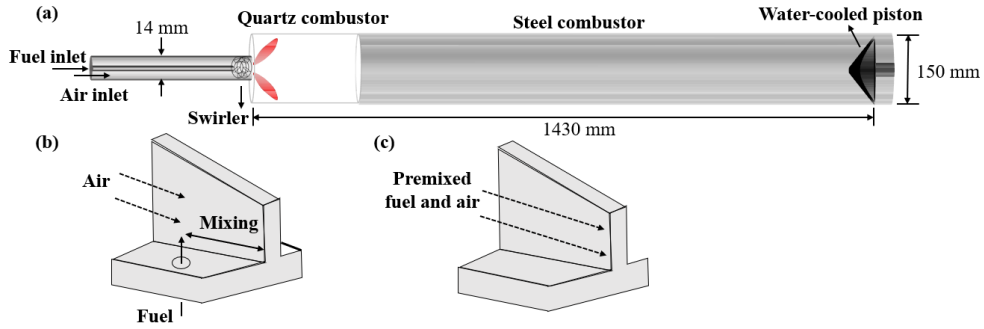
Fig. 2.1. (a) Schematic of the model gas turbine combustor [11] and detailed view of the swirl vane in the (b) partially premixed and (c) premixed condition.

The partially premixed model gas turbine combustor, shown in Fig. 2.1, was used to study the effect of the H_2 composition and premixedness on the unstable combustion. The combustor is operable under H_2-fueled conditions and experimental works [11] were performed for the H_2-enriched and partially premixed condition. As shown in Fig. 2.1a, the cylindrical combustor has a diameter of 0.13m in a radial direction and an axial length of 1.43 m. A transparent quartz combustor is located at 200 mm in the axial direction from the dump plane, where the flame mainly takes place. The other part of the combustor is composed of stainless steel and water cooling is applied at the combustor wall. 90 percent of the combustor outlet area was blocked via a plug nozzle to achieve an acoustic boundary at the combustor. In the experiments, supply of air and fuel at the inlet was controlled by a mass flow controller (MFC) and RS-232 communication modules. The uniformity of the

6

inlet fuel mixture was acquired via an inline mixture. Well-mixed fuel was injected into the combustor through 14 fuel holes within the inner side of the swirl vanes 2.7 mm upstream of the dump plane (Fig. 2.1b) to form a partially premixed flame in the combustor. A total of 11 dynamic pressure sensors and 4 k-type thermocouples are installed through the wall and were used to measure the unsteady pressure and control the inlet air temperature. The particle image velocimetry (PIV) technique was adapted to obtain the flow field during the reacting condition. An ND-YAG laser was used for the PIV measurement, and the scattering signal was measured via a CCD camera, lens, and bandpass filter. Also, the OH-chemiluminescence was measured in the quartz combustor to obtain the flame structures of the swirling turbulent flames. The premixed condition was only considered in numerical approach. In premixed condition, fully premixed fuel and air were injected into the 'Air inlet' in Fig. 2.1a and swirled at the swirl vane shown in Fig. 2.1c. The swirler newly considered in the simulation (Fig. 2.1c) supplies fully-premixed fuel and air prior to the injections. Therefore, the degree of premixedness becomes higher, forming convection flames inside the combustor.

For the numerical study, Large-eddy simulations (LES) were performed using the finite volume method for spatial integration with an open-source CFD tool, *OpenFOAM* [27]. In particular, transient combustion solver, *reactingFoam*, was used in this study. The compressible governing equations of mass, momentum, energy, and species for the simulation of reacting flow are as follows.

$$\frac{\partial}{\partial t}(\bar{\rho}) + \frac{\partial}{\partial x_i}(\bar{\rho}u_i) = 0 \tag{1}$$

$$\frac{\partial}{\partial t}(\bar{\rho}u_i) + \frac{\partial}{\partial x_j}(\bar{\rho}u_i u_j) = -\frac{\partial}{\partial x_i}(\bar{\rho}) + \frac{\partial}{\partial x_j}((\mu + \mu_t)\frac{\partial u_i}{\partial x_j}) \tag{2}$$

$$\frac{\partial}{\partial t}(\bar{\rho}h) + \frac{\partial}{\partial x_i}(\bar{\rho}u_i h) = \frac{\partial}{\partial x_i}((\bar{\rho}\alpha + \frac{\mu_t}{\mathrm{Pr}_t})\frac{\partial h}{\partial x_i}) + \overline{\dot{\omega}_T} \tag{3}$$

$$\frac{\partial}{\partial t}(\overline{\rho}Y_i) + \frac{\partial}{\partial x_j}(\overline{\rho}u_jY_i) = \frac{\partial}{\partial x_j}((\overline{\rho}D_{im} + \frac{\mu_t}{Sc_t})\frac{\partial Y_i}{\partial x_j}) + \overline{\dot{\omega}_i} \qquad (4)$$

Here, $\overline{\rho}$ is the averaged density, u_i is the Favre-averaged velocity, $\overline{p}$ is the averaged pressure, h is the Favre-averaged enthalpy, Y_i is the Favre-averaged mass fraction of species i, $\overline{\dot{w}_T}$ is the averaged heat of reactions and $\overline{\dot{w}_i}$ is the averaged production rate of species. The turbulence properties μ_t, Pr_t, and Sc_t are the turbulence viscosity, the turbulence Prandtl number, and the turbulence Schmidt number, respectively. The fluid properties μ, k, α and D_{im} are the viscosity, the thermal conductivity, the thermal diffusivity, and the mass diffusivity, respectively. The molecular diffusion coefficients of D_{im} for a carrier gas of N_2 are calculated using the Chapman-Enskog theory [28]:

$$D_{im} = \frac{1 - X_i}{\sum \frac{X_j}{D_{ij}}} \qquad (5)$$

$$D_{ij} = D_{i-N_2} = 1.88262 \cdot 10^{-2} \cdot \frac{T^{1.5}\sqrt{\frac{M_i + M_{N_2}}{M_i M_{N_2}}}}{p(\frac{\sigma_i + \sigma_{N_2}}{2})^2 \Omega_D} \qquad (6)$$

where the M_i is the molecular weight, σ_i is the collision diameter, and Ω_D is the function of the characteristic Lennard-Jones energy, which are given in textbook [29]. The module of diffusion coefficient calculation was developed by Novaresio *et al.* [30] and was implemented in the *reactingFoam* solver.

For low-Mach number solutions requiring pressure closure, the PIMPLE algorithm was used. In the LES framework, relatively large-scale motions are directly solved and small-scale motions are modeled using a subgrid-scale stress model. In this study, the

subgrid−scale modeling was performed using the WALE model [31]. The subgrid−scale viscosity is described using the following equations.

$$\nu_{sgs} = (C_k \Delta)^2 \frac{(S_{ij}^{\ d} S_{ij}^{\ d})^{3/2}}{(\overline{S}_{ij} \overline{S}_{ij})^{5/2} + (S_{ij}^{\ d} S_{ij}^{\ d})^{5/4}} \tag{7}$$

$$\overline{S_{ij}} = \frac{1}{2}(\frac{\partial u_i}{\partial x_j} + \frac{\partial u_j}{\partial x_i}) \tag{8}$$

$$S_{ij}^{\ d} = \frac{1}{2}(\frac{\partial \overline{u_k}}{\partial x_i}\frac{\partial \overline{u_j}}{\partial x_k} + \frac{\partial \overline{u_k}}{\partial x_j}\frac{\partial \overline{u_i}}{\partial x_k}) \tag{9}$$

where ν_{sgs} is the subgrid−scale viscosity, C_w is the model constant, Δ is the filter cutoff width, $\overline{S_{ij}}$ is the filtered strain rate tensor, and $S_{ij}^{\ d}$ is the velocity gradient tensor, respectively. In the simulation, the model constant C_w is fixed as 0.325.

In the presented simulation, accurate calculations of the flame length and flame structure, as well as the OH profile, in comparison with the experimental data are key factors in the analysis of the dynamics of the combustor flow. Accordingly, a 23−step reduced chemical kinetic scheme consisting of 15 species [32] was implemented to calculate the reaction rate of H_2−enriched CH_4 flame. The kinetics of this scheme was verified prior to a full combustor simulation for the laminar flame speed. We calculated the 1D laminar flame speed using the current OpenFOAM solver and verified the chemical kinetics as implemented in the combustion solver. Figure 2.2 shows a comparison of the 1D calculation with the experimentally measured laminar flame speed and a reference calculation [33]. The comparison shows that the solver accurately predicts the flame speeds under various pressure conditions. Therefore, the kinetics and solver are suitable for simulating the H_2−enriched CH_4 laminar premixed flame in a combustion chamber.
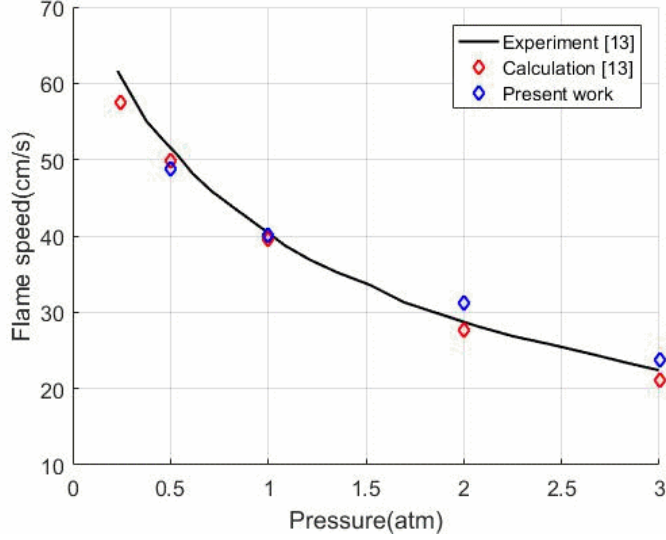
Fig. 2.2. Verification of the chemical kinetics with the previous results [33].

Regarding turbulent combustion, the turbulent flame speed indicates burning intensity of turbulent premixed flame. Expressions of turbulent flame speed were previously reported based on semi-empirical scaling laws [34] and passive scalar in flames [35]. However, the global model of turbulent flame speed covering various experimental and flame conditions is elusive [36]. Therefore, modeling of the turbulent flame is considered while the validation of turbulent flame speed is not handled.

In modeling of the turbulent partially premixed flame in a model gas turbine combustor, the Arrhenius rate law is usually not suitable because the actual reaction rate is nonlinearly dependent on the temperature and species composition. Therefore, it cannot be resolved on LES grids due to their small scales.

$$\overline{\dot{w}_i(\rho,T,Y_j)} \neq \dot{w}_i(\overline{\rho},\overline{T},\overline{Y}_j) \tag{10}$$

To properly handle such a source term, an additional approach, called the turbulence-chemistry interaction model, was adapted. To

simulate a partially premixed flame, where the fuel and the air are not fully premixed prior to entering the combustor, the Partially Stirred Reactor (PaSR) model [37] was used. The production rate of a reaction i is written as follows:

$$\frac{dc_1}{d\tau} = \frac{c_1 - c_0}{\tau} = \frac{c - c_1}{t_m} = f_i(c) \tag{11}$$

$$c^1 = c(\frac{\tau}{\tau + t_m}) + c^0(1 - \frac{\tau}{\tau + t_m}) \tag{12}$$

$$f_i(\mathbf{c}) = (v_i^{''} - v_i^{'})\dot{w}_i \tag{13}$$

Here, c_1 and c_1 are the concentrations at the inlet and outlet of the cell, respectively, $v_i^{'}$ and $v_i^{''}$ are the stoichiometric coefficients, τ is the time step, t_m is the micro mixing time, and $\dot{w}_i$ indicates the progress rate of the reaction i. Using the above relations, a generalized model can be derived:

$$f_i(\mathbf{c}) \simeq f_i(\mathbf{c}^1) + \frac{\partial f_i}{\partial c}\bigg|_{c=c_1}(c - c^1) = f_i(\mathbf{c}^1) - \frac{c - c^1}{t_c} \tag{14}$$

$$\frac{c_1 - c_0}{\tau} = f_i(c^1) \cdot \frac{t_c}{t_c + t_m} \tag{15}$$

where t_c is the chemical reaction time scale. The chemical source term was determined based on the given chemical interaction model. Also, for the simulation, a second−order semi−implicit Crank−Nicholson scheme is used for unsteady terms for time integration and a second−order central difference scheme is used for diffusive fluxes. A one−step monotonic scheme with flux limiter [38] that is second−order accurate in the smooth region and first−order accurate in steep gradient is used for convective fluxes.

In the experiment, the fuel and air are injected through a plug nozzle with a swirl number of 0.832. The mass flow rate of the air was fixed as 1100 slpm (liter/min), and the fuel flow rate was

varied according to the composition of the syngas because the heat input of the syngas was fixed to 40 kW. Based on the given condition, the initial conditions of the simulation are set as the following table:

Table 2.1. Initial conditions of the simulated cases in various syngas compositions.

Case	A	B	C	D
H_2 ratio (mole F.)	50	75	100	50
Eq. ratio	0.552	0.529	0.48	0.552
Fuel flowrate (slpm)	102.0	139.8	222.0	102.0
Air flowrate (slpm)	1100	1100	1100	1100
Heat input (kW)	40	40	40	20

In this work, a total of four inlet conditions are considered for investigating the effect of H_2 composition and premixedness. When the H_2 composition is varied, the heat input of the fuel is fixed at 40 kW, and the flow rate and equivalence ratio are changed accordingly. The air flow rate is fixed at 1100 slpm regardless of the fuel condition. In case D, a reduced fuel flow rate was set with a heat input of 20 kW. In cases A, B, C, both premixed and partially premixed conditions are considered in the simulations and only partially premixed condition is considered in case D.

As for the boundary conditions, the no-slip adiabatic wall is applied to the wall. Dirichlet boundary conditions are used at the fuel and air inlets, and velocity values based on the injection flow rate are explicitly specified. At the outlet section of the combustor, outflow condition based on atmospheric pressure is applied, and Neumann boundary conditions are applied to other parameters.

Before the simulation, a three-dimensional stereolithography (STL) file is produced based on a blueprint, and meshing is subsequently performed. Open-source software fvMesh is used for the pre-processing, and unstructured mesh is applied to take account of the complex geometry.
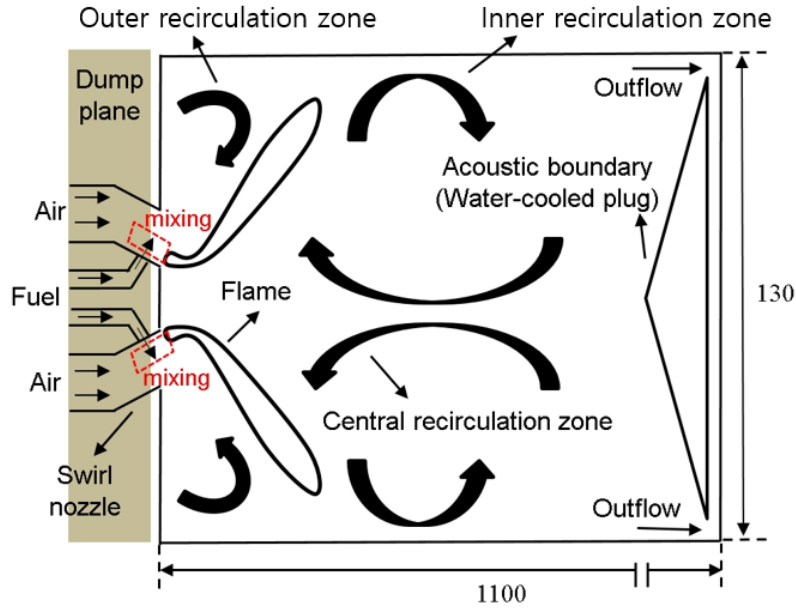
Fig. 2.3. Planar schematic of the partially premixed cylindrical gas turbine combustor.

As shown in the schematic of combustor (Fig. 2.3), the fuel and air are partially premixed in a relatively short mixing zone (2.7 mm) inside the swirl nozzle. The syngas is continually injected through the combustor and generates a V-shaped swirling flame. In the simulations, very fine mesh with y+ < 1 is applied in the near-wall region to resolve small-scale turbulence at the edges of the swirler. In the combustor, a 2-mm unstructured mesh was used in the flame-generating zone to properly resolve the reacting zone. In addition, a 4-mm unstructured coarse mesh was used in regions where the reaction did not occur.

2.3. Results and discussion

2.3.1. Flame structure

Images of the simulated time-averaged flames in the gas turbine were compared to the experimental data in the partially premixed condition. In the experiment, an OH-chemiluminescence measurement was conducted at the quartz tube using a high speed ICCD camera to visualize the flame. The frame rate in the

measurement was 7,000 frame/s, and the recorded image size was 1024 × 1024 pixels. The images were recorded for approximately 1 second and were time-averaged to capture the mean values of the flame images. In the time-averaged image, the OH signal in the flame was accumulated into two dimensions. In the simulation, the OH mass fraction was calculated and time-averaged. The data were continually integrated along the y-axis to match the experimental conditions (Fig. 2.4a). The Abel-inversion technique was used on the averaged images in both the experiment and the simulation to capture the 2D flame boundaries and to analyze the flame structures.
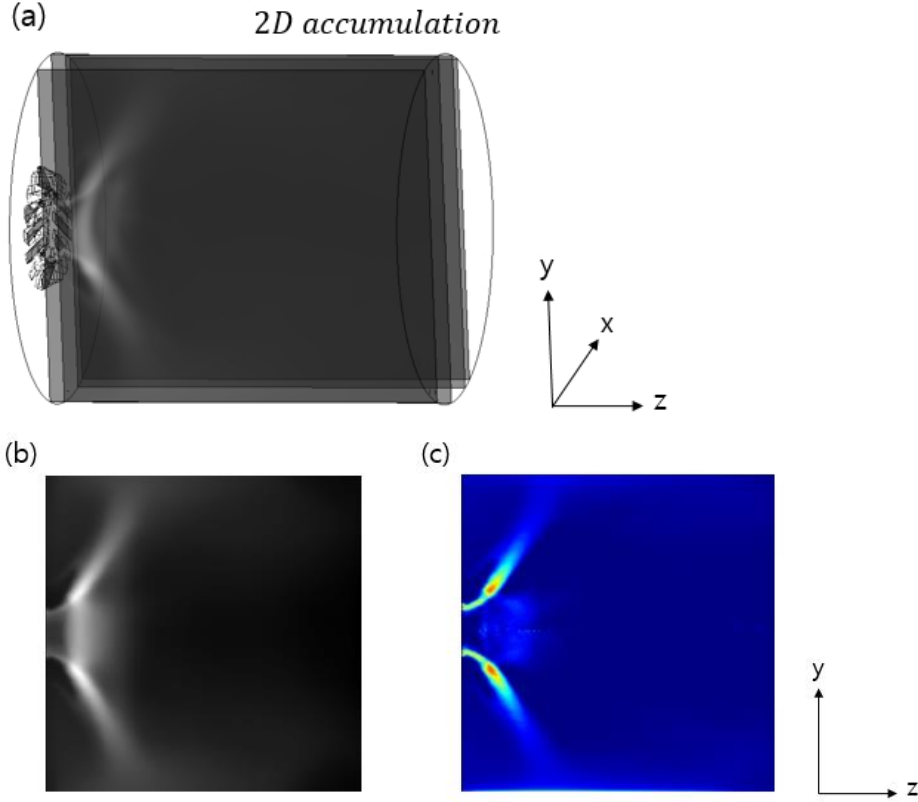
Fig. 2.4. (a) Accumulation of the 3D profiles into a 2D image, (b) the accumulated image, and (c) the Abel-inversion image.

To properly implement the imaging process, the three-point Abel method proposed by Dasch [39] was applied using a MATLAB code. The Abel-inversion code reads in the brightness of the

accumulated grayscale images (Fig. 2.4b) and transforms them into the processed images (Fig. 2.4c).
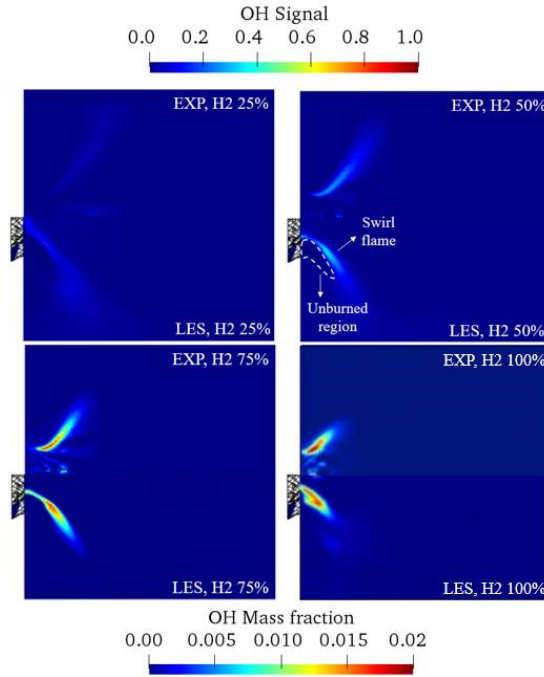
Fig. 2.5. Comparison of the partially premixed flame structure shown in the experiment and LES with the H_2 content of 25%, 50%, 75%, and 100%.

Inside a combustor, a V−shaped partially premixed flame was shown and its structure varied depending on the H_2 composition. Comparison results of the simulated flame structure with experimental data are presented in Fig. 2.5. The time−averaged OH mass fraction profiles were calculated with the different H_2 compositions and their shapes were compared with the OH* chemiluminescence image. In both experiments and LES, the flames were shown in the narrower region with a higher intensity as the H_2 composition increased. The corresponding results were influenced by the high reactivity of H_2, which leads to the fast flame speeds of the fuel mixture. The unburned region with no chemical reaction, which affects the flame shape, showed next to the swirl flame. This area consists of mostly air with low fuel content, and a low

equivalence ratio prevents the chemical reaction. The unburned region was also measured in the previous experiment [40], and its length was reported as the reason for the combustion instability mode shifting. The angle and length of the flames in LES agreed well with the experiment while the ignition in LES starts at the entrance of the combustor. The disagreement in the flame starting point was due to the chemical mechanism in LES, which was focused on predicting the flame speeds of fuel. The flame tip showed the dispersed shape and its trend becomes more pronounced at the low H_2 composition. Rotating flows located in inner and outer recirculation zones affected this phenomenon.

(a) Partially premixed, jet-in-crossflow
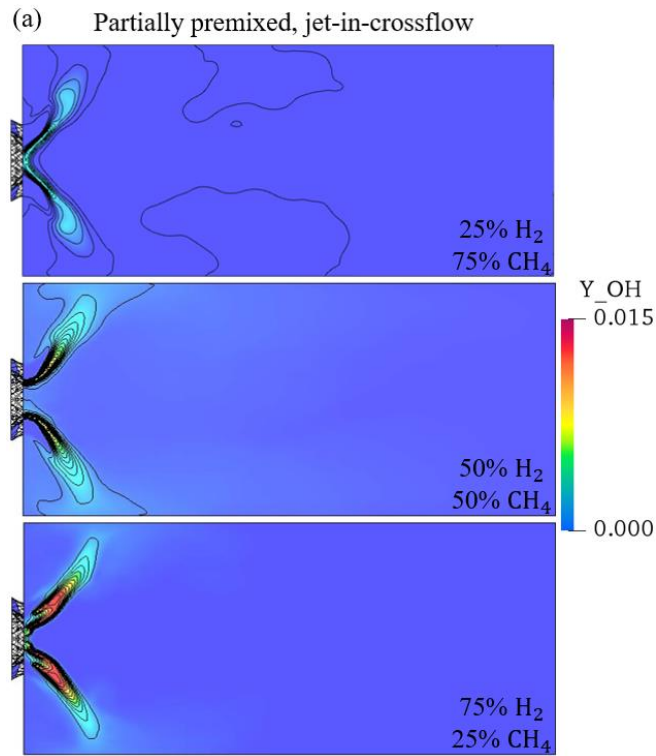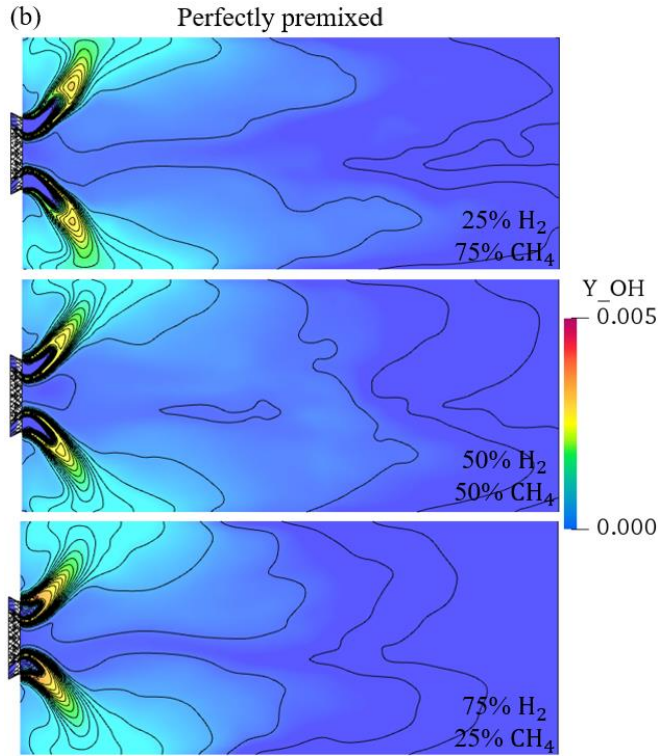
Fig. 2.6. Contours of the LES OH mass fraction results with different H_2 compositions in (a) partially premixed and (b) premixed conditions.

The OH mass fraction contour of the partially premixed and premixed flame in different H_2 compositions is presented in Fig. 2.6. The partially premixed and premixed mixtures were ignited near the swirl injectors, where the ignition position diversified due to the mixing condition and H_2 composition. Fast ignition delay and flame speed of H_2 affect both the partially premixed and premixed flame. High H_2 composition causes pulling of the flame area to the combustor entrance and reduces the flame length. In the partially premixed flame, the supply of the fuel in the swirler was conducted in the form of jet-in-crossflow. The feeding of the partially premixed jet flow into the combustor causes the thin flame near the combustor entrance. The structures of the partially premixed flame were diversified depending on the H_2 composition. In 25% H_2 composition, the flame length exceeds the radial length of the combustor and causes continuous burning through the recirculation

zones near the combustor wall. In 50% H_2 composition, the radial length of the flame becomes close to the combustor radial length, and it causes fewer flame-wall interactions than the 25% H_2 composition. Burning at the recirculation area is also shown in 50% H_2 results. In the 75% H_2 composition, the flame barely interacts with the wall compared to the other results. In this case, burning takes place in a short reaction regime, and the reaction rate represented with OH fraction was higher than the other results due to the fast flame speed of H_2. Flame thickness was relatively little changed with the increase of H_2 composition, while the flame thickness near the wall decreased with the low density of H_2 and higher density ratio of unburned and burnt mixtures.

Compared to the results of partially premixed flame, flame structures were widely distributed for the premixed flames. The increased length of flames was caused by the fuel injection direction, where the partially premixed mode radically injects the fuel into the swirler and the premixed mode axially injects the fuel and air into combustor (Fig. 2.1). Premixed flame lengths all exceeded the radial length of combustor, and therefore, similar flame structures appeared with variations in H_2 composition. As a result, burning continuously takes place through the recirculation zones in all premixed cases. The premixed flame structures are expected to change due to H_2 composition in a larger-scale combustor, while that issue is left for future studies.

2.3.2. Mean flow fields
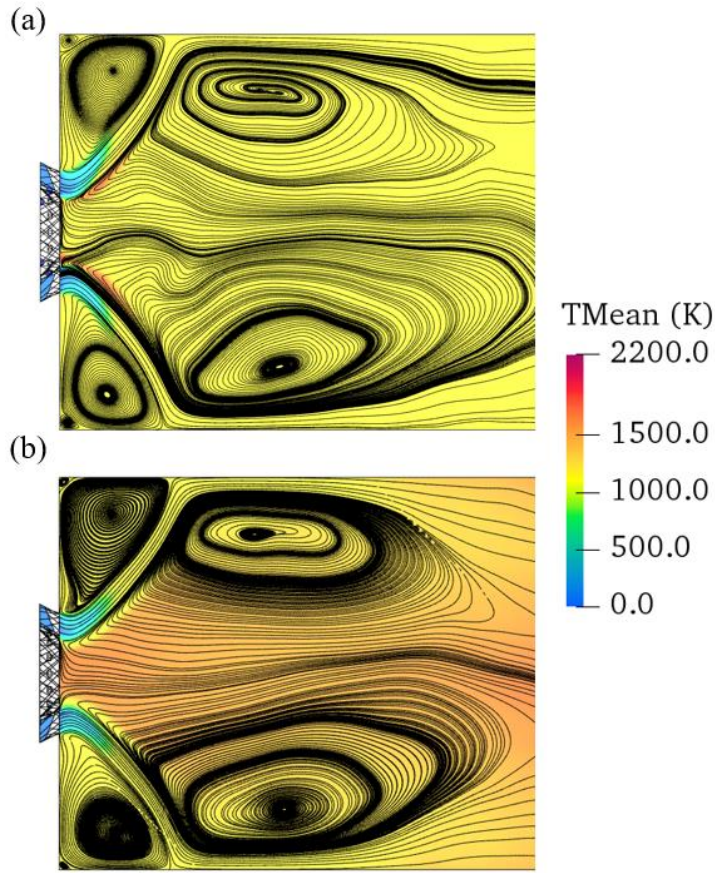
Fig. 2.7. Temperature contours superimposed with streamline in the combustor with (a) partially premixed and (b) premixed conditions.

The examples of streamlines with temperature contours of partially premixed and premixed flames are presented in Fig. 2.7. In both flames, the unburned regions showed a temperature around 500 K, which coincides with the inlet air temperature. Also, the outer recirculation zone near the dump plane and the inner recirculation zone through the combustor wall were shown. Injecting flow forms the shear layer and divides the two recirculation zones. The streamline structures of the two flames were similar, and it shows that the injecting air works the main role in forming the flow structure in the combustor. In the partially premixed flame (Fig. 2.7a), burning takes place in the thin reaction regime and with a temperature of 2200 K. The hot burnt gas mixed with relatively cold flow from the unburned region and forms a

temperature of around 1200 K. A temperature drops as the reaction rate goes down, and burnt gas rotates through the recirculation zones. In the premixed flame (Fig. 2.7b), burning continuously progressed near the wall due to the long flame length. Therefore, the hot flow region with a temperature of 1500 K is formed in the center of an inner recirculation zone.
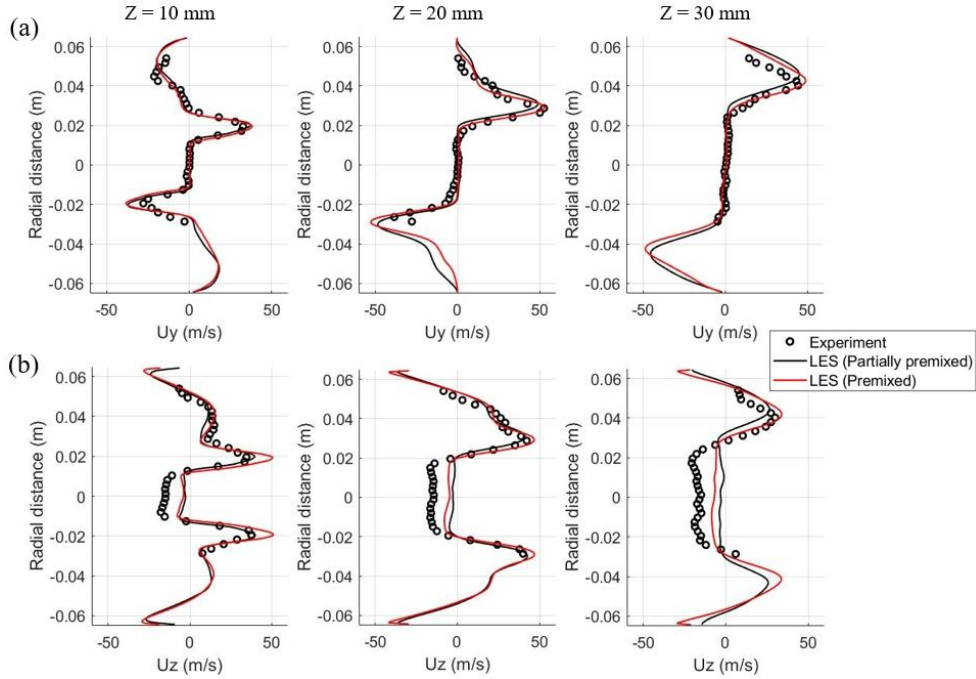
Fig. 2.8. The time averaged (a) radial and (b) axial velocity profiles in partially premixed (dark line) and premixed (red line) conditions in comparison with experimental results (dark dot).

In Fig. 2.8, the mean velocity profiles inside partially premixed and premixed combustors are compared to the experimental results. The velocity was measured using PIV in the partially premixed condition. A comparison was conducted for radial (Fig. 2.8a) and axial velocity (Fig. 2.8b) components with different axial regions. Good agreements were shown between LES and experimental results. A little difference appeared in the reverse flow region at the center of the combustor (Fig. 2.8b). After reaching the combustor outlet, part of the burnt gas bounces off to the

combustor inlet. The reverse flow from the combustor outlet was not sufficiently formed due to the limitation of computational time, resulting in a difference with the experiment. In LES, the peak velocity generated from flow injection was similar to measurement, and results from premixed flame were faster than partially premixed flame. The variance resulted from the mixing method. The partially premixed method injects the fuel in jet-in-crossflow form, interrupting airflow injection. While in premixed method, the fuel and air are fully premixed prior to the injection. The flow speed near the rigid wall was similar in the two mixing cases, indicating that the recirculation zones were formed similarly in both LES.

2.3.3. Combustion instability

In H_2/CH_4 50:50 and partially premixed condition, strong combustion instability is developed. The simulation is compared with the experimental data measured at dynamic pressure sensors in the combustor at the same location. For frequency analysis, fast Fourier transform (FFT) is performed to construct the pressure spectra, and the result is shown in Fig. 2.9.
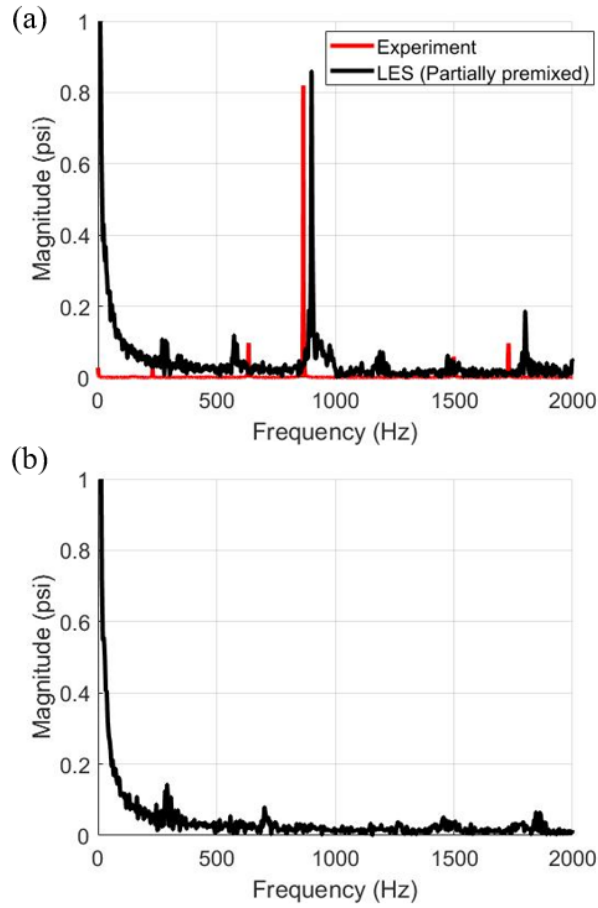
Fig. 2.9. Pressure spectra of the pressures inside the (a) partially premixed and (b) premixed combustor.

The frequency spectra of the pressures inside the partially premixed and the premixed combustor are drawn in Fig. 2.9 based on the transient pressure at the combustor measured at 1.02 m from the dump plane. The peak frequency is shown near 900 Hz and is in good agreement with the peak frequency of the experiment. Oscillation in the other frequency was weakly shown, where the local maximum frequency near 500 Hz indicates 2nd harmonic mode and the local maximum frequency near 300 Hz indicates the natural frequency inside the combustor. In the perfectly premixed flame, the relatively weak oscillation was shown at the natural frequency of 300 Hz and 3rd harmonic frequency of 700 Hz. The weak oscillation at 3rd harmonics indicates that the thermoacoustic

feedback loop did not appear in the premixed case.
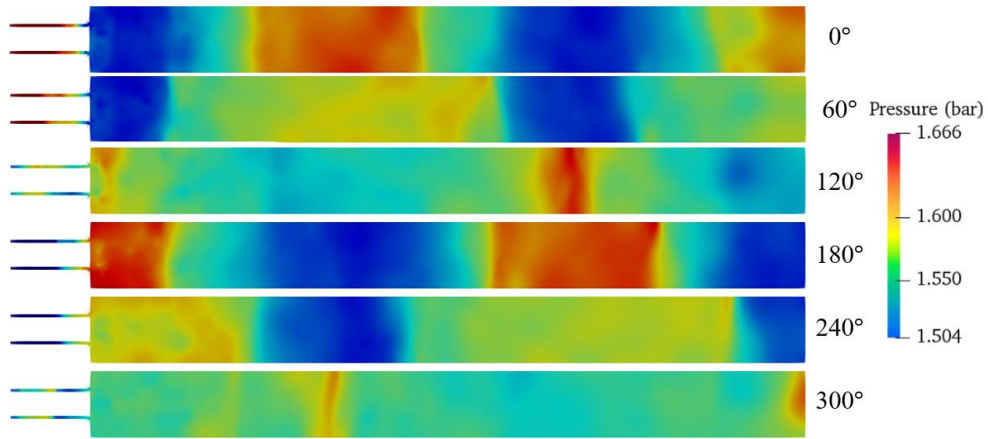
Fig. 2.10. Phase-locked pressure fields inside the gas turbine combustor with 6 phases in oscillation period.

The phase-locked instantaneous pressure fields inside a partially premixed combustor are shown in Fig. 2.10. The pressure distribution represents the 3rd harmonic longitudinal mode through the combustor and it corresponds to the reported result in the previous measurement [16]. The local changes of pressure are shown near the combustor entrance due to the formation of flame. The pressure oscillation is also shown in the supply line on the left side of the combustor, and it indicates that the supply line is included in the feedback loop in the combustor. Since the magnitude of self-sustained pressure oscillation is high, the information on flame and vortex structure is not well described in Fig. 2.10.
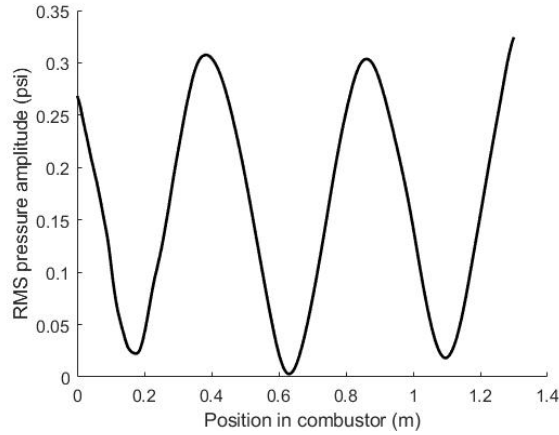
Fig. 2.11. RMS pressure amplitude distribution in the unstable
H₂/CH₄ result.

The graph in Fig. 2.11 shows the root mean square (RMS) pressure amplitude distribution with respect to position of combustor in unstable condition (Fig. 2.9a). The instability mode differs from the natural frequency of the combustor, which suggests that simulation can accurately interpret the generation and mode transition of the instability due to the fuel composition.
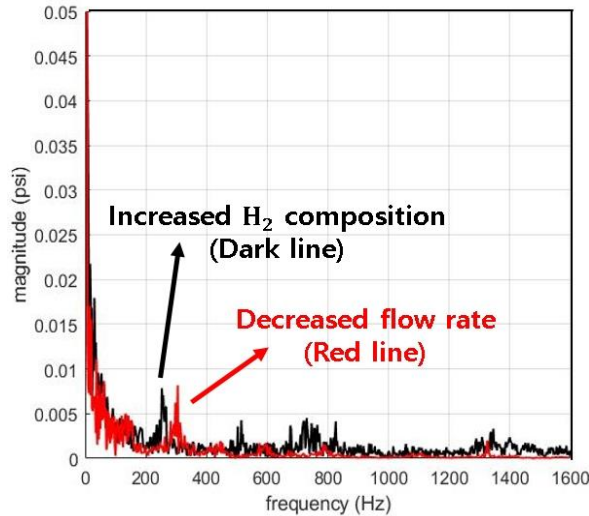
Fig. 2.12. FFT results for numerical pressure profile for increased
H₂ composition (100% H₂) and reduced fuel flow rate (20kW).

In contrast to H₂/CH₄ case, the self-excited oscillations do not

occur when H_2 content is increased to 100% at the same heat input. The pressure spectra through FFT is also plotted for the increased H_2 composition condition and reduced fuel flow rate condition, and the results are shown in Fig. 2.12. From the experimental results [16], negligible pressure perturbation occurs at 100% H_2 fuel condition, and the numerical profile presents the similar result. Compared to previous H_2/CH_4 fuel conditions, the results in pure H_2 profile shows a stable performance. From this, it is confirmed that even if the heat input is constant, the characteristics of combustion instability are different depending on the fuel composition.

Furthermore, the result for the H_2/CH_4 flow with the half fuel flow rate (Fig. 2.12) is in contrast to Fig 2.9. The result shows that when the fuel flow rate is reduced, the perturbation mainly occurs at low amplitudes corresponding to the first longitudinal mode. This suggests that fuel flow rate, as well as fuel composition, are involved in the mode transition of the combustor.

In the unstable case, flow analysis through visualization is performed to determine the factors affecting instability characteristics. According to the results, oscillating flame occurs due to flow perturbation in the injector. Four phases of the flame during a single oscillation period (Fig. 2.13) show the contours of perturbating flames.
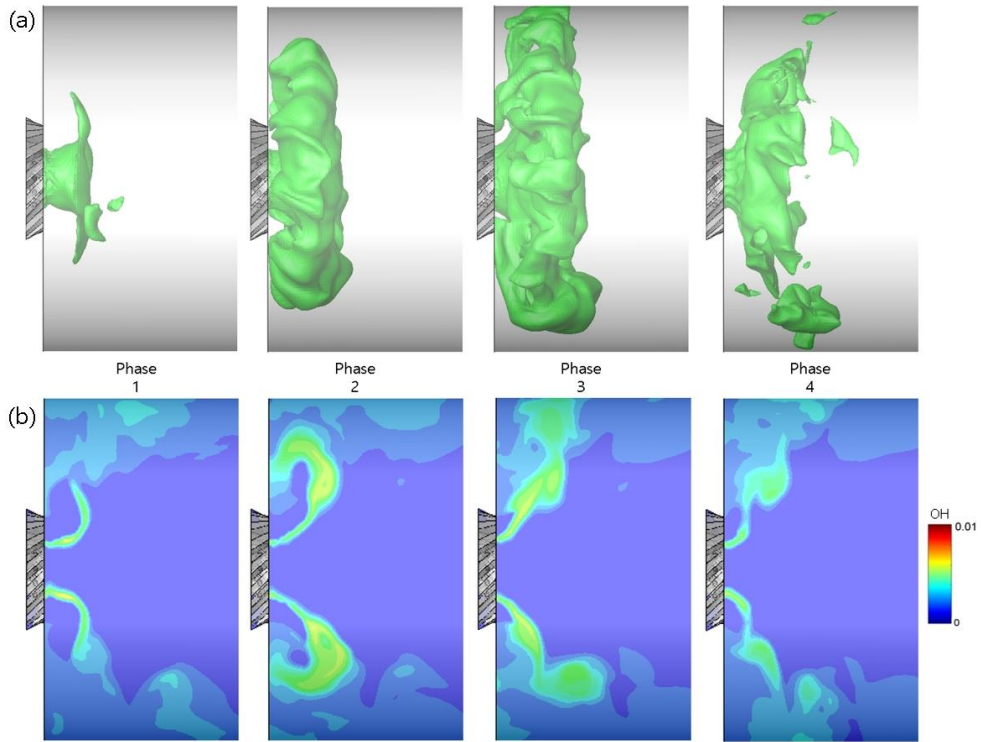
Fig. 2.13. (a) Isosurface of OH mass fraction and (b) yz-plane OH mass fraction profiles of oscillating flame in four different phases.

The isosurface for the OH mass fraction of 0.005 is presented for four phases in Fig. 2.13a. In phase 1, the inlet backflow is stopped as the pressure inside the nozzle gradually decreases and fuel is choked inside the nozzle resulting in a small flame structure. At this time, the flame in the vortex, which occurred in the previous cycle, is almost disappeared and the remaining reactants are moved along the recirculation zone around the rigid wall. In phase 2, as the pressure in the nozzle drops further, fuel begins to be injected strongly into the combustion chamber. Therefore, the flames begin to develop and supply heat energy to the vortices on the wall, increasing the heat release rate in combustion chamber. In phase 3, fuel is continuously fed into the combustor and the most maximized flame structure is generated. In phase 4, the pressure inside the nozzle increases significantly, and the fuel at injector starts to form inlet backflow, causing the flames to begin the decay. However,

flames still remain in the recirculation zone due to the injected fuel up to the previous phase, and heat generation is maximized by continuous burning at this region. The heat release rate fluctuation from flame perturbation show the relationship between the flame and pressure profile in each phase (Fig. 2.14).
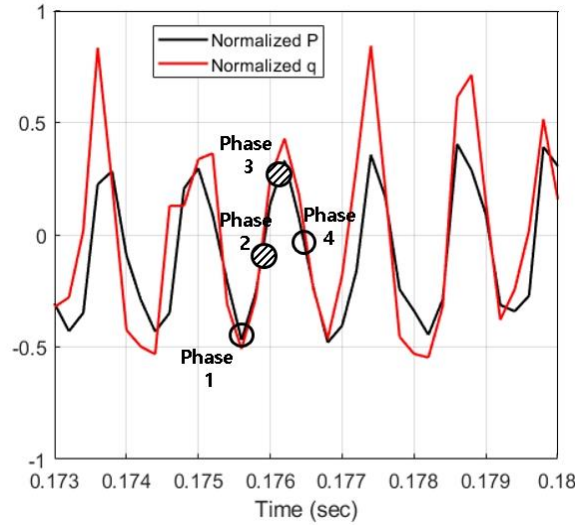
Fig. 2.14. Temporal variation of normalized p′ and q′ profiles at the middle of the combustor in unstable case where the phase marked with hatched circle indicates the phases where the vortex burning takes place.

The heat release rate is measured by calculating the volume integral to the computational domain, and the pressure is measured 30 mm away from the dump plane. It shows that the phase angles of p and q are within 45 degrees at all the time and therefore, Rayleigh criterion is satisfied.
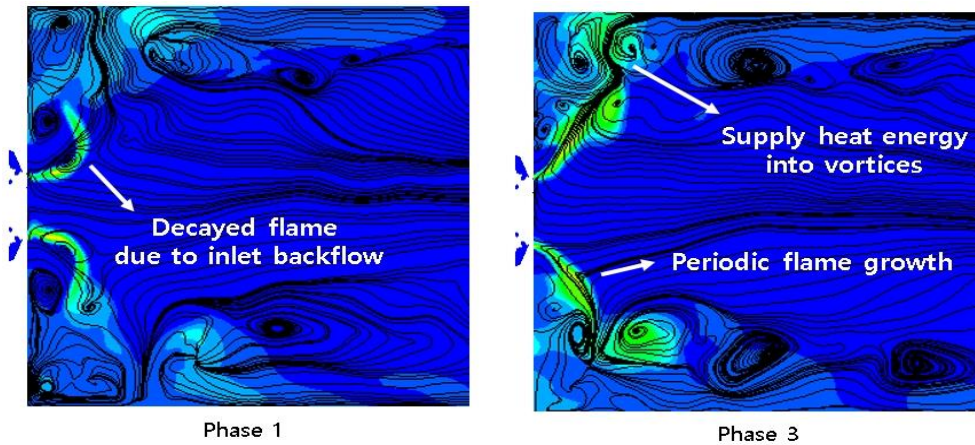
Fig. 2.15. H_2/CH_4 flame in phase 1 and 3 shown with streamline.

Figure 2.15 shows the details of flame−vortices interaction in two different phases and indicates the correlation between heat release rate in Fig. 2.14 and vortex burning. According to the results, small outer recirculation zone is observed between nozzle and ejecting flow. Along the combustor rigid wall, relatively large inner recirculation zones appear. This inner recirculation zone provides burnt gas to the injector and contributes to continuous ignition of unburnt gas. As shown in phases 1 and 3 in Fig. 2.15, the oscillating flame structure under H_2/CH_4 condition serves as a shear layer that separates these recirculation zones. This recirculation zone vibrates intensively, which results in the oscillation of inner recirculation zone along the axial direction of the combustor. Perturbation of the injected flow rate causes periodic vortices burning at the wall. As shown in the hatched circle in Fig. 2.14, vigorous burning at those vortices supplies large heat energy into the combustor, which induces the satisfaction of Rayleigh's criterion.
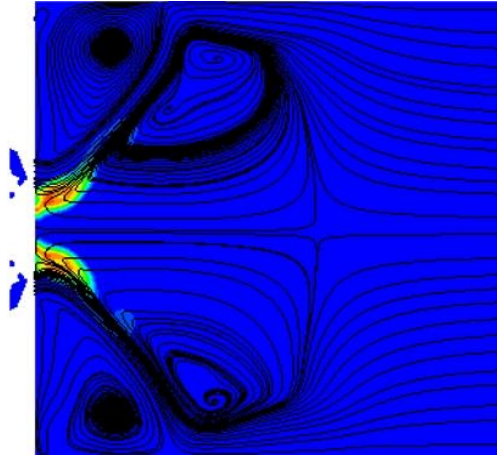
Fig. 2.16. H_2 flame shown with streamline.

From the instantaneous streamline fields shown in Fig. 2.16, the characteristics of the H_2 flame differ from those in the H_2/CH_4 condition. As previously mentioned, H_2 flames ignite very close to the injector and generate narrow flame structure. This narrow flame structure cannot induce intensive vortices burning at the wall and therefore the thermoacoustic feedback mechanism is not strong enough to develop strong instability. Since there is little pulsation of injecting flow in the H_2 case, more stable flow field is generated in combustor. The inner/outer recirculation zone of H_2 flame is formulated in a limited range due to the stabilized H_2 flame. A similar effect is seen when the H_2/CH_4 fuel flow rate was reduced to half (Fig. 2.17).
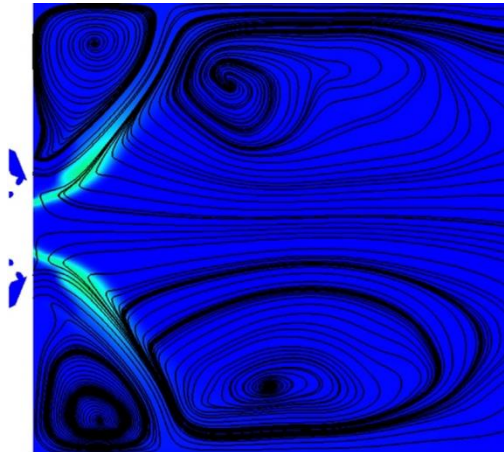
Fig. 2.17. H_2/CH_4 flame with reduced flow rate shown with streamline.

The area of flame generation is similar to that of the flame in H_2 condition. In the streamline field of Fig. 2.17, the reduced H_2/CH_4 flame length cannot induce vortices burning in the combustor, leading to a stabilized flow field.
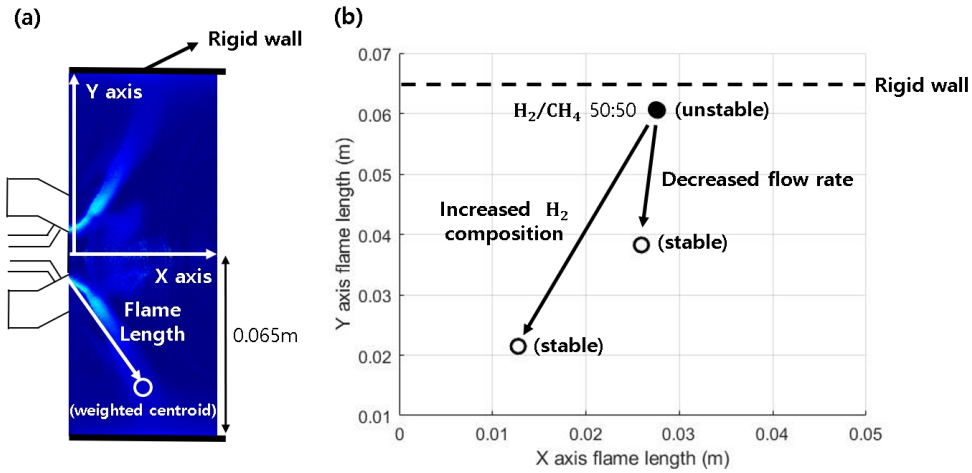
Fig. 2.18. (a) Flame length measurement and (b) flame structure profile and stableness of three test cases.

The flame structure profile for each test case is presented in Fig. 2.18. The flame length is calculated by measuring the intensity-weighted centroid for the OH image (Fig. 2.18a) in the same way as done in [16]. The slow reaction rate of CH_4 led to the formation of a long H_2/CH_4 flame near the position of the rigid wall and caused the interaction with the vortex near the wall. On the other hand, in the results of decreased fuel flow rate and increased fuel H_2 ratio, the y-axis lengths of the flame are reduced, and thus the probability of interaction with the wall vortex is significantly reduced. The simulated profiles show a considerable agreement with the experimental results. For example, Yoon et al. [40] conducted an experiment with various heat input and fuel composition conditions for partially premixed flame and found that the short flame length and stable mode are generated when H_2

3 0

content was sufficiently high. In addition, the stable area increased when the heat input value of the fuel decreased, which is consistent with the simulation. Ghoniem et al. [41] conducted an experiment using a H_2/C_3H_8 mixture for a backward step premixed combustor and found that the effect on dynamic mode transition is similar when the H_2 content is increased and the equivalence ratio is decreased.

In the premixed case, shown in Figs 2.6 and 2.7, the flame length exceeded the radial length of the combustor. Therefore, periodic vortex burning shown in Fig. 2.15 did not appear, and heat release oscillation formed weakly resulting in attenuation of combustion instability. To further investigate the cause of instability, equivalence ratio fluctuation in the swirler is investigated.
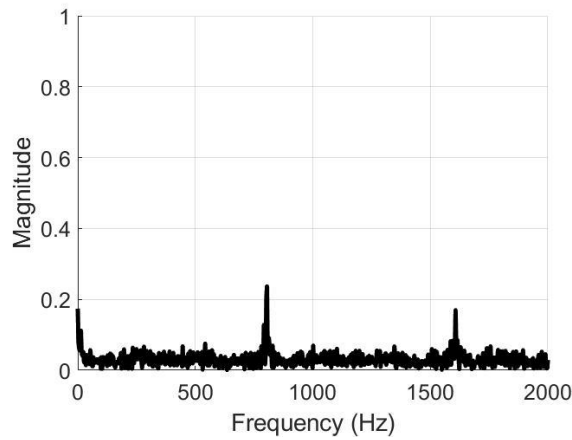
Fig. 2.19. FFT results for the oscillation of equivalence ratio inside a swirler.
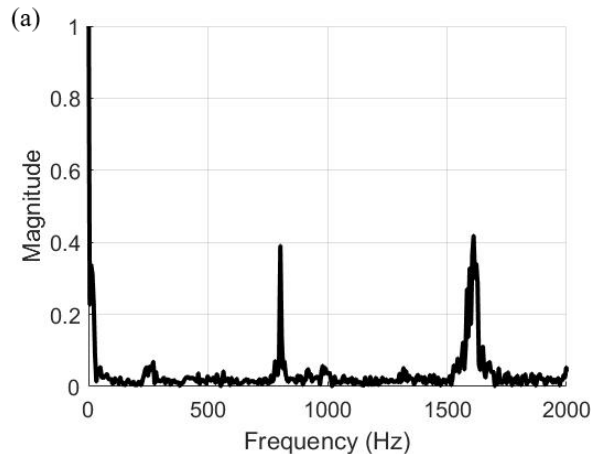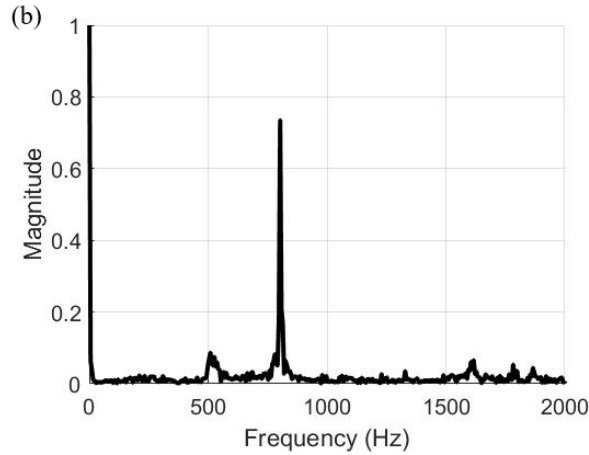
Fig. 2.20. FFT results for the flow rate (a) before and (b) after entering through a swirler.

Figure 2.19 shows the frequency spectra of the equivalence ratio inside a swirler. The peak frequency near 800 Hz was shown, which was the same peak frequency with combustion instability. It implies that the pressure wave at 3rd harmonics induced the oscillation of flow in the supply line, and it caused instability during the mixing process. Since the equivalence ratio was fixed at all regimes, the oscillation during fuel−air mixing did not appear in the perfectly premixed case. Therefore, the oscillation of the equivalence ratio before ignition indicates that imperfect mixing with fuel and air affected the combustion instability in the partially premixed combustor. Local maxima at 300 Hz and 500 Hz were blurrily shown, while the local maximum at 1600 Hz is more clearly shown with a similar magnitude with peak frequency. Those characteristics coincide with experimental work by Kypraiou *et al.*, [42] where the non−premixed flame with radial fuel injection shows the highest flame response due to the equivalence ratio fluctuations.

The spectra of the flow rate in Fig. 2.20 present the flow oscillation before and after entering through the swirler. As shown in Fig. 2.1, the flow is supplied through the swirler with injectors. The flow rate tracked within the injectors (Fig. 2.20b) oscillated

with two main frequencies of 800 Hz and 1600 Hz. The oscillation at 800 Hz was influenced by the combustion instability, while the oscillation at 1600 Hz was caused by the curved geometry of the injectors. The high-frequency oscillation at 1600 Hz was dissipated after entering the swirler (Fig. 2.20a), but still affected the combustion instability in the combustor (Fig. 2.9).

In the present simulation, the H_2-enriched model combustor in partially premixed and premixed conditions was considered. Judging from the above results, the tendency would change under 100% scale combustor condition. As the axial length of the injector and combustor increases, a lower instability frequency will be formed accordingly, and similar conclusions had been shown in previous studies [43]. In addition, when the radial length of the combustor increases, the position of the rigid wall shown in Fig. 3.1.13 changes, and combustion instability is expected to occur at higher flow rates and lower H_2 fuel composition. The radial length of the current combustor was changed in the previous research [44] and the pressure response in the combustor was changed due to the absence of flame-vortex interaction.

2.4. Conclusions

The effects of H_2 composition and premixedness are simultaneously studied in the model gas turbine combustor using LES. From the simulations, combustion characteristics and causes of combustion instability are identified. The simulations are performed for four different H_2 compositions and two mixing conditions. The results show that both flame structure and combustion instability are sensitive to changes in the H_2 composition and the fuel flow rate. It is found that a short flame is generated at a high H_2 composition due to the high diffusivity and faster burning velocity of the H_2 fuel. A similar flame structure is found when the fuel flow rate is reduced by half. The effect of flame structure on the thermoacoustic feedback mechanism is

subsequently discussed. When the flame length is sufficiently long, it induces the periodic vortex burning in the recirculation zone and contributes to the development of instability. In this unstable case, combustion instability corresponds with 3rd harmonic longitudinal mode of the combustor is presented. When the flame length becomes short, on the other hand, very weak instability is found inside the combustor. The effect of flame on the recirculation zone is minimized under the conditions of increased H_2 composition or low flow rate, and therefore stable results are observed. Meanwhile, in the premixed flame, the flame structures are less sensitive to H_2 content since the premixing with air reduces the hydrogen enrichment effects of hydrogen. In the partially premixed case, FFT spectra inside a swirler show the oscillation of the equivalence ratio is measured as the same as the frequency of combustion instability. This oscillation does not exist in premixed conditions. Therefore, it shows that the fuel and air mixing process leads to heat release fluctuation in partially premixed conditions. Overall, this study demonstrates the two factors of hydrogen and premixedness contribute to changing flame structure and cause combustion instability in the combustor. Two phenomena of flame-vortex interaction and equivalence ratio fluctuation induce heat release fluctuation, contributing to self-excited combustion instability.

Chapter 3. Hydrogen-enriched partially premixed combustor: flame transfer function

3.1. Background and motivation

Combustion instabilities (CI) caused by the coupling of acoustic waves and unsteady heat release of the flame have been a major issue of the combustion community in the past decade. Practical combustion systems like gas turbines, rocket engines, and scramjet combustors share the common risk due to CI [1]. The feedback mechanism of CI in combustion systems is non-linear and involves the physics of acoustics, chemical reactions, turbulent flows, which makes it even harder to predict CI numerically. Large amplitude pressure oscillations of the CI limit cycle cause operational uncertainties of engines and possibly damage the combustion chamber. Therefore, prediction and suppression of CI are essential in the design stage of the combustion system. The difficulty in predicting CI not only comes from its non-linearity but also from numerous influencing factors. Existing studies of CI on gas turbine combustors point out that the physics related to the precessing vortex core [2], flame-vortex interaction [3], and fuel conditions [4] were some of the driving factors of CI.

To clarify the stability of the combustion system and to complement the experimental studies, large eddy simulation (LES) is widely used. LES provides the details of flow fields in engines, which are sometimes hard to measure in experiments, and also shows whether the combustion remains stable or not [5]. LES of CI is divided into two approaches: first is to fully reproduce the CI feedback mechanism including the acoustic waves, and second is to use the thermoacoustic models using the flame transfer function (FTF). FTF is defined as the ratio of heat release rate fluctuation to the inlet velocity fluctuation induced by the acoustic wave [6], and LES has shown to be quite promising for obtaining the FTF [7-9].

The FTF result is used as an input on the thermoacoustic network solver, which provides information of CI limit cycle. Related studies by Morgan et al. [10] performed LES for FTF in a partially premixed gas turbine combustor and combined the LES results with the thermoacoustic network solver. The predicted CI information was similar to the experimental result, providing the reliability on LES and network model. Similarly, Joo et al. [11] used their experimental FTF results as the input of a thermoacoustic network solver. Predicted CI profiles on the network model were well—matched with experimental CI results in various fuel conditions. In their works, strong flame responses were shown at some forcing frequencies of FTF, which are correlated with the CI profile. From the experiments, fuel supply line acoustics was suggested as the cause of the resulting FTF values. However, the flame response with a maximum gain was shown under the natural frequency of the supply line, and the cause of this has not been clarified.

Based on the state of limited knowns associated with the CI as reported previously, we performed LES of FTF in a partially premixed gas turbine combustor and looked for the cause of the flame response. In particular, the correlation between the flow dynamics of fuel supply system and those of combustor is sought to explain the cause of CI, which was not the focus of the earlier LES works. In section 3.2, the target configuration describing its geometry, numerical setup, and models are described. In section 3.1, flow responses in the fuel supply system on the acoustically forced condition are presented. Section 3.2 shows the LES result without the external acoustic forcing. Instabilities inside the fuel supply system are investigated to identify the cause of the flow response. Section 3.3 shows the flame response inside the combustor with acoustic forcing. In section 3.4, the overall results are summarized with a discussion. Based on the previous findings, we clarify the role of the fuel supply system on the FTF and CI characteristics, which has not been reported in the past.

3.2. Numerical approach

The experimental setup of a partially premixed model gas turbine combustor is shown in Fig. 3.1 [12]. The setup was designed as a 1/3 scaled-down model of the industrial GE7EA gas turbine combustor. In [12], measurements were made to obtain FTF according to fuel conditions. The setup includes the combustor and the fuel supply system consisting of a supply line and a swirler. The fuel supply line on the left side feeds the fuel consisting of methane and hydrogen into a swirler. The natural resonance frequency of the fuel supply line is calculated as 292 Hz [13] based on the flow sound speed and the fuel supply system geometry. The mechanical pulsator (siren) is located at the inlet of the supply line to impose acoustic forcing of the flow. In the previous experiment [12], the FTF measurements were performed with the forcing magnitude of under $\overline{u}/u'=0.1$, with a forcing frequency of every 25 Hz in the range of 25 to 1000 Hz. The local maxima were found under the frequency of 600 Hz in the various inlet conditions. A forcing frequency in the range of 25 to 600 Hz was applied in the current LES to find the causes of local maxima of the FTF shown. The mean mass flow rate of the fuel consisting of hydrogen-enriched methane was 0.0236 kg/s, which corresponds to Reynolds number of 5630. Air flow rate was set as 0.18 kg/s with a mean equivalence ratio of 0.55. For flame stabilization, a swirler consisting of 14 injectors and swirl vanes are located at the right end of the supply line (Fig. 3.1b). The fuel is injected into the swirl vanes with a swirl number of 0.832 and mixed with air in jet-in-crossflow form (Fig. 3.1b). Partially premixed fuel and air are spark-ignited at the combustor, forming a swirl flame. A cylindrical combustor with a length of 300 mm was considered for FTF measurement. At the outlet of a combustor, non-reflective boundary condition [14] was used to obtain the acoustic feedback-free flow in the combustor and to ensure the non-negative velocities near the outlet. Therefore, the longitudinal acoustic waves within the combustor were neglected. Since the transverse

and circumferential thermoacoustic instabilities did not appear in the experiment [12], no additional modeling was performed at the boundary of the combustor wall. In the results of the current setup, acoustic waves only appear in the fuel supply system. The computational domain of the current work is set the same as the experimental setup, and boundary conditions are shown in Table 3.1.

Table 3.1. Boundary conditions for LES.

Description (units)	Value
Mean inlet velocity (m/s)	11.02
Inlet forcing magnitude (m/s)	1.102
Inlet forcing frequency (Hz)	25 - 600
Inlet fuel temperature (K)	320
Inlet air temperature (K)	473
Fuel composition (H_2/CH_4 mole F.)	50:50
Wall condition	Non-slip
Combustor outlet	Non-reflective
Wall temperature (K)	300 (isothermal)

An unstructured grid was used on the computational domain, and a structured grid was locally used at the wall boundary layer. The grid used in this work contains 5.86 million cells, where 3.84 million cells were located at the fuel supply system and 2.02 million cells were located at the combustor. Figure 3.2 illustrates the grid distribution considered in the simulations, showing the domains of Fig. 3.1a. As shown, the refined meshes are shown in the near−wall region (y^+ within 1) and the flame generation area in the combustor.

(a)
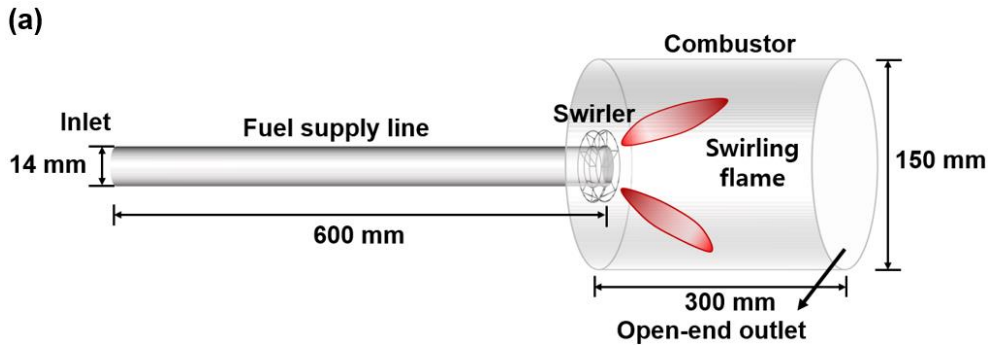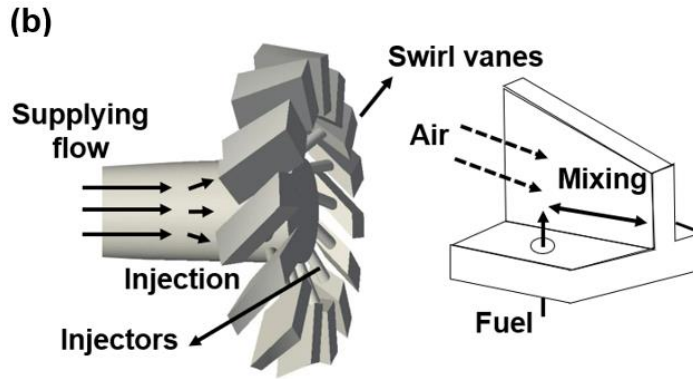
Fig. 3.1. (a) Schematic of the model gas turbine combustor and (b) a detailed view of a swirler.
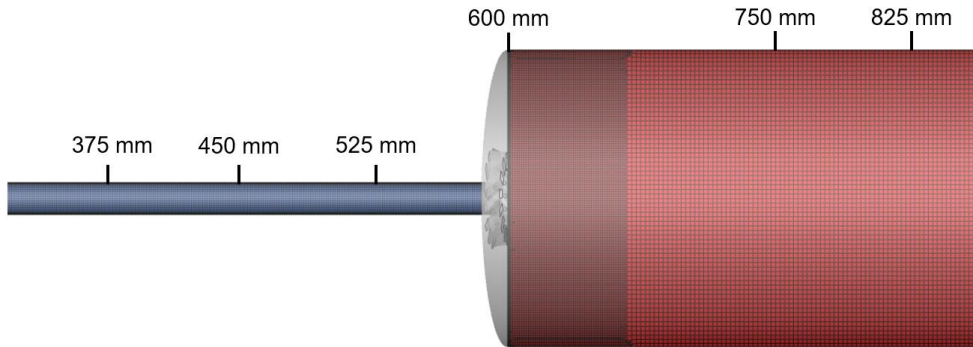
Fig. 3.2. Grid refinement shown with the blue region indicating the fuel supply system and the red region indicating the combustor. Numbers in the figure indicate the distance from the inlet shown in Fig. 3.1a.

The Favre-averaged governing equations consisting of mass, momentum, energy, and species transport were sequentially solved for the reactive flows. The chemical mechanism consisting of 23-step and 15-species [15] was implemented to solve the reactions of hydrogen-enriched methane fuel. Perfect gas was assumed for all gas mixtures and tabulated formation of specific heats and formation of enthalpies were used for each chemical species. Sutherland's law was applied for the calculation of the viscosity, and Fourier heat conduction model, and Fickian diffusion model were used. The wall adapting local eddy viscosity (WALE) LES subgrid-scale model [16] is used for the closure of governing equations,

which does not require additional wall functions in a turbulent transition regime. Turbulent-chemistry interactions in the combustor were handled using the Partially Stirred Reactor (PaSR) model [17] in the filtered reaction rate term.

The LES in this work are performed using an opensource C++ library OpenFOAM [18]. PIMPLE algorithm was used for the pressure-velocity coupling in governing equations. For the time marching, a second-order implicit Crank-Nicholson scheme is used for the unsteady terms. For spatial discretization, a second-order central difference scheme is used for the diffusion term and a second-order difference scheme with the flux limiter is used for the convection term.

LES of the combustion system are performed on a total of 6 cases: 5 with acoustic forcing and 1 with no external forcing. Forcing frequencies of 50, 100, 200, 300, 400 Hz were set to investigate the flow and flame responses in the combustion system (Table 3.1).

3.3. Results and discussions

3.3.1. Grid independence test

The grid independence was checked by calculating the FTF inside the combustor and the index of quality. Different meshes consisting of fine (11.51 million cells), medium (5.86 million cells, current work), and coarse (1.52 million cells) meshes were used for the FTF simulations. The results are presented in Fig. 3.3.
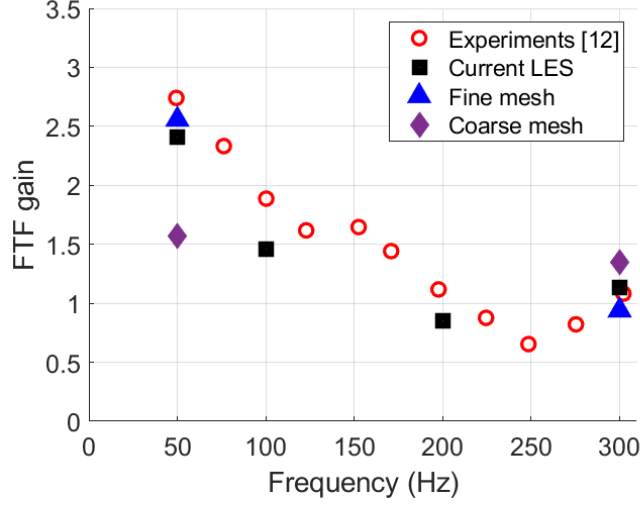
Fig. 3.3. FTF gain by LES and experiment [12] compared with fine and coarse meshes.

Figure 3.3 shows that the calculated FTF gain was similar in fine mesh and current LES, indicating the relevance of mesh distribution in this work. From the coarse mesh case, FTF gain was underpredicted at 50 Hz and overpredicted at 300 Hz. This indicates that the effect of oscillating vortices, which is later described in section 3.2, is underestimated in the simulation. Subsequently, the index of quality (LES_IQ), proposed by Celik et al. [19], was calculated based on the resolved turbulent kinetic energy and subgrid−scale turbulent kinetic energy. The formula of LES_IQ is shown in eq. (1):

$$LES\_IQ = E_{res} / (E_{sgs} + E_{res}) \tag{1}$$

where E_{res} and E_{sgs} are the resolved and subgrid−scale turbulent kinetic energy with its value exceeding 0.8 in most cells, it is considered a good LES result.
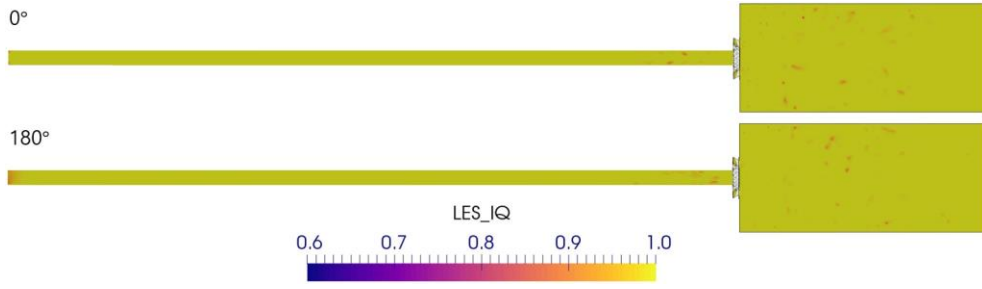
Fig. 3.4. Contours of LES_IQ corresponding to phase 1 (0°) and phase 3 (180°).

The contour of the LES_IQ (LES index of quality) is shown in Fig. 3.4 with different phases (0°, 180°) of oscillating flow fields in the combustion system. Most of the flow fields except a few cells satisfied the LES_IQ > 0.8, indicating the reliability of the current LES. Nevertheless, those cells that did not satisfy the requirement still exceeded LES_IQ > 0.75 condition and are mainly located at the recirculation areas of the burnt gas. Overall, the quality of the current simulation was confirmed through grid independence studies in Figs. 3.3 and 3.4.

3.3.2. Flow response inside the fuel supply line

The flow response inside the fuel supply system is quantitatively investigated using the cold-flow transfer function (CTF). CTF is originally used to identify the fuel injection patterns of the rocket propulsion system [20] and is also used to observe flow responses in the gas turbine combustor [13]. CTF, similar to FTF, is defined as the fluctuation of flow from inlet velocity modulation, and its mathematical formula is shown as:

$$CTF = [U'/U_{mean}]_{outlet} / [U'/U_{mean}]_{inlet} \tag{2}$$

In five forcing frequencies, CTF results were obtained from the integration of velocity profiles in the swirler outlet. The comparison with experimental data [13] was subsequently performed, and the result is shown in Fig. 3.5.
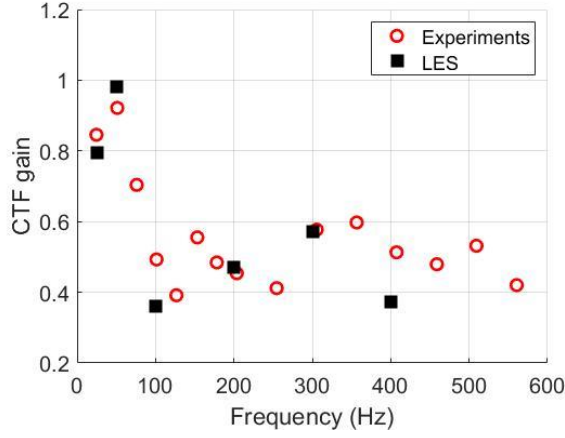
Fig. 3.5. Experimental measurements and LES results for CTF as obtained at the outlet of the swirler.

Figure 3.5 shows the comparison of LES predictions, indicating that CTF gain remained under 1 in most forcing frequencies, which shows the dissipation of inlet fluctuation occurring inside the fuel supply system. The strongest flow response was shown at the frequency of 50 Hz, which does not correspond to the acoustic mode of the fuel supply system or combustor. Compared to the CTF gains in 100 and 400 Hz cases, the local increase was obtained near 300 Hz for both experiment and simulation, where the resonance frequency of 292 Hz coincides with the observed frequency.

The snapshots in Fig. 3.6 show flow oscillations inside the fuel supply system. Figure 3.6a indicates that the lowest mass flow rate to the swirl vanes, and Fig. 3.6b indicates the largest mass flow rate to the swirl vanes (Fig. 3.6c), where the normalized mass flow rate is defined by the equation below.

$$\dot{m}_{normalized} = (\dot{m}_{supply} - \dot{m}_{mean}) / \dot{m}_{mean} \tag{3}$$

where $\dot{m}_{supply}$ indicates the transient mass flow rate, and $\dot{m}_{mean}$ is indicative of the time-averaged mass flow rate to the swirl vane. As shown, the periodic injections through a swirler with the forcing

frequency of 50 Hz were observed. The flow injection through a swirler is non−uniform due to the turbulent boundary layer inside the fuel supply line.
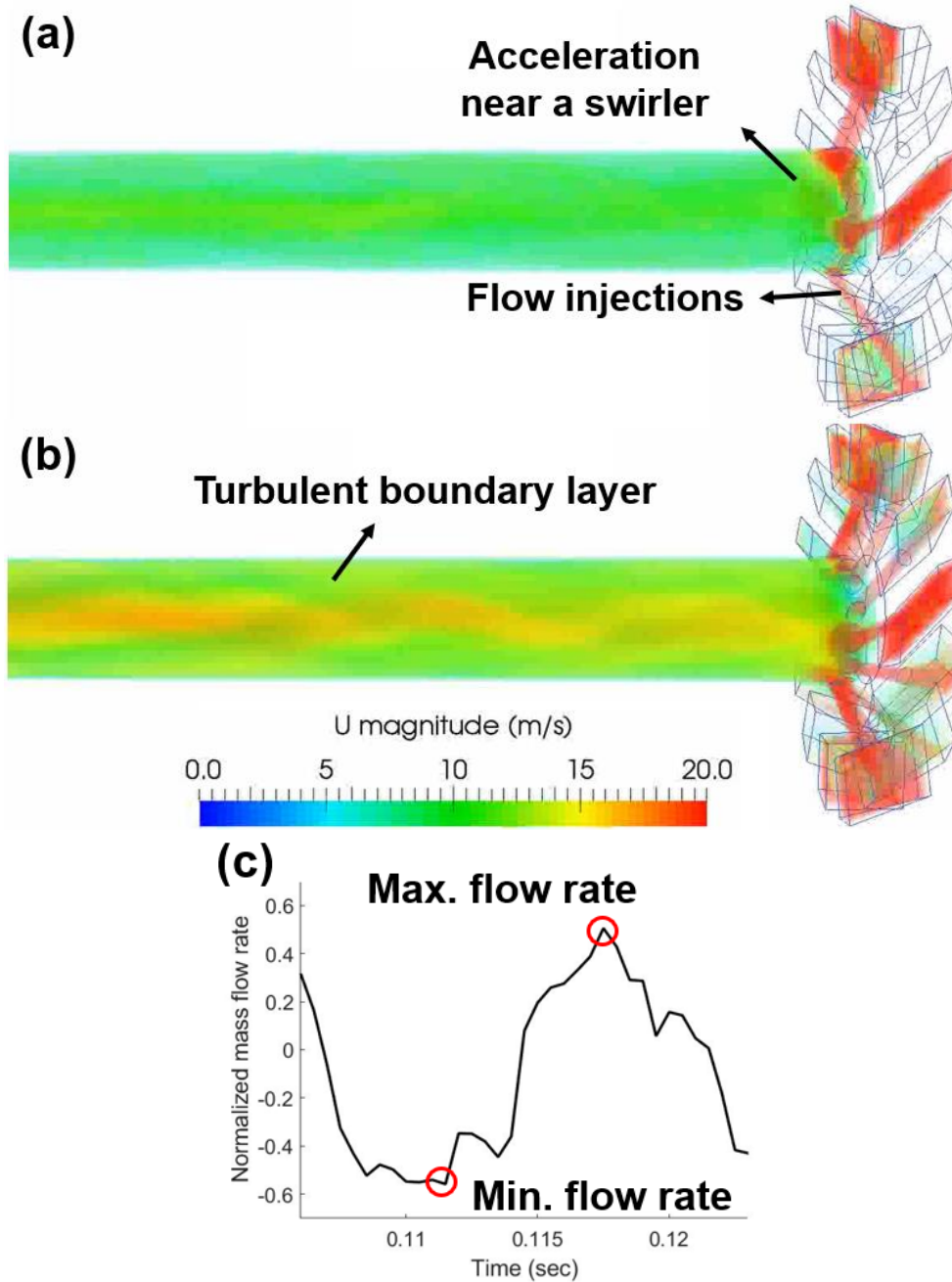
Fig. 3.6.   Velocity distribution inside the fuel supply system shown with the cases of (a) minimum and (b) maximum mass flow rates, shown in (c).

In each region of the fuel supply line, CTF is subsequently measured to figure out the flow responses at each region of the supply line. The modified CTF function is defined at each supply line location of x, which indicates the distance from inlet, as follows:

$$CTF_x = [U'/U_{mean}]_x / [U'/U_{mean}]_{inlet} \quad (x = 30mm, 300mm, 600mm) \quad (4)$$
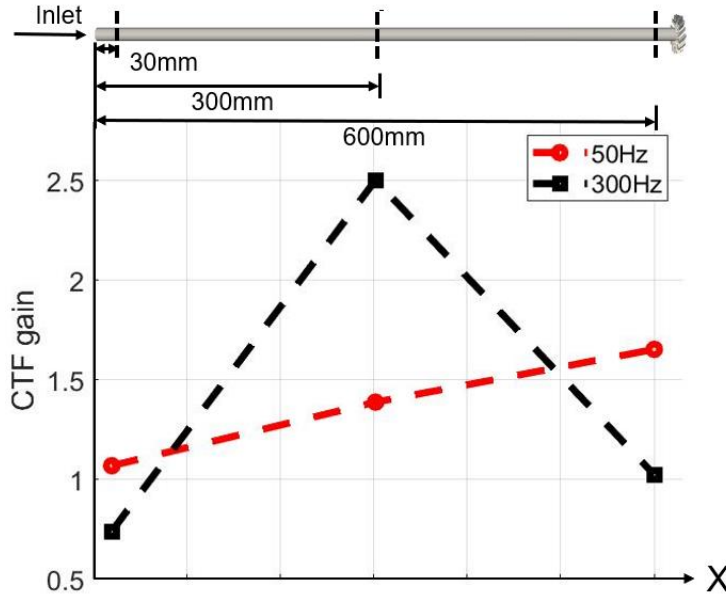
Fig. 3.7.   The flow responses calculated at three different location of the fuel supply line for forcing frequencies of 50Hz (red line) and 300 Hz (dark line).

Figure 3.7 presents the flow responses in each supply line location of 50 Hz and 300 Hz forcing frequencies. Transient velocity profiles were obtained at 3 different locations of 30 mm, 300 mm, and 600 mm, and those values were used to calculate the CTF in each location. Just as in Fig. 3.5, the time-averaged variable (U_{mean}) and the fluctuation magnitude variable (U') were used to calculate CTF. In all locations, CTF gains exceed the values which are obtained at a swirler outlet (Fig. 3.5), which shows that the dissipation of inlet fluctuations mainly occurs during the fuel injection through a swirler. In the 50Hz forcing, the strength of the

4 5

flow response was continuously increased as approached a swirler. This was due to the oscillations induced near the supply line outlet, which is mentioned again at the end of section 3.2. In the middle, CTF gain at the forcing frequency of 300 Hz increased due to the resonance with the acoustics of the fuel supply line.
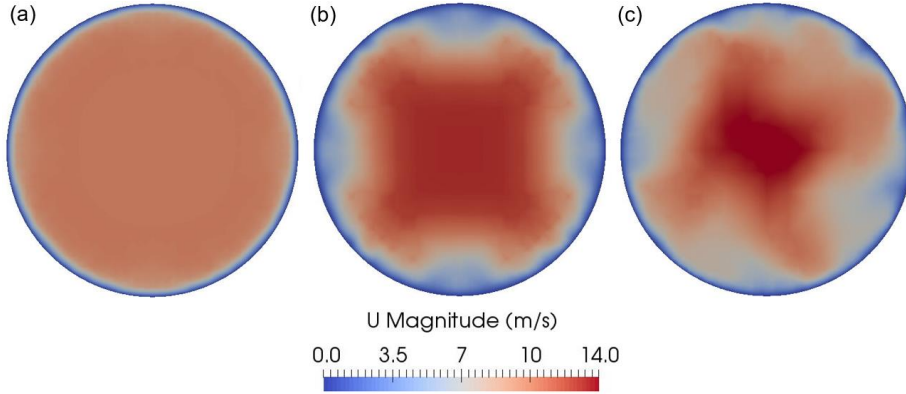
Fig. 3.8. Velocity distribution in the cross−sectional view at the location of (a) 0.03m, (b) 0.3m, and (c) 0.6m from the fuel supply line entrance for a forcing frequency of 50 Hz.

The snapshot in Fig. 3.8 at the multiple locations of the fuel supply line shows the radial cross−sectional view of a fuel supply line. Near the inlet, the flow represents a uniform laminar flow (Fig. 3.8a). As the flow is injected through, the turbulent boundary layer is continuously developed inside the fuel supply line (Fig 3.8b, 3.8c). The supplying flow at the feed line fluctuates with a given forcing frequency, forming an X−shaped pattern (Fig. 3.8b). The injecting flow interacts with the instabilities near the swirler boundary, and it results in the highly non−uniform oscillation shown in Fig. 3.8c. The oscillation at the middle of the supply line is shown more sensitive to 300 Hz input (Fig. 3.7b), while the oscillation at the outlet of the supply line is sensitive to 50 Hz input (Fig. 3.7c).

Figure 3.9 illustrates the cross−sectional side view near the region connected to the entrance of a swirler. Before the injection, supplying flow fluctuates with the 4 oscillation phases of phase 1 (0°), phase 2 (90°), phase 3 (180°), and phase 4 (270°). In

4 6

phase 1, the transport of the flow smoothly proceeded with a high injecting speed. Distortion of the injecting flow was observed at phase 2, which shows the formation of vortices near the edges of the swirler inlet. Vortices were developed at phase 3, impeding the movement of the flow towards a swirler. Generated vortices were fluctuated due to the turbulence inside the supply line and were transported inside a swirler (phase 4). Vortices were collapsed inside a swirler and the supply of the flow resumes again, returning to phase 1. Overall the transient cycle in Fig. 3.9 proceeded with the frequency of 50 Hz, which corresponds to the inlet forcing frequency at the inlet. Due to the fluctuations shown in Fig. 3.9, the velocity response was increased at the supply line outlet, as shown in Fig. 3.7c.
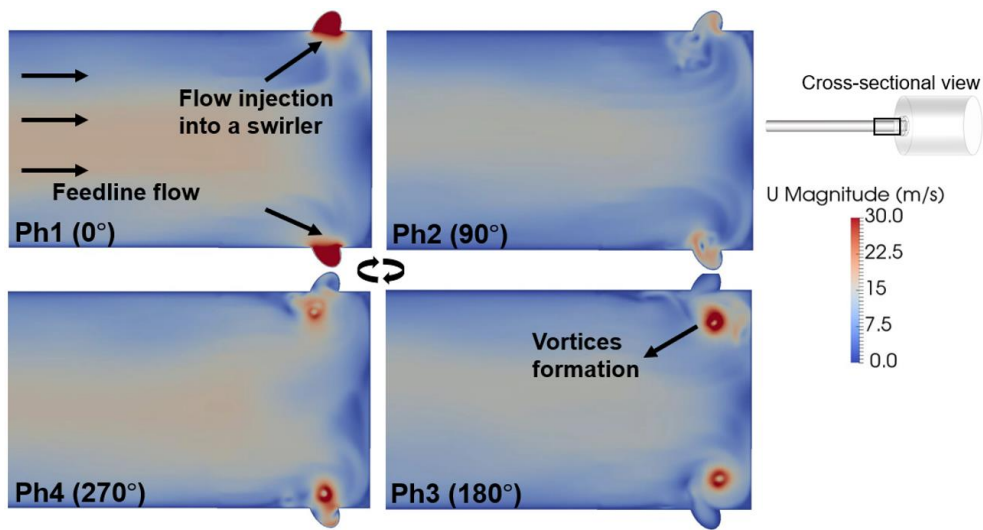
Fig. 3.9. Oscillating vortices shown in the cross−sectional side view near the swirler inlet with the forcing frequency of 50 Hz.

The flow response at the 300 Hz forcing frequency (Fig. 3.7c) was different from Fig. 3.7b. A strong response was observed at the middle of the supply line, which indicates the interaction of forced flow with the resonance frequency of the supply line. The increased response was noticeably dissipated near the swirler inlet. Dissipation of input fluctuation was continued during the injection,

resulting in the low CTF gain at the swirler outlet. This shows that the acoustic effect is dominant inside the fuel supply line. Also, instabilities near the swirler inlet suppressed the input fluctuations at 300 Hz, resulting in a weak flow response at the outlet. The fluctuation of vortices near the swirler inlet was observed, but not in the given forcing frequency. Its characteristics were similar to the naturally occurred vortices inside the fuel supply line, which was further investigated in section 3.3.

3.3.3. Flow response without external forcing

LES result without external forcing was subsequently carried out. Therefore, uniform mass flow rate of 0.0236 kg/s was set at the supply line inlet. Even without the input fluctuations, the internal instabilities inside the fuel supply line were observed. The instantaneous snapshot was shown in Fig. 3.10, which represents the oblique view of the computational domain. Internal instabilities were captured inside the fuel supply system including acoustic wave. Interestingly, even without external forcing, periodic feeding into a swirler was also shown due to the internal instabilities. The strength of the acoustic wave is preserved as the right end of the fuel supply line is blocked by the rigid wall. Oscillating vortices were observed at the edges near the swirler inlet, which block the flow entering the swirl vanes. Periodic feeding into a swirler, which was self-induced inside the fuel supply system, was also shown in Fig. 3.6. The frequency spectra of internal oscillations were described using fast-Fourier-transform (FFT) (Fig. 3.11).
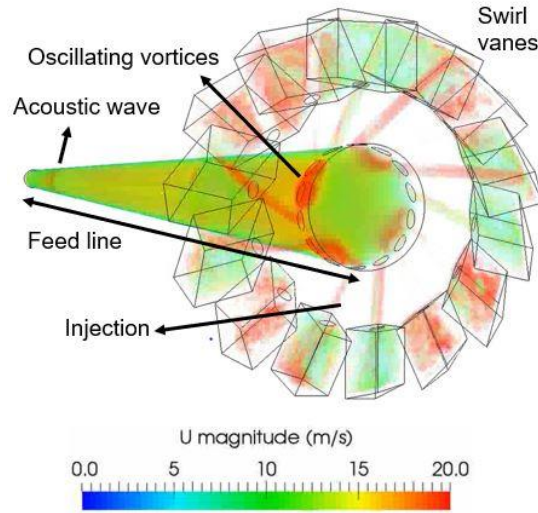
Fig. 3.10. Oblique view of the flow distribution in the fuel supply system in the case with no forcing.
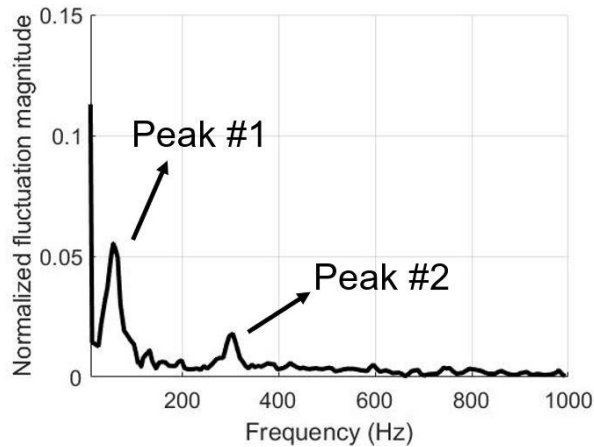
Fig. 3.11. FFT spectrum of the flow rate at the outlet of a swirler without forcing.

At the FFT spectrum, velocity oscillations at the outlet of a swirler were normalized with mean velocity magnitude. Two characteristic oscillations were shown to consist of peak #1 from periodic feeding and peak #2 from the fuel supply line acoustics. The oscillation frequency of peak #1 was shown at the f ≈ 50 Hz and the frequency of peak #2 was shown at the f ≈ 300 Hz. The peak #1 frequency implies that the maximum value of CTF gain near 50 Hz (Fig. 3.2) was obtained by the interaction of internal

4 9

oscillation and input velocity fluctuation. The peak #2 frequency was similar to the natural frequency of the fuel supply line which was calculated as 292 Hz. This implies that the peak #2 oscillation was formed due to the acoustic wave in the fuel supply line. Weak oscillations were also found at frequencies other than the two peaks, which were mainly resulted from the chaotic oscillations of the turbulent boundary layer.
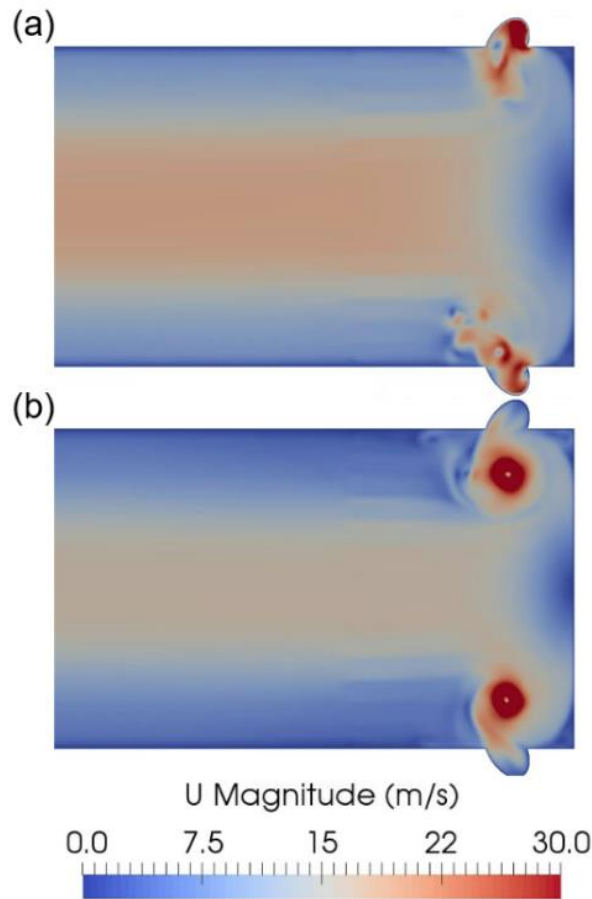
Fig. 3.12. (a) Decaying and (b) strengthening of vortices near the swirler inlet in the case without external forcing.

Figure 3.12 shows the instantaneous snapshots of the internal instabilities near the swirler inlet. Periodic feeding and vortices formations were similar to Fig. 3.9, where the phase of Fig. 3.12a represents phase 1 and the phase of Fig. 3.12b represents phase 3

of Fig. 3.9. As shown, the overall process by which the vortices impeded the flow injection was similar to the results obtained in 50 Hz inlet forcing. Compared to Fig. 3.9, the movement of the vortices was more stable due to the absence of external forcing and a decrease in turbulence level. The frequency corresponding to one period is around 50 Hz, confirming that the oscillations of peak #1 are induced by the complex geometry of the fuel supply system. Obtained FTF inside the combustor represented similar characteristics to CTF as described in following section.

3.3.4. Reacting flow: mean flow field
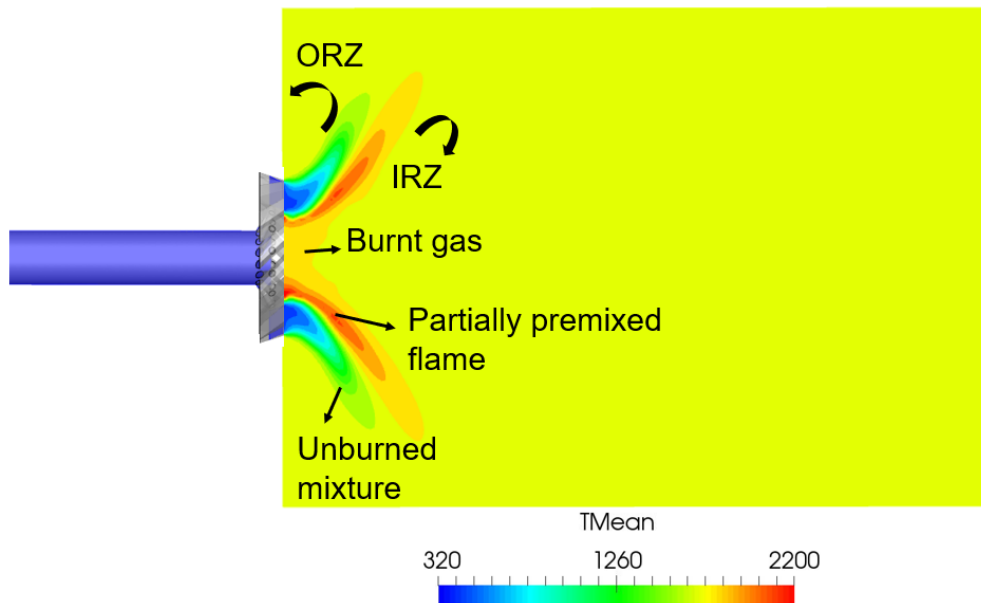
Fig. 3.13. Mean temperature profile inside a combustor.

Turbulent swirling flame in a combustor was simultaneously computed with the fuel supply system. In each simulation result, time-averaged profiles were shown almost the same since the mean value at the inlet was fixed. The contour of the mean temperature shown in Fig. 3.13 describes the structure of the flow field in the combustor. As described in Fig. 3.1b, fuel is injected in the jet-in-crossflow from inside a swirler. The injected fuel is pushed through the combustor by the supply of air. Due to the imperfect mixing, part of the air was injected into a combustor

separately and forms an unburnt mixture area right next to the flame. The mixing of fuel and air mainly progressed in the shear layer between the unburnt mixture zone and flame, causing an active burning and heat−releasing in the corresponding area. The maximum temperature of the flame was shown at around 2200 K near the combustor dump plane. The flame temperature gradually decreases closer to the wall due to the consumption of fuel and low wall temperature. Inner recirculation zones (IRZ) and outer recirculation zones (ORZ) were formulated through the wall, and the supply of burnt gas takes place through them. Burnt gas was stagnated in the middle of the combustor dump plane due to the continuous recirculating flow from IRZ. The temperature of stagnated burnt gas was around 2000K, and its high temperature contributes to the ignition of the supplying flow.
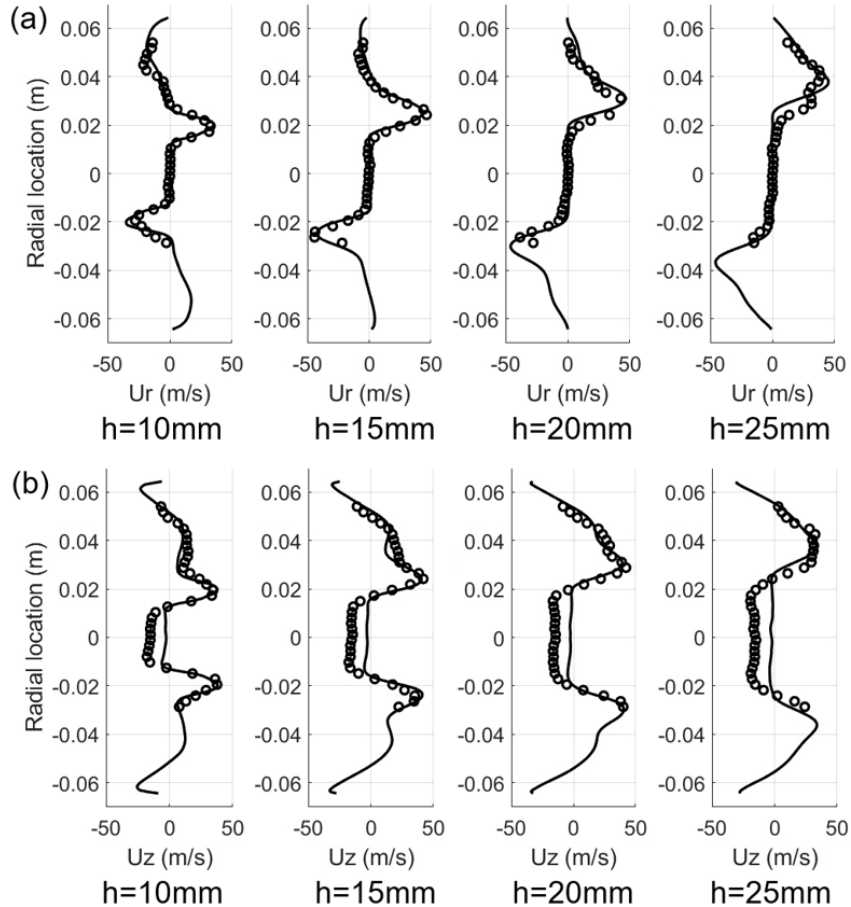
Fig. 3.14. Profiles of the time-averaged (a) radial and (b) axial velocity components for the current simulations (lines) and experimental measurement (symbols), where h indicates the axial distance from the combustor dump plane.

PIV measurement was conducted in the experiment [12], and a quantitative comparison with the current calculation was performed in Fig. 3.14. Comparisons of the mean velocity components were conducted at different axial locations of the combustor using velocity components in the current LES. The results show that the simulations accurately reproduced the velocities of injecting fuel and air mixtures, which are located in the radial location from 0.02 m to 0.04 m. The simulations also captured the recirculating flows near the combustor wall. The reverse flow at the center of the combustor was weakly reproduced in the current simulation since the current work did not consider the acoustic boundary at the combustor outlet, which was considered in the previous PIV experiment.

3.3.5. Reacting flow: flame transfer function

In this section, dynamic flame responses inside the combustor and relevant FTF are explained. The unsteady heat fluctuation caused by the inlet acoustic forcing (Table 3.1) was obtained inside the combustor to calculate the FTF. The distributions of OH mass fraction inside a combustor are presented in Figs. 3.15 and 3.16 to investigate the behavioral characteristics of the flame. Figure 3.15 shows the flame response of the 50 Hz inlet forcing, and Fig. 3.16 shows the flame response of the 300 Hz inlet forcing. The flow injected from the swirl vanes was ignited in the combustor and forms the M-shaped swirling flame near the dump plane. The injecting flow rate through the combustor fluctuates as the outlet of a swirler connects to the combustor. The variations of the flame were shown in 4 different phase angles. For phase angle from 0°	to 180°, flames were stretched forward and interacted with the rigid wall of the combustor. After reaching to the wall, the flame

rotated through the IRZ and ORZ inside the combustor. From 180°
to 270°, the flames were shortened as the flow rate through the
combustor decreased. In all phases, the flame angles fluctuated, but
it did not affect the overall flame structures. Compared to Fig. 3.16,
the flame responses in Fig. 3.15 showed stronger fluctuations in
terms of flame length variation and interactions with the wall due to
the periodic injections induced and amplified in the fuel supply
system. As outlet of the combustor is set as an outflow condition,
thermoacoustic effects were not generated in the combustor.
Therefore, the different oscillations were originated from the
instabilities in the fuel supply system, which was quantitatively
measured as CTF.
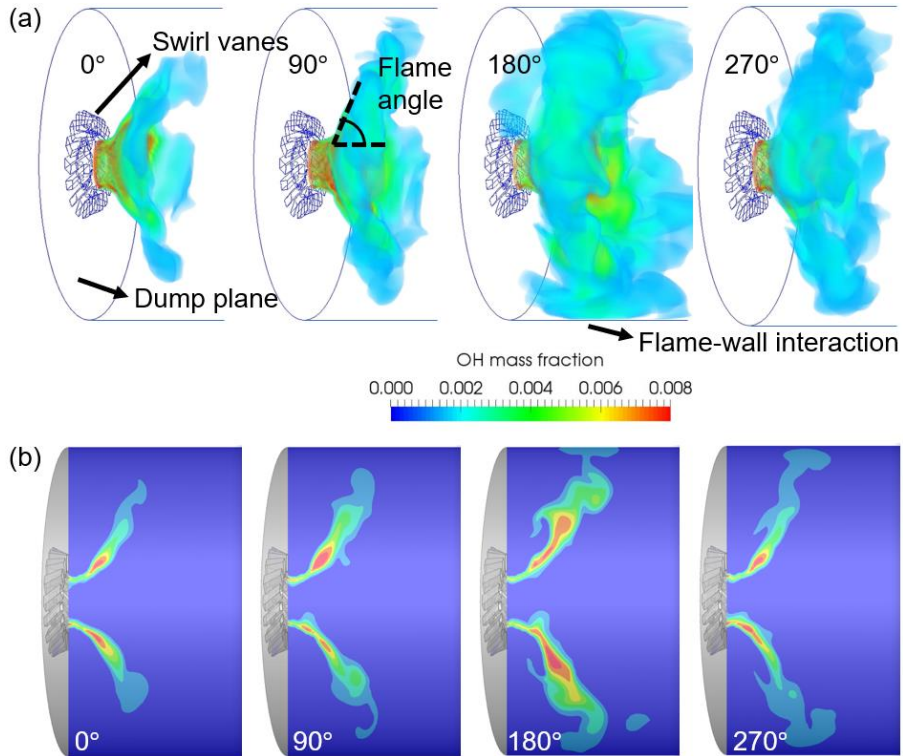
Fig. 3.15. Instantaneous OH mass fraction fields for four different
phases of 0°, 90°, 180°, and 270° for 50 Hz forcing frequency
shown in (a) 3-dimensional view and (b) yz plane in a combustor.
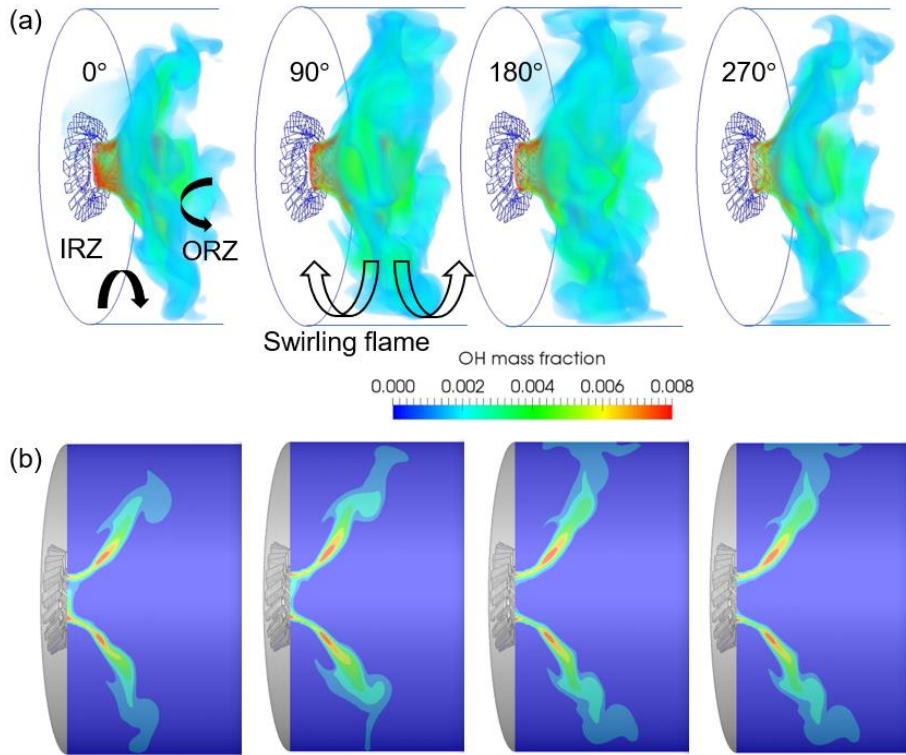
Fig. 3.16. Instantaneous OH mass fraction fields for four different phases of 0°, 90°, 180°, and 270° for 300 Hz forcing frequency shown in (a) 3-dimensional view and (b) yz plane in a combustor.
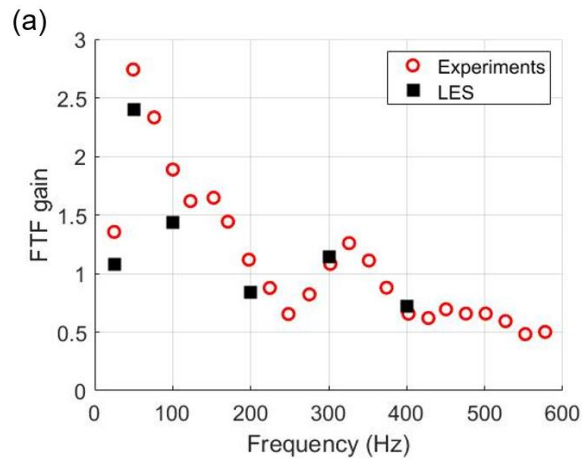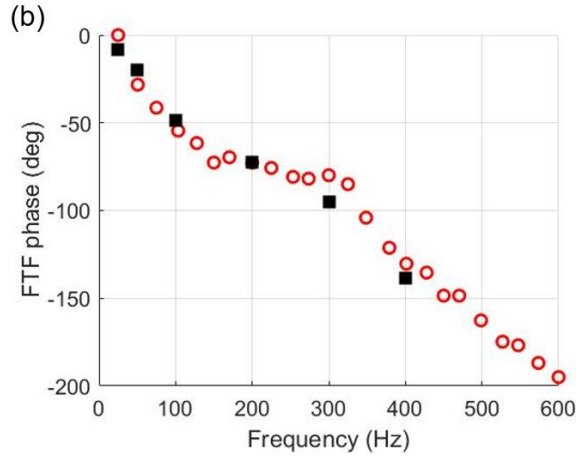
Fig. 3.17. (a) FTF gain and (b) FTF phase predicted by LES
compared with experimental results.

The FTF results are shown in Fig. 3.17, plotted together with the previous experimental results. The FTF in the LES was obtained by integrating the heat release rate calculated in the simulations. FTF gain and phase calculated in this work showed a good agreement with the experimental measurements [12]. The overall gain profiles were a little underestimated in the LES, but still showed similar characteristics to the experiment. The gain profile at 50 Hz exceeded 2, showing a rigorous flame response in the combustor. Both FTF and CTF in Fig. 3.2 describe the maximum gain at f = 50 Hz, which results from the amplified periodic injections with the interaction of forced flow. Therefore, the internal instabilities near the swirler inlet shown in Figs. 3.6 and 3.9 were confirmed as the main cause of flow/flame responses. The inflow oscillation at 50 Hz induces the periodic flame-wall interactions near the rigid wall, which induces intense heat release fluctuations inside the combustor [21]. Local maxima were also shown at 300 Hz, but not as high as represented in the experimental result. Both previous experimental findings in [12] and the current numerical investigation (Fig. 3.17) indicate that the acoustics of the fuel supply line is the main reason for the increase of gain at 300 Hz. The local maximum frequency in Fig. 3.17 showed a slight discrepancy with the resonance frequency of 292 Hz. This is

5 6

because the resonance frequency is determined based on the length of fuel supply system and the sound speed of injecting fuel. In both LES and experiment, the preheated air at 200° C is mixed with the air in the swirler, resulting in the increase in the sound speed as well as the noted discrepancy in the peak frequency. Also, the FTF phase calculated in LES showed a high degree of agreement, implying that the entire process from fuel supply to ignition was properly simulated. Naturally occurred oscillations inside the combustor, like fluctuations of the flame angle, were not affected on LES results due to its weak amplitude compared to the inlet fluctuations.

3.4. Conclusions

The effects of fuel supply driven instabilities on the partially premixed flame responses are investigated using three－dimensional LES. The two transfer functions namely CTF and FTF are deduced to study the flow and flame response behaviors. The fuel supply system considered in this work consists of the supply line, 14 injectors, and a swirler. The gaseous fuel is supplied through a cylindrical supply line and is injected into the swirler. The injected fuel is partially premixed with air inside the swirler and is supplied in the combustor, forming a partially premixed flame. The results show the formation of the geometry－induced vortices near the edges of the swirler inlet. Those vortices are periodically generated and collapsed, impeding the flow injection into the swirler. Such oscillations induced by the periodic injection occurs at 50 Hz, which coincides with the peak frequency of the CTF. The peak frequency of 50 Hz does not correspond to the natural resonance frequency of supply line, implying that the periodic injection process is the only cause of such flow response. The oscillatory fuel supply resulted in a rigorous fluctuation of flames and the subsequent increase of the FTF gain. Thus, the fuel supply driven instability has a direct impact on the FTF and CI in the partially premixed combustor, considered for this investigation.

Chapter 4. Multiple premixed combustors

4.1. Background and motivation

Thermoacoustic instability occurs when the heat release perturbation from a flame is coupled with the acoustic mode of the gas turbine combustor. It is a major cause of damage or noise generation during a combustion engine operation. In the past several decades, studies have been conducted to analyze and to provide preventive measures to suppress the instability. Related studies have focused on the can combustors, where the hydrodynamic instability [1,2], acoustic mode [3,4], equivalence ratio [5,6], fuel composition [7,8], and swirl number [9,10] have been identified as the significant factors that can stabilize or destabilize the combustion operation.

While most of the experimental and numerical researches were focused on single can combustors or annular type combustors, the industrial applications utilize the can-annular type combustors composed of multiple can combustors inside the heavy-duty gas turbine engine. The combustion dynamics of a can-annular type can be quite different from that of a single can combustor [11]. On the downstream side of the can-annular combustor, there is a cross-talk area connecting each combustor. The cross-talk plays the role of mixing of the exiting burned gas from combustion to equilibrate the temperature of the combustion products. However, the pertinent flow field as well as the pressure waves can interact closely inside the cross-talk, which can lead an instability mode transition.

The previous experimental work in [12] demonstrated that a push-push mode vibrating in the same phase in each combustor or a push-pull mode vibrating in a different phase in each combustor occurs due to the presence of the cross-talk in the can-annular combustors. However, a limited number of analytical or numerical investigations are available regarding thermoacoustic instability in

the can-annular combustors. Ghirado et al. [11] proposed a low-order model for acoustic mode analysis of multiple can combustors connected by the cross-talk and predicted the effect of mutual synchronization between the combustors on the axial and azimuthal instability modes. The effect of the distance between combustors on the coupling strength in the low-frequency instability region was analyzed. The related study [13] considered the can-can coupling using a low-order model and observed the effects of flame saturation nonlinearity and mode localization on the nonlinear mode shape. Farisco et al. [14] performed large eddy simulation (LES) with the cross-talk and investigated the can-to-can interaction using a non-reacting cold flow assumption. Their results demonstrated that the cross-talk effect does exist, and one cannot ignore such effect in the simulation of the combustion instability in a can-annular system which was yet to be done at the time. Thomas et al. [15] also numerically studied the effects of external fluctuations in the two coupled thermoacoustic oscillators. They have confirmed that the increase of the noise intensity induces the sudden drop of pressure oscillations and causes the amplitude death. Based on the literature review, no LES study has been reported on the can-annular combustors with a detailed chemical reaction model of methane-air mixture. For providing a detailed insight into the occurrence of thermoacoustic instabilities in can-annular combustors, the present study focuses on the full LES of self-excited thermoacoustic instability with consideration of combustion and thermoacoustic feedback processes.

As for a single can type combustor, there have been reported full LES results in the past for considering the thermoacoustic instability. For example, Franzelli et al. [16] performed LES of thermoacoustic instability in a single can combustor and demonstrated that simulations considering the mixing zone can produce accurate results in the unstable operating condition. Lourier et al. [17] simulated the thermoacoustic instability in the single can combustor and compared well with the experimental results of oscillations. Kraus et al. [18] performed LES with heat

conduction effects and predicted the thermoacoustic instability in a swirl burner. Nam et al. [7] performed LES in a single can combustor in hydrogen-enriched methane fuel conditions, and predicted the thermoacoustic instability in various operating conditions. The prediction of thermoacoustic instability in a ring-shaped annular type combustor, which is mainly used for aircraft engines, was given. Chen et al. [19] performed LES of the partially premixed flame and investigated the role of the precessing vortex core (PVC) on driving thermoacoustic oscillations in a gas turbine combustor. Noh et al. [20] conducted a joint study of LES and experiment and successfully simulated the phase-resolved flame structure from thermoacoustic oscillations. Zettervall et al. [21] calculated thermoacoustic instability in an annular combustor where the features of the flame structure and pressure oscillations in the combustor were identified. The thermoacoustic instability of a liquid spray fueled gas turbine combustor is also successfully captured [22] using the LES Euler-Lagrange approach with liquid fuel/wall interaction model. Nevertheless, the LES results on thermoacoustic instabilities from the literature corresponded to the single cylindrical can combustors or at times the annular combustors. While many of the real heavy-duty gas turbine engines stem from their can-annular combustors, it is essential to perform the full LES on the can-annular type gas turbine combustors.

Based on the earlier computational attempts to understand combustion instability in can-annular combustors with the cross-talk, the objective of the present study is to expand the feasibility of LES together with high-fidelity turbulent combustion models and to capture the self-excited instabilities in the can-annular combustors with the chemical reactions considered. Here, two premixed combustors connected to the cross-talk are designed and considered numerically. A swirl-stabilized premixed flame is generated in each combustor while the acoustic effect is induced by a blocked outlet. The LES of a swirling flame is performed with the wall-refined meshing for resolving turbulence. Subsequently, a full turbulence-chemistry coupling is attempted which is intended to

enable a high-fidelity combustion simulation at sub-grid scale. The simulations under both symmetric and asymmetric conditions are enforced in order to clarify the role of symmetry in stabilizing or destabilizing the combustion system. The apparent role of the cross-talk on combustion instability is explained while the results are compared with our experimental measurements for the validation of the LES results.

4.2. Numerical approach

In this work, the complex combustion system of two identical lean premixed combustors connected to the cross-talk are considered (Fig. 4.1). The experimental work in [12] dealt with longitudinal-mode combustion instability in two adjacent combustors.
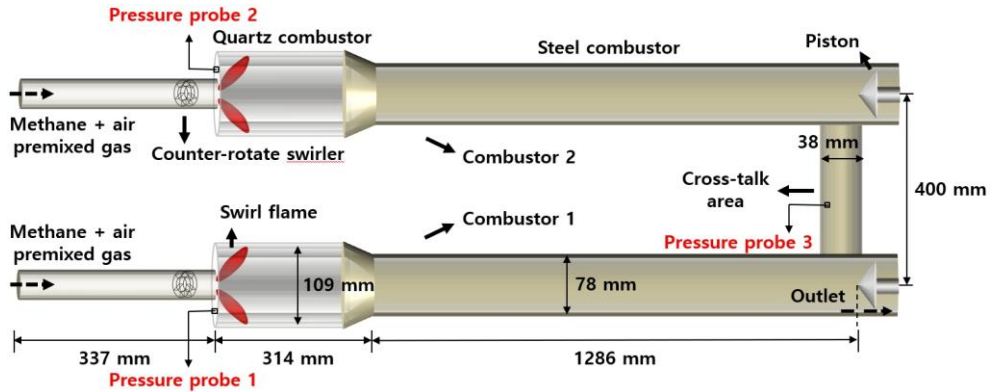
Fig. 4.1. Schematic of can-annular gas turbine combustors.

The premixed methane-air gas mixture was supplied in the preheated condition using two 30-kW electric heaters. The inlet sections consist of the 337 mm long supply lines and annular cross-sections with a 38 mm diameter inner mixing tube and a 25 mm diameter outer center body. The flow was choked at the inlet of the fuel-oxidant mixing region, which served as the acoustic boundary of the combustors. Two identical counterclockwise axial swirlers with a swirl number of 0.48 were located at the nozzle of

each combustor, from which a swirling flame was formed and flame stabilization was achieved. A quartz tube with a radius of 109 mm and an axial length of 314 mm was used at the inlet of the combustor, and the CH* chemiluminescence was measured in the section. The combustor was made of stainless steel, and high-velocity jet impingement of room temperature air was performed to cool the combustor. Additionally, 80.5% of the area at the end of the combustor was blocked by a piston, resulting in the isolation of acoustic effects inside the combustor. The other outlets were exposed to ambient air at an atmospheric pressure. PCB model 112A22 pressure transducers were located in the dump plane and the cross-talk, and they were used to measure the pressure oscillation during combustion. The experiment was conducted at various equivalence ratios, and some of the results were used for verification of the numerical simulation.

For the simulation, the compressible Navier-Stokes equations that consisted of Favre-averaged mass, momentum, energy, and species equations were adopted. The LES model was used to simulate swirl-stabilized premixed flames generated inside the combustors, and accordingly, large-scale eddies were directly calculated and small-scale eddies were modeled using a turbulence model. Thus, the wall-adapting local eddy-viscosity model [23] was utilized for the subgrid-scale viscosity term to allow a proper closure to the governing system, and the subgrid-scale viscosity was modeled.

The premixed mixture supplied to the combustor was assumed to be ideal gas, and the viscosity of the gas was calculated as a function of temperature using Sutherland's viscosity law. The enthalpy and specific heat of chemical species during the exothermic reaction process were modeled using NASA polynomials based on tabulated constants. In addition, Fick's law for diffusion and Fourier's law for heat conduction were used for the simulation of mass and heat transfer of gas mixtures. The diffusivity of species is approximated by calculating bulk species diffusivity with unity Lewis number assumption.

A combustion model consisting of 15 species and 23 reaction steps [24] was applied for the full reaction of methane−air premixed gas to calculate the reaction and heat release rates of the combustion process. Turbulence-chemistry interaction modeling was additionally performed to simulate the highly nonlinear small−scale reactions during turbulent combustion. Modeling was performed using a PaSR model [25], and accordingly, the calculated cell was divided into a reaction zone and non−reaction zone. In the model, the concentration of a species i and related equations are written as follows:

$$\frac{dc_1}{dt} = \frac{c_1 - c_0}{\Delta t} = \frac{c - c_1}{\tau_m} = \dot{w}_i(c) \tag{1}$$

$$c_1 = c(\frac{\Delta t}{\Delta t + \tau_m}) + c_0(1 - \frac{\Delta t}{\Delta t + \tau_m}) \tag{2}$$

In above equations, c_1 and c_0 are the concentrations at the inlet and outlet of the cell, Δt is the numerical time step, τ_m is the turbulent mixing time, and $\dot{w}_i$ is the production rate of the species i. From the Eqs. $(1)-(2)$, a generalized model equation is drived:

$$\dot{w}_i(c) \simeq \dot{w}_i(c_1) + \frac{\partial w_i}{\partial c}\Big|_{c=c_1}(c - c_1) = w_i(c_1) - \frac{c - c_1}{\tau_c} \tag{3}$$

$$\frac{c_1 - c_0}{\Delta t} = w_i(c_1) \cdot \frac{\tau_c}{\tau_c + \tau_m} \tag{4}$$

where τ_c is the reaction time scale.

For the transient term of the governing equations, a second−order semi−implicit Crank-Nicolson scheme was used for time integration. A one−step monotonic scheme with a flux limiter was applied for convective flux to capture the pressure waves inside the combustor, while a second−order central difference scheme was applied for diffusive flux. The compressible pressure−implicit with

splitting of operators (PISO) algorithm was used to effectively handle the pressure-velocity coupling in the governing equation. The 4th order implicit Rosenbrock method [26] is used for integrating chemical kinetic ordinary differential equations. The Courant number in the simulation was less than 0.4, and the resulting computational time step became $\sim 1.5 \times 10^{-8}$. The wall-clock time required for the calculation of combustion instability is about 4 weeks for one case. Mentioned equations and numerical models are employed in the in the open-source semi-implicit finite volume code OpenFOAM 4.1 for simulation. In particular, unsteady compressible solver rhoReactingFoam is used in this study. The code has been used for the study of turbulent flame and thermoacoustic instability in the gas turbine combustor, which was shown to reproduce the experimental data in [19, 21], and thus additional code validation is not deemed imperative in the present work.

　　The simulations were performed based on the operational conditions of outlet and the presence of the cross-talk. The specific details on each case of simulations are listed and explained in Table 4.1.

Table 4.1. Inlet conditions for each computational test.

Case	1	2	3	4
Combustor outlet	Open	Closed	Closed	Closed
Number of combustors	1	2	1	2
Equivalence ratio	0.65	0.65	0.65	0.65
Mean inlet velocity (m/s)	50	40	40	40
Inlet pulsation	Off	Off	Off	On
Inlet temperature (K)	473	473	473	473
Wall boundary condition	Isothermal, No-slip	Isothermal, No-slip	Isothermal, No-slip	Isothermal, No-slip

　　For flame structure analysis, the open condition in Case 1 considers the injector, swirler, and combustor with the atmospheric outlet condition at ambient pressure applied at the exit of the combustors. A schematic of the combustor in the open condition is

presented in Fig. 4.2a. The simulation result in Case 1 shows the premixed flame without the acoustics where the comparison with the experimental measurement in the same condition is considered. As for the simulation of combustion instability, the closed conditions of Cases 2 through 4 with injector, swirler, cross−talk, and combustors were considered in a whole system in Fig. 4.1. Moreover, in order to examine the effect of the cross−talk, a single combustor with a closed outlet without the cross−talk was considered and illustrated in Fig. 4.2b.
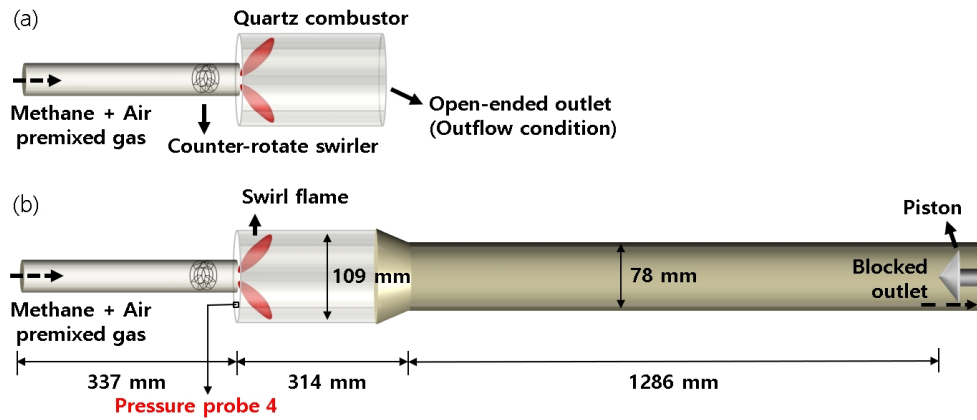
Fig. 4.2. Planar schematic of a single gas turbine combustor in the (a) open condition of Case 1 and (b) closed condition of Case 3.

The Reynolds number corresponds to the inlet velocity of 40 m/s was 44,000, and 50 m/s was 55,000. The first grid at the wall was in the region of $y^+<5$ in order to locate the first grid point in the viscous sublayer and to apply no−slip boundary condition. Therefore, local refinements using very fine grids were performed at the near−wall region of the computational domain. A grid size of approximately 1 mm was placed in the injector and swirler regions. Then, an approximately 2−mm grid was placed in the flame and vortex generation regions of the burner. In addition, a 4−mm coarse grid was placed in the region of the combustor where only the acoustic effect was considered as an important factor. Thus, a total of 6 million unstructured grids were used in the simulation. Figure 4.3 illustrates the grid refinement considered in the simulation. The

preheated mixture with a uniform inlet velocity of $\bar{u}$ = 40 m/s without additional turbulence and an inlet temperature of 473 K was applied at the entrance of the injectors. The equivalence ratio of the injected premixed mixture was 0.65, and the mass fraction of methane was set to 0.036. The isothermal wall condition was applied at the wall regions exposed to ambient air, and because of unknown wall temperature, a value of 800 K was assigned which is consistent with the work referenced in [27]. In the wall sections consisting of swirler walls and interfaces of combustor and injector, adiabatic wall condition was applied as the cooling effects from the air did not have to be considered. Computations in this work were performed using the Intel Xeon CPU E5-2637 processors consisting of 192 cores. The wall-clock time required to obtain the results were 20.3 days for the cases of thermoacoustic instability and 3 days for flame structure simulation.
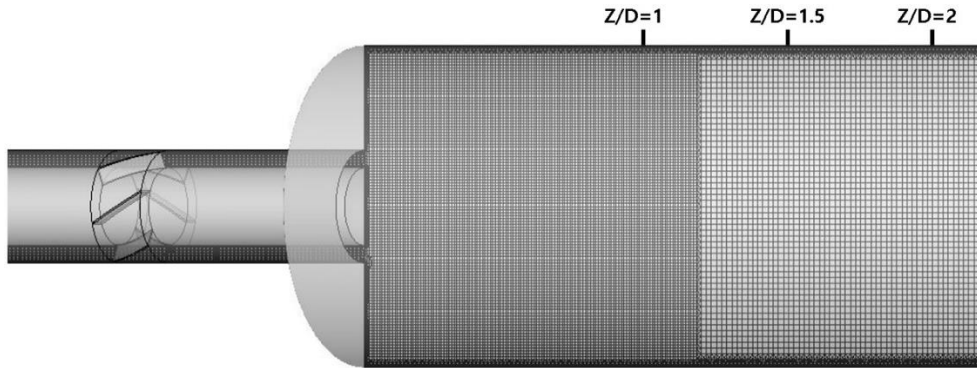
Fig. 4.3. Selective grid refinements for resolving near wall turbulence in the present simulation.

Prior to the full simulation, grid independence test was performed at three-grid levels including the selected grid (6 million), coarse grid (3 million), and fine grid (12.5 million). The combustion instabilities in the combustors (Case 2 in Table 4.1) were simulated, and the results are presented in Fig. 4.4.
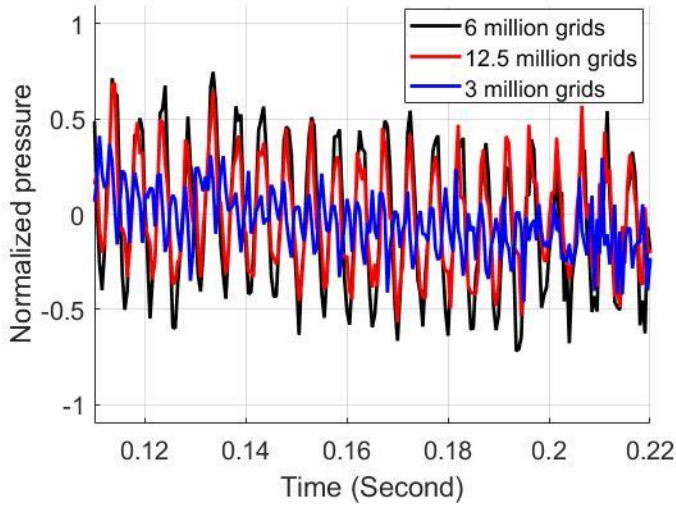
Fig. 4.4. Dynamic pressure comparison inside the combustor (probe 1) for mesh independence test.

According to Fig. 4.4, the finest grid case showed similar oscillation frequency and amplitude in comparison to the selected mesh of the current work. In contrast, the coarse mesh showed the dissipated amplitude and significantly increased oscillation frequency, indicating that the lack of refined grid points resulted in erroneous handling of the feedback loops between acoustics and flame, while the necessary mesh resolution for accurate simulation is suggested by the current mesh set up.

4.3. Results and discussion

4.3.1. Case 1: Single combustor in open condition for validation of LES result

In the open condition, the flame structure simulation is compared with the experiment. The CH* chemiluminescence signal was obtained from the combustor to the axial 0.12 m region. The current combustion model [24] does not consider CH. Since both CH* and OH* intensity represent the rate of heat release during combustion, the calculated OH mass fraction appearing in the same region is compared instead. Fuel was injected at x = 0 region of the

combustor as the premixed flame started to appear at x = 0.02 m region (Fig. 4.5). The time-averaging flame was performed for about 1 second, which corresponds to 180 convective times of the flame. Averaging takes place after the stabilization of flow from 0.05 seconds. The premixed flame was formed as an attached flame near the injector as shown in Fig. 4.5. Due to the formation of swirling flame, a recirculation area appeared in the wall region, apparently noted with the vigorous mixing and rapid reactions. Thus, a large fraction of radicals was generated mostly in the near-wall region. In the experiment, the measurement was performed with a slightly inclined injector, and accordingly, subtle asymmetry was observed in the region of r = 0. However, the agreement between the two images is quite acceptable as illustrated here. An attached flame was observed in both experiment and simulation, mostly in the axial location of 0.02 to 0.06 m. The distribution of high radicals obtained experimentally was closer to the rigid wall than that obtained numerically, which is attributed to the error in reaction rates in the recirculation area near the wall. Since the swirling flame was located in the transparent quartz combustor section (Fig. 4.2), the error of the reaction rates in Fig. 4.5 was caused by neglecting the cooling effects. In the experiment [12], cooling using the high winds outside the combustor was considered to prevent damages from high temperatures.
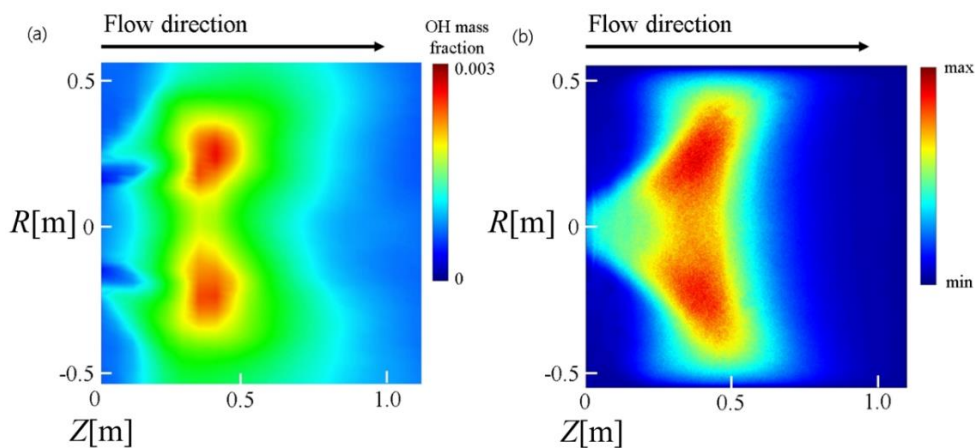

Fig. 4.5. Flame structure profiles in the open condition of Case 1:

(a) calculated OH* mass fraction and (b) experimentally observed CH intensity.

4.3.2. Case 2: A whole system with dual combustors with the cross-talk in closed condition

For the whole system in Fig. 4.1 with closed condition and blocked outlet, the distribution of the time-averaged mean velocity field from the simulation is presented in Fig. 4.6. From the average velocity field in the closed condition (Fig. 4.6), a streamline profile as displayed in Fig. 4.7 was also produced. Due to the high swirl number of the counter-rotating swirler, the direction of the flow changed significantly from the swirler region. Geometry-induced turbulence was induced when the flow passed through the swirler, which caused velocity acceleration inside the injectors. Accordingly, a M-shaped flame was formed, and the burned gas from the flame moved into the recirculation areas and interacted with the near-wall vortices (Fig. 4.7). Some of the burned gas returned to the inlet of the combustor and contributed to continuous ignition of the premixed gas. Other burned gas moved to the combustor exit, resulting in a fast flow rate in the converging section of the combustor. As illustrated in Fig. 4.6, the injection speed increased when the flow passed the swirler due to the effect of high turbulent intensity at the trailing edge. Furthermore, a ring-shaped velocity distribution appeared in the transverse plane (constant Z plane) as the swirling flow occurred. The results indicated that the flow characteristics of both combustors were quite symmetrical.
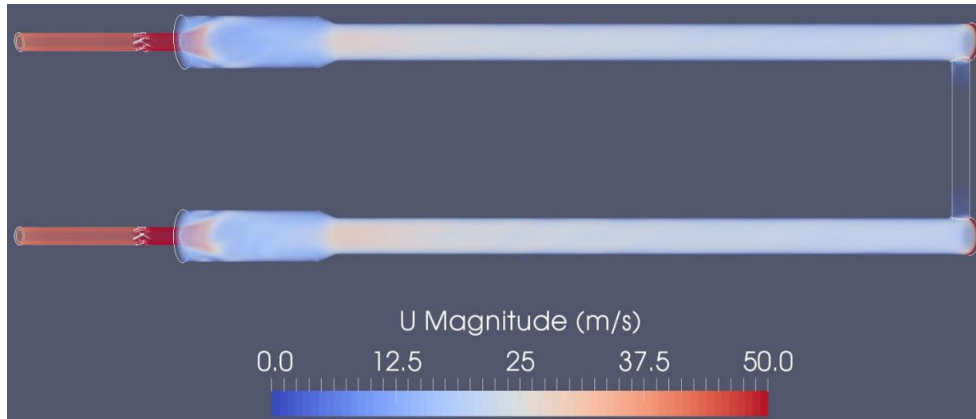
Fig. 4.6. Mean axial velocity profile in the closed condition of case 2.

Similar to the results in the open condition, the recirculation zones appeared in each combustor. The recirculation zones and shear layer predominately occurred in the combustor upstream region, and inner and outer recirculation zones were identified. The outer recirculation zones were located at the corners of the combustors and consisted of one large vortex and one very small vortex. Flames were mainly generated in this region, and burned gas occurred from combustion circulates in the near−wall region. The toroidal inner recirculation zones were located in the central part of the combustors and consisted of two main large vortices. In each combustor, the recirculation zones appeared similarly with a little asymmetry of vortex structure. This asymmetry was caused by the gravity force applied at the body force term in momentum equation, which causes the flow to move downside of the combustor.
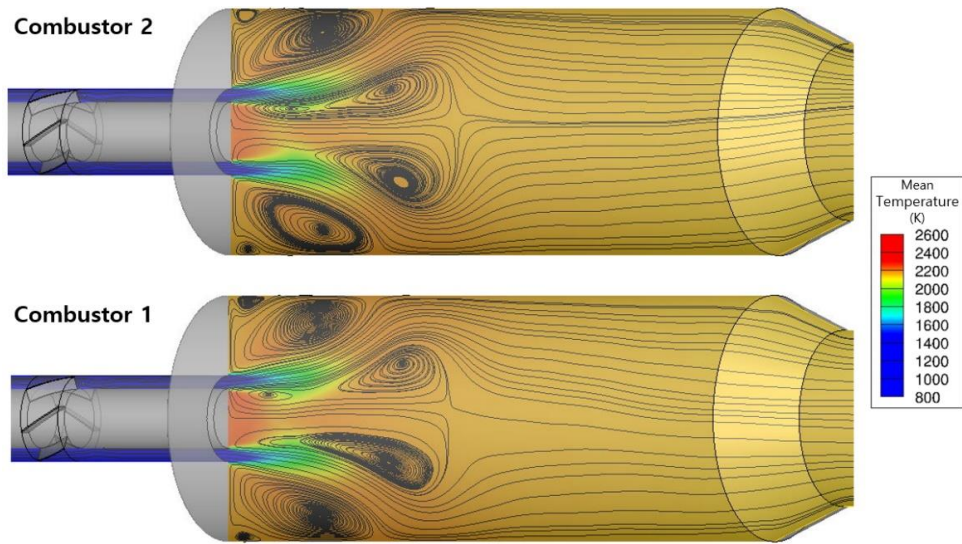
Fig. 4.7. Symmetric streamlines plotted together with the mean temperature background.

The quantitative depiction of the average velocity distribution inside each combustor (Fig. 4.8a), and the root−mean−square (rms) velocity fluctuation (Fig. 4.8b) at various locations at the inlet of the combustor is given. As both combustors had the same inlet velocity and geometry, the average velocity distribution in each combustor was shown nearly identical. In the region close to the combustor entrance, vortices due to the formation of a recirculation zone were located on the wall, and accordingly, a faster axial velocity distribution was located in the near−wall region. In contrast, in the central part of the combustor, inverse flow with slow velocity was generated toward the inlet part due to the influence of the inner recirculation zone. Near the converging section of each combustor, the flow suction occurred in the centerline due to the influence of the geometry, and the suction speed increased near the converging region. As the effect of the recirculation region decreased, the near−wall velocity was relatively slow. The rms velocity fluctuation in each region also appeared similar in each combustor but differed from the mean velocity profile because the combustion instability amplitude in each combustor was slightly different. The rms velocity fluctuation at

Z/D = 1.0 exhibited similar values in all regions, which implied that the fluctuation of the centerline recirculated flow was much stronger than its mean value. In the regions of Z/D = 1.5 and Z/D = 2.0, relatively low rms fluctuation values appeared as the distance from the injector increased. As the location approached the converging section of the combustor, the fluctuation value became very large, signifying that the pressure oscillation had a strong influence on the flow suction phenomenon.
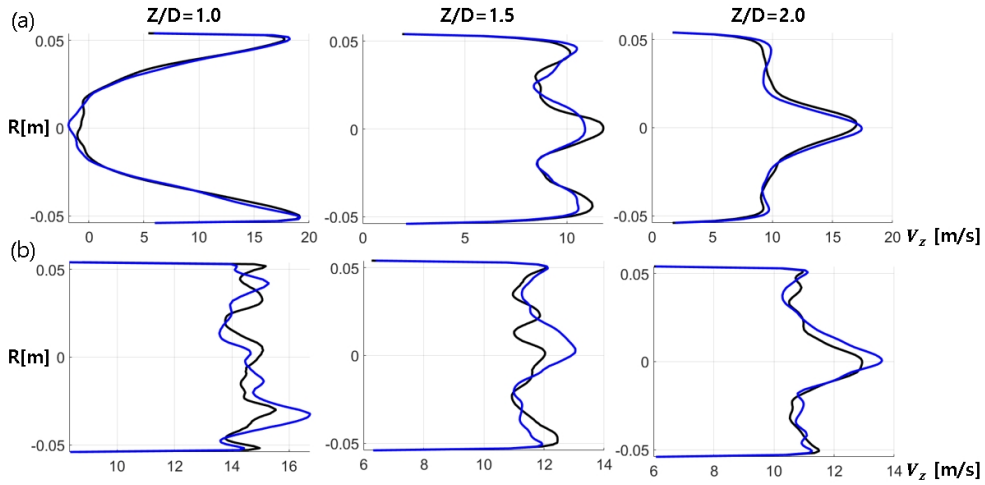
Fig. 4.8. Profiles of (a) mean and (b) root-mean-square fluctuations of axial velocity for transverse planes of combustor 2 (black line) and combustor 1 (blue line) at three axial distances, Z, with respect to the combustor diameter, D, where R indicates the radial location.

Intense pressure oscillations were observed in the two combustors and in the cross-talk due to thermoacoustic coupling. The fast Fourier transform (FFT) results of the pressure oscillation in probes 1 and 2 (Fig. 4.1) are presented in Fig. 4.9. FFT was performed based on the calculation results up to 0.2 seconds. Dynamic pressure data was measured at each probe at a sampling rate of 1000 Hz. The FFT results of the pressure oscillation measured by the pressure transducer overlapped with the numerical profile. In both the experiment and simulation, perturbation

occurred at a frequency of approximately 200 Hz, which is similar to the fundamental eigenmode of the combustor [12]. A lower perturbation amplitude generated in the numerical results than in the experiment. It was attributed to the underestimation of the flame−wall interaction as the isothermal wall condition was assumed in wall sections of cylindrical combustors. The neglection of the wall cooling effects of the combustor wall also causes this difference in heat release fluctuations and sound speeds of the actual experiment, which causes the higher oscillation frequency in simulation.

The pressure perturbation in probes 1 and 2 appeared in a similar amplitude in each combustor, which was consistent with the push-push mode reported in the experiment.
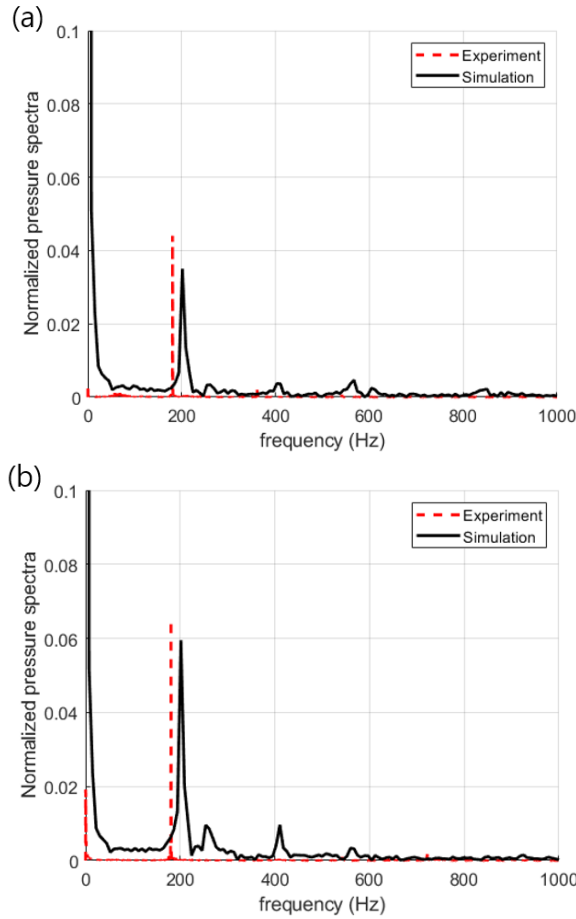

Fig. 4.9. Fast Fourier transform results of pressure oscillations

measured at (a) probe 1 and (b) probe 2

.

Due to the interaction of the two combustors, pressure oscillations also appeared in the cross-talk, and the temporal results of the pressure oscillation are presented in Fig. 4.10a, while the FFT results are presented in Fig. 4.10b. A high initial CH_4 fraction was set for proper ignition in the simulation, and consequently, strong pressure oscillations occurred at the beginning of the simulation. The generated pressure perturbation dissipated over time; however, the dissipation stopped at a specific point due to thermoacoustic coupling and the creation of a limit cycle. In each combustor, thermoacoustic instability was generated in a similar phase and magnitude, and overlapping of these instabilities resulted in the generation of high-amplitude pressure oscillation in the cross-talk. The same phenomenon occurred in the experimental results, which confirmed the similarity with the numerical results. In the experiment [12], distinct instability was not shown except in f ≈ 200 Hz. The simulation results in Fig. 4.9 and Fig. 4.10 showed more instability magnitude in the high frequency beyond 200 Hz. The simulation considered less time period than the experiment due to computational cost. Therefore, oscillation magnitudes in high harmonic modes shown in the early stage of the simulation were overpredicted in the simulation.

(a)
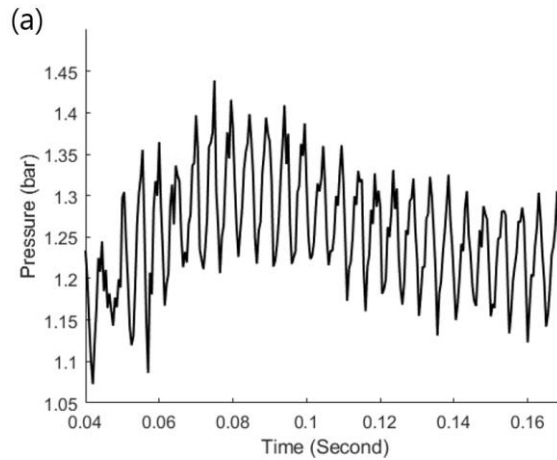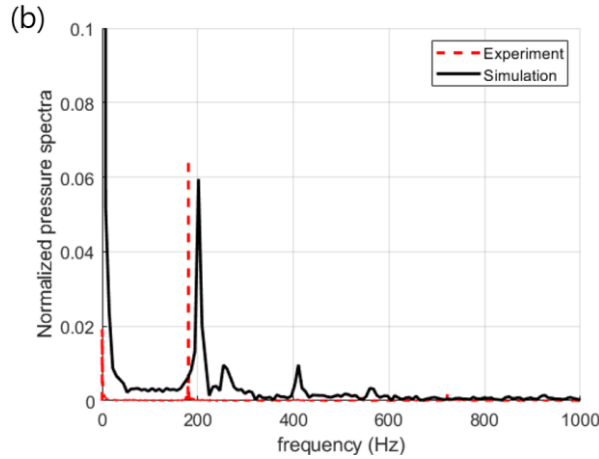
Fig. 4.10. (a) Temporal profile of pressure oscillation in the cross-talk and (b) the fast Fourier transform profile (black line) at probe 3 with a comparison to the experiment (red dashed line).

Figure 4.11 presents the time history of the heat release and pressure inside combustor 1 measured in the flame generation region. P' in Fig. 4.11 was obtained from probe 1, and Q' in Fig. 4.11 was obtained by integrating the heat release rates calculated at the nodes inside the combustor. The results demonstrate that the frequencies of the pressure and heat release oscillation were indeed in phase. Therefore, the Rayleigh criterion was satisfied, and thermoacoustic instability developed. The amplitude of the pressure oscillation illustrated in the results was approximately 4.2 kPa, which was slightly lower than the experimental results [12].
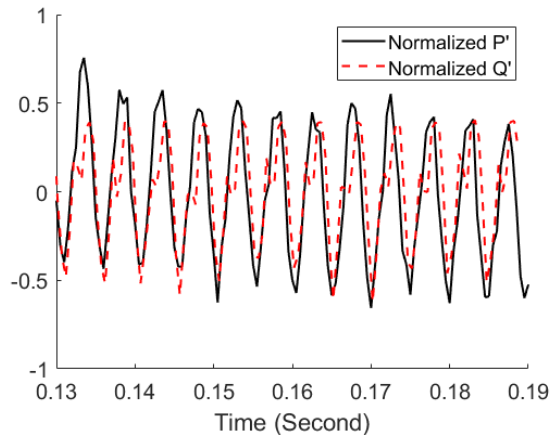
Fig. 4.11. Time history of normalized pressure and heat release
oscillations at probe 1.

The two pressure histories displayed in Fig. 4.12 represent the results measured in each combustor and reveal that symmetrical pressure oscillation appeared in the combustors. This in-phase interaction between pressure and heat occurred similarly in the cross-talk and the two combustors and displayed characteristics of the push-push mode, in which oscillations in the combustors vibrate in the same phase.
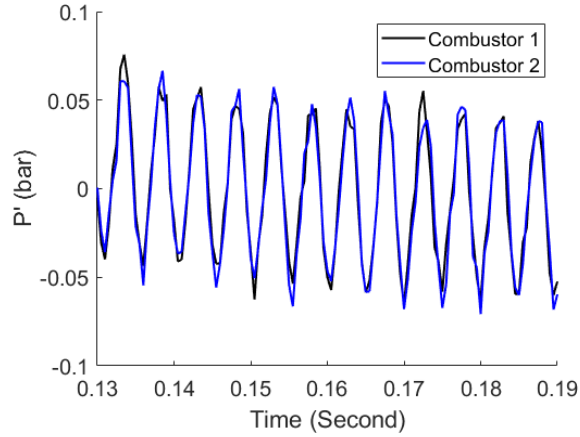
Fig. 4.12. Time history of acoustic pressure measured at probes 1
and 2.

The contour for this pressure perturbation is presented in Fig. 4.13 at every phase angle of 90° in a single cycle of 360°. Almost identical pressure field was formed in the two combustors where the pressure perturbation corresponding to push-push mode has occurred. Due to the flame generated at the inlet of the combustor, a slightly higher pressure than that in the surrounding area appeared in the combustor inlet region. In the middle of the injector, pressure discontinuity occurred due to the sharply bent swirler geometry. The pressure wave generated in each combustor was transported to the cross-talk, resulting in strong perturbations. Some of the pressure wave was dissipated into the combustor exit,

while most of it was reflected under the influence of the piston. All plotted figures are presented in the limit-cycle region, where constant pressure perturbation was maintained.
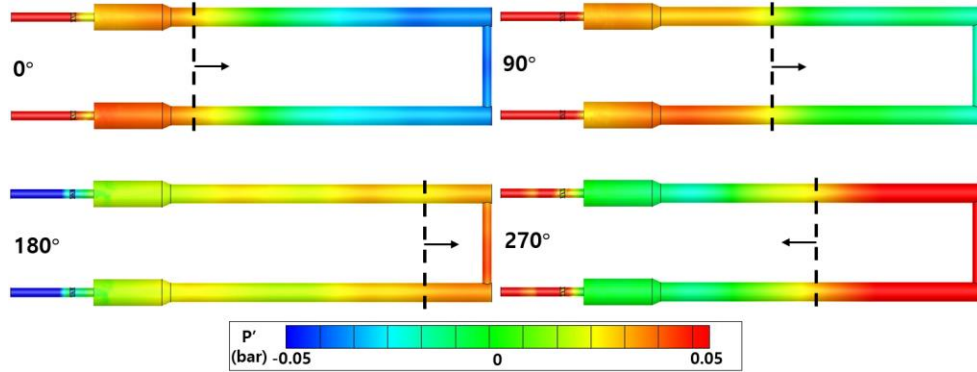
Fig. 4.13. Pressure oscillations shown in four different phases angle in the direction of the pressure wave.

The fluctuation of the flow rate resulted in a fluctuating flame. The injection speed at the inlet of the combustor is plotted in Fig. 4.14, and the flame isocontour is plotted in Fig. 4.15 based on the H mass fraction of 5×10^{-5}. The velocity profile and heat release rate in Fig. 4.14 was averaged in the transverse plane (including probes 1 and 2) located at the combustor entrance. The pressure measured at the center of the plane is plotted together with the heat profile in Fig. 4.14b. The flame was ignited at the inlet of the combustor (0°) and lifted into the axial direction (90°) as the premixed mixture was injected. As the injection flow rate increased, the flame developed (180°), forming an attached flame at the inlet of the combustor. In the subsequent phase (270°), as the injection flow rate decreased and backflow was formed, the flame structure collapsed and some of the flames were sucked into the injector. Finally, as the backflow stopped and the injection started again, the mixture was fed back into the combustor, and the cycle repeated (0°). These results qualitatively explain the effect of pressure waves in the combustion system on the injection flow and flame structure. Fig. 4.14b shows the change of the locally measured heat release rate and pressure depending on the flame enhancement and

extinction in Fig. 4.15. The heat showed local maxima between $90°$ and $180°$, when the flame was continuously developing through the combustor axial direction. Unlike the total heat release rate integrated with the entire combustor domain (Fig. 4.11), the local heat release rate showed a double peak in one cycle, which is similar to the velocity graph in Fig. 4.14a. It shows that the dynamics of flame were directly influenced by the supplying flow inside the injector. The measured pressure in Fig. 4.14b represents a similar phase to releasing heat, which shows the acoustic－combustion interaction in the flame zone, satisfying Rayleigh's criterion.
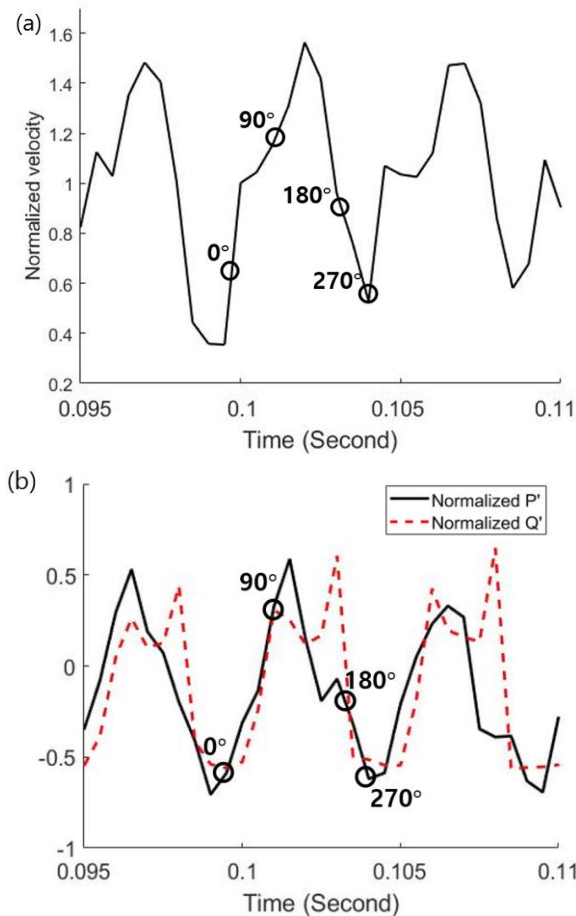

Fig. 4.14. Injection velocity profile normalized with (a) mean inlet velocity and (b) local pressure and heat release rate at the combustor entrance.
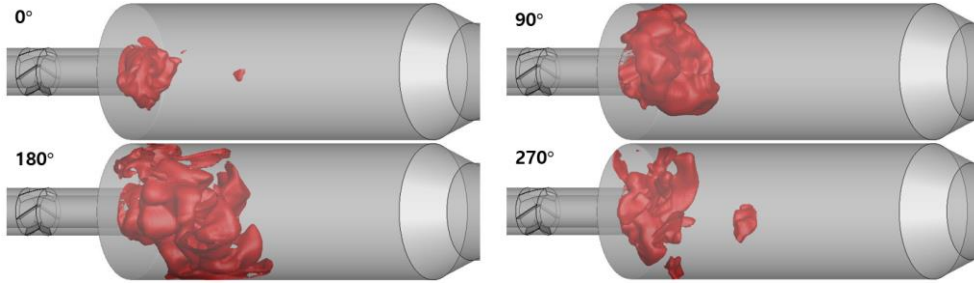
Fig. 4.15. Isocontour of oscillating flame in four different phases for the H mass fraction of 5×10^{-5}

A scatter plot of the heat release rate versus the progress variable (C) was generated for the quantitative analysis of the swirling flames in the combustors. The progress variable is a marker for reaction zones in combustion and has the value of unity or zero except in flamelets. The formula for the progress variable is shown in the following equation:

$$C = \frac{Y_{O_2} - Y_{O_2}^u}{Y_{O_2}^b - Y_{O_2}^u} \tag{5}$$

where Y_{O_2} indicates the mass fraction of the oxidant (oxygen) in the computational domain $Y_{O_2}^b$ and $Y_{O_2}^u$ are the oxidant mass fraction of the unburned and burned mixture, respectively. For the scatter plot, averaging of 20 transient profiles corresponding to each phase was performed. The flame oscillation was generated by the pressure wave response, and the scatter profile in the combustor for the oscillating flame in four different phases was plotted, as illustrated in Fig. 4.16. Samples of the progress variable and heat release rate were measured in the quartz combustor region. The bent shape and resulting vortices near the combustor entrance generated the high kinetic energy and low Damkohler number region, causing intense mixing with burned gas in the quartz combustor region. Local flame extinction due to periodic flame stretch and incomplete burning also occurred in the combustors. Therefore, a broad distribution of the heat release rate, especially

in the intense reaction zone, was observed in each transient profile.

Figure 4.16 presents the scatter results for the phase 0°, in which the flame was sucked into the injector. In this phase, most of the reactions were not proceeded, and only hot burned gas was located in the combustor. Accordingly, most of the samples were located near C = 1, and therefore, a relatively low heat release rate is illustrated in the graph. The scatter plot results for the fully developed flame phase (180°) measured in the combustor are also presented in Fig. 4.16. Under the influence of turbulence, a broadly scattered distribution appeared in the reaction region of C = 0.4 ~ 0.8. The peak heat release rate was formed at approximately C = 0.7, and a rapid decrease in the heat release value occurred after the peak value. Comparison with the results derived from the freely propagating laminar flame was performed. The profile of the laminar flame was calculated using Cantera [28] under the same inlet temperature and chamber pressure conditions as in the simulation. The characteristics of the laminar flame were in good quantitative agreement with the scatter profile results from the fully stretched flame, indicating that the swirling stretched flame in the simulation exhibited similar characteristics to the propagating flame.

The scatter plots of the injection and dissipation flames correspond to phases 90° and 270°, respectively. In each phase, the progress variable ranged from 0 to 1, indicating that most of the reactions occurred in the combustor. In the injection flame, the heat release rate was distributed more widely than in other phases, which was attributed to the turbulence caused by the fast injection speed. In the absorption flame, a narrower scatter distribution was identified due to the slowed injection speed, and a low heat release rate was observed.

0°

90°

180°
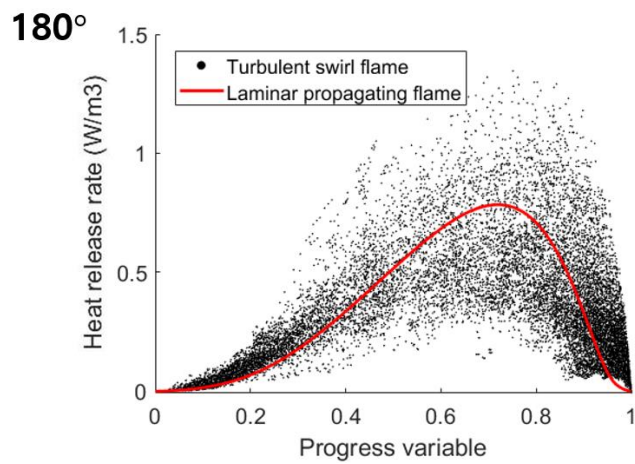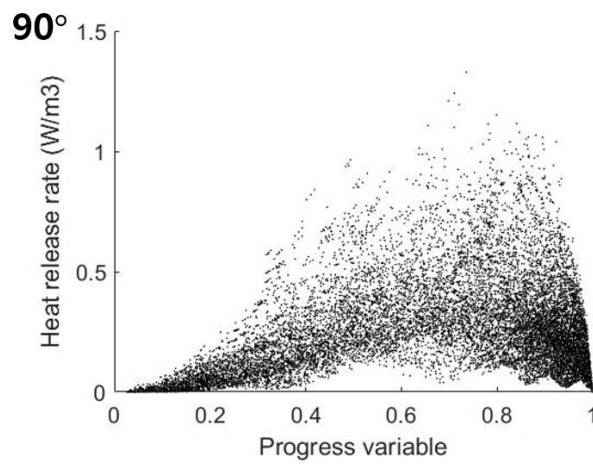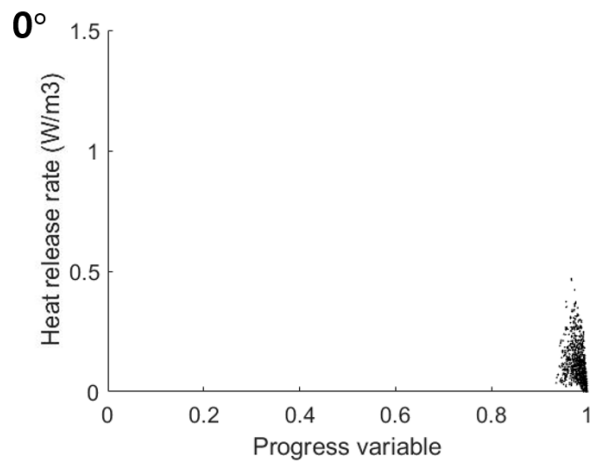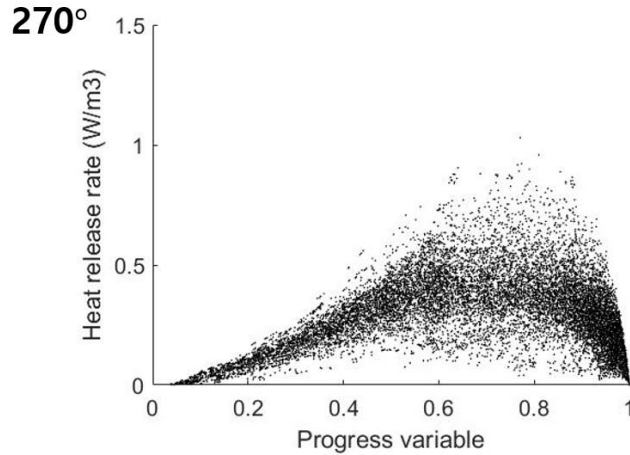
Fig. 4.16. Scatter plots of the heat release rate, plotted in four different phases where the results for fully stretched flame (180°) is superimposed on those for laminar propagating flame.

4.3.3. Case 3: Single combustor without the cross-talk in closed condition

Additional test considered a single combustor with closed condition shown in Fig. 4.2b. Comparison with Case 2 is made for understanding the role of the cross-talk in the generation of thermoacoustic instability. In the single combustor, the thermoacoustic instability was also observed. Figure 4.17 depicts the pressure spectra of combustion instability where the comparison was made between the single and dual combustors with the cross-talk. While the instability frequencies corresponding to the fundamental axial mode of combustor were the same for both experiment and simulation, a difference in the magnitude of the instability is observed in Fig. 4.17b. The increase in the amplitude in the single case is due to the disappearance of radial oscillations apparent in the dual case with the cross-talk. Also, the decrease in the total combustor area is also responsible for the increase in the amplitude. In other words, because the heat release rate due to combustion was the same, it is presumed that the oscillation in the cross-talk, and large area effectively dissipated the acoustic energy in the two combustors. Therefore, the interactions through the cross-talk in Case 2 had effectively worked towards restraining

the instability of combustion system.
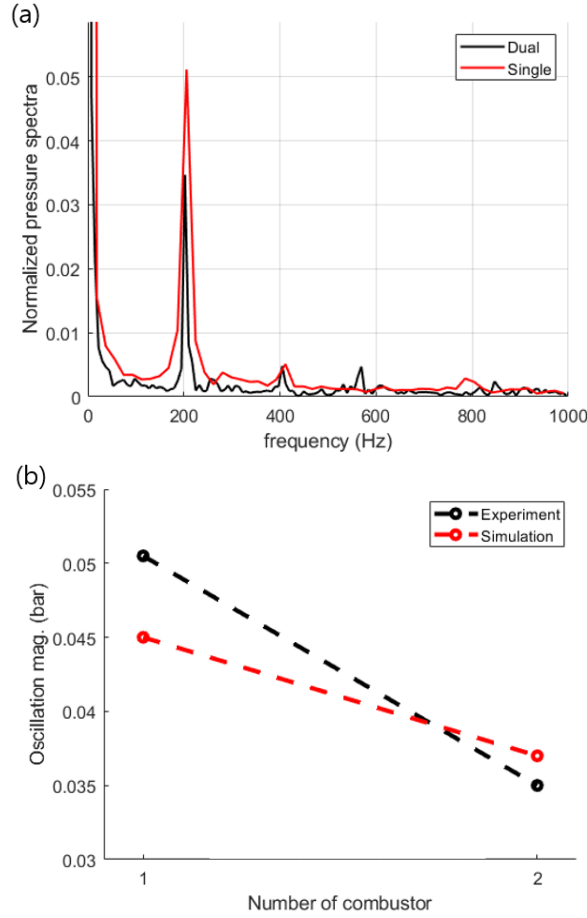
Fig. 4.17. (a) Fast Fourier transform results of pressure oscillation inside a single combustor (probe 4, red line) in Case 1 and dual combustors with cross-talk area (probe 1, black line) in Case 2 and (b) comparison with experimental results.

4.3.4. Case 4: The asymmetry issue related to the cross-talk existance

The forced asymmetry in a dual combustor arrangement of Case 2 is subsequently considered. In the previous experiment [12], asymmetry was enforced by allowing the equivalence ratio to vary in each combustor. The difference of flame dynamics and product gas temperature in combustors resulted in asymmetry in the experiment. That asymmetry of combustion dynamics induces the

out-of-phase interactions of each combustor (push-pull mode) and attenuates the instability magnitude compared with the symmetrical cases. Similar experimental work [29] was performed with varying swirler geometry in two combustors. Five different swirlers were considered, and accordingly, different flame transfer functions (FTF) were created in each combustor. The results were in agreement with the work of [12] indicating the asymmetry of the swirlers induced instability attenuation and out-of-phase interactions in combustion system. For the purpose of comparing the previous experiments, the effect of asymmetry in combustion instability was revisited via the simulation. Here, a velocity pulsation to suppress the instability is imposed on one combustor inlet while keeping the inlet equivalence ratios the same in both combustors. Therefore, the constant heat input and geometry are considered, and the asymmetrical acoustic velocity leads to the change in the combustion instability. The phase of the inlet pulsation was set opposite to the phase of the self-excited instability generated inside the combustor. The pulsation was given at the left end of a computational domain of combustor 2 (Fig. 4.1). By applying inlet pulsation, instability attenuation of combustor 2 and its out-of-phase interaction with combustor 1 are intended. Table 4.2 shows the frequency and amplitude of the inlet pulsation which is imposed only in combustor 2. The simulation is intended to monitor the instability suppression and combustor-combustor interactions resulting from an additional inlet pulsation at the combustor entrance.

Table 4.2. Inlet pulsation conditions.

Case	1	2
Combustor number	Open	Closed
Velocity magnitude (m/s)	1	2
Pulsation frequency (Hz)	0.65	0.65
Pulsation amplitude ($U'/\overline{U}$)	50	40

Figure 4.18 reports the spectra of the pressure as computed. Due to inlet pulsation effects, the suppression of instabilities is observed. In combustor-2 with an inlet pulsation, the strength of instability was noticeably reduced (Fig. 4.18a) while the oscillation frequencies were conserved in both combustors. Moreover, the velocity pulsation resulted in almost one-third reduction in oscillation amplitude at the frequency of f = 200 Hz, which indicates that external flow pulsation can result in an oscillation beating in combustors. The transition to high frequencies appears at around f ≈ 900 Hz, which corresponds to the 4th longitudinal mode of the combustor. Such transition of instability was caused by the interference of velocity perturbations inside the injector. Changes in combustor-2 affected combustor-1 through the cross-talk. The oscillation magnitude was dissipated at the frequency of f = 200 Hz (Fig. 4.18b), but not as much as that of combustor-1 (Fig. 4.18a). The high-frequency oscillation in combustor-2 also affects combustor-1 since the pressure wave from the oscillating flame propagates through the cross-talk.
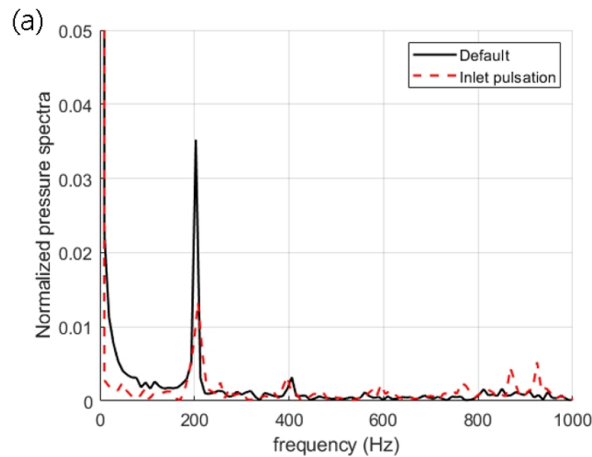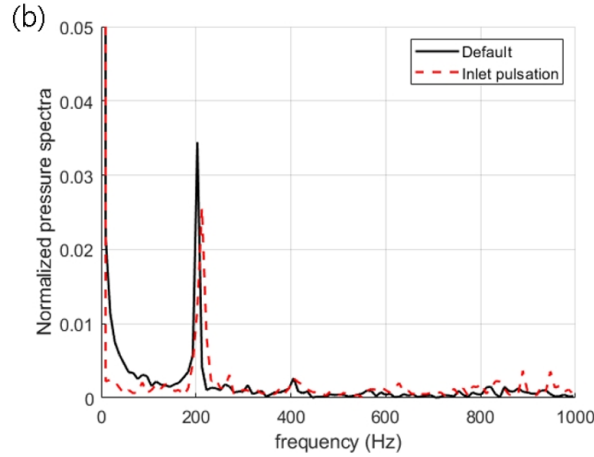
Fig. 4.18. FFT of the pressure without (solid line) and with (dashed line) inlet pulsation obtained from (a) probe 2 and (b) probe 1.

FFT result of the oscillating pressure at the cross-talk is described in Fig. 4.19. The attenuation of oscillation also appeared at the frequency of 200 Hz, similar with the results shown in Fig. 4.18. The oscillation peaks were also shown at 400 Hz and 800 Hz, due to the transition from a fundamental to higher harmonic modes. The mode change did not appear in the system since the different phase of pulsation is fully dissipated at the end of the combustor. Thus, the combustion system remains in a push-push mode.
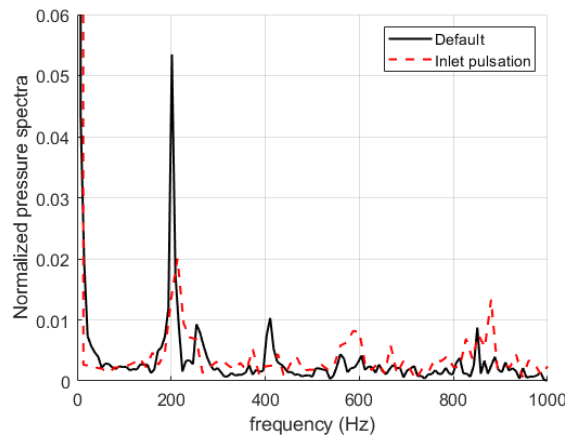
Fig. 4.19. FFT of the pressure at the cross-talk (probe 4) without (solid line) and with (dashed line) inlet pulsation.

Under the asymmetric condition as considered thus far, the three-dimensional flow fields are illustrated in Fig. 4.20. The inlet pulsation reduced the oscillation in the injector. After passing through the swirler, the flow perturbation was amplified and accelerated in both combustors due to the acoustic wave effect. Also, the ratio of oscillation is observed to be weaker due to the instability suppression effect. The supplied gas highly rotated in both combustors just before the injection. In the region past the injection, the flow propagated into the axial direction and swirled through the wall region. In the combustor compression region, flow continuously rotated and moved through the axial direction. Some flow moved through the cross-talk and transported to the neighboring combustor. The velocity distribution in the cross-talk is relatively slow except at the edge region.
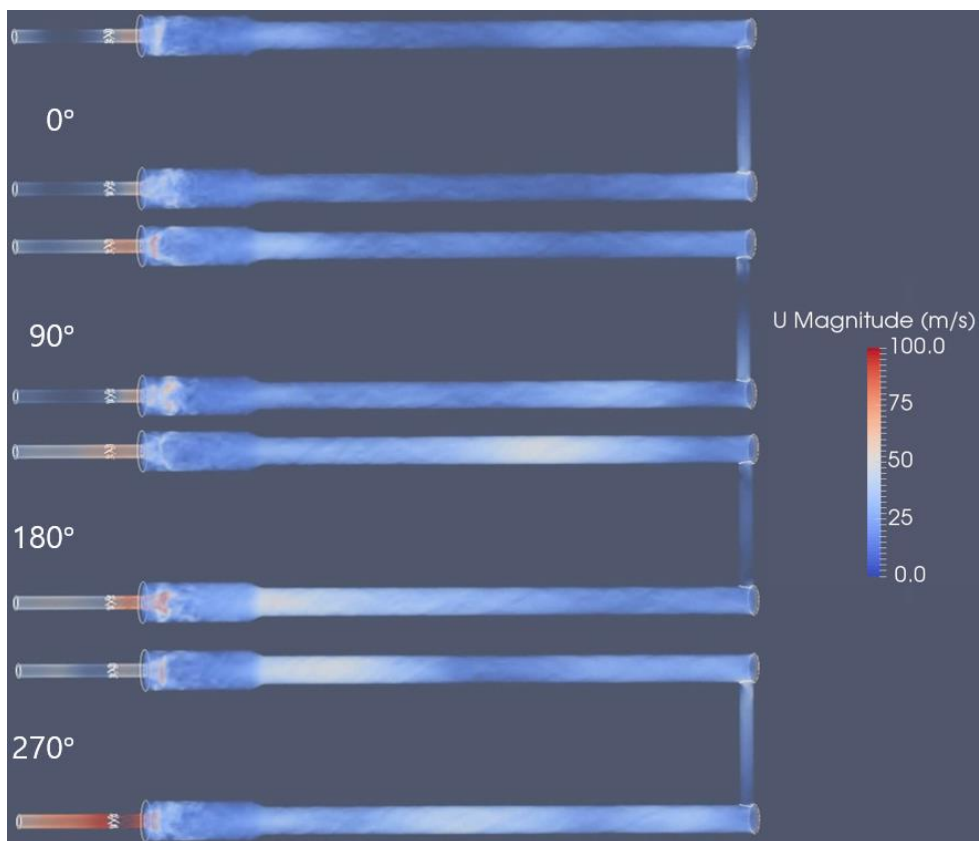
Fig. 4.20. Transient fields of velocity magnitude in four different phases.

The enlarged view of the transient velocity with pulsation (Fig. 4.21a) and without pulsation (Fig. 4.21b) are described. With the inlet pulsation, the injecting flow propagated shorter in the axial direction (180°), resulting in a more stable flow structure. The oscillation at the combustor converging section was also reduced with the inlet pulsation. Such suppression of heat oscillation has led to the dissipation of combustion instability. Thus, the velocity pulsation in one combustor inlet suppressed the thermoacoustic instability by interfering with internal velocity oscillations as shown from the present numerical simulation. Therefore, the asymmetry velocity oscillation induced by an external acoustic source, which is possibly given by asymmetrical injector or swirler design in each combustor, or additional acoustic damper [30], can be considered at the design stage of gas turbine combustors for the attenuation of combustion instability.
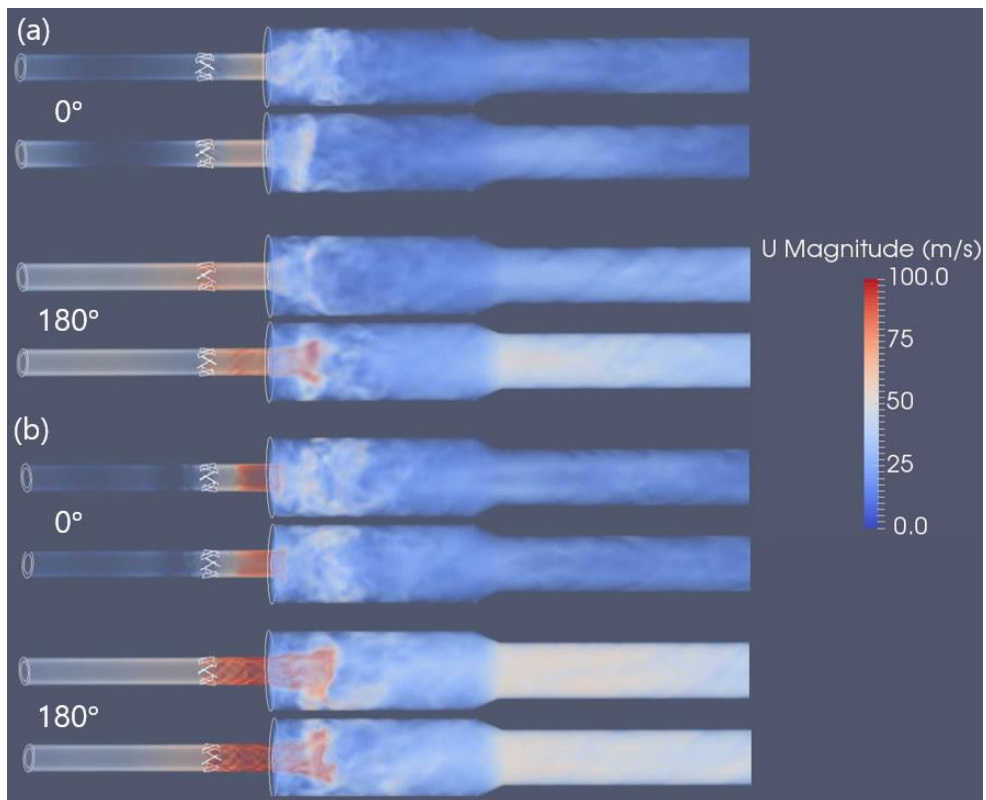
Fig. 4.21. A comparison of inlet pulsation effect: magnified transient fields of velocity magnitude for (a) with and (b) without the inlet pulsation.

4.4. Conclusions

A numerical simulation was performed for two combustors connected via the cross-talk. LES with a PaSR model was used to simulate the swirl-stabilized premixed flames in the combustion chamber. The results on the open combustor case were compared with the experimental CH*-chemiluminescence results, indicating a good agreement. The can-annular type combustion system consists of the two combustors with the cross-talk was considered and the thermoacoustic instability inside it was simulated, which has never been done in the past. where the combustion instabilities with the push-push mode are self-excited. An attached flame was observed in each combustor as well as high mixing rate and vigorous burning in the recirculation area near the wall. The simulation on the closed combustor without the cross-talk is subsequently considered, showing the reinforcement of combustion instability due to the absence of the cross-talk. Changes in the thermo-acoustic instability and flow fields due to the asymmetric inlet perturbation were also discussed. The external inlet pulsation on one of the two combustors resulted in a noticeable attenuation of combustion instabilities in both combustors, suggesting an efficient method of suppressing combustion instabilities in a can-annular combustion system. This study showed the applicability of the LES model in a chemically reactive multi-combustor system in an attempt to clarify the unfamiliar role of the cross-talk and to advance the design of a can-annular combustor. Moreover, the present effort broadened the applicability of the pressure-based LES solver for performing the thermoacoustic instability analysis.

Chapter 5. Dual-mode scramjet combustor with disturbance: reduced order analysis

5.1. Background and objective

The research and flight tests of supersonic propulsion systems have been conducted for decades to develop stable and reliable hypersonic vehicles. Previously, numerous computational studies were performed to analyze supersonic combustion using high-fidelity CFD solvers, especially for scramjet combustors. That numerical analysis requires the modeling of turbulent combustion in a fully compressible flow, and research conducted in Sweden [1-3] reported high-accuracy results compared with the experiments. Still, high-fidelity simulation in supersonic combustion requires a very large number of grids far exceeding one million, and high computational costs. Therefore, CFDs may be inappropriate to use in the design and trajectory optimization stage of the hypersonic vehicle which requires various numbers of thrust and mode information.

In this regard, the reduced order models within the one-dimensional environment have been studied considering mixing and combustion phenomena inside the scramjet combustor. Previously, the quasi-one-dimensional governing equations consisting of the continuity, momentum, energy, and species conservation equation were proposed by O'Brian *et al.* [4] in the differential form. Finite-rate chemistry model for the hydrocarbon-burning scramjet engine was implemented in the solver, and the solver was used for rapid design and optimization of the vehicle. The research performed by Torrez *et al.* [5] proposed the combustor model for the subsonic and transonic combustor conditions, considering the ram-to-scram transition and thermal choking phenomena. The reported results confirmed good accuracy with the experimental results and a thrust map was proposed depending on flight number

and altitude. Also, Birzer and Doolan [6] derived a supersonic mixing model in the hydrogen-fueled scramjet combustor, and the calculated mixing efficiency was implemented in the one-dimensional solver.

Based on the previous studies of the combustion analysis on a hypersonic vehicle, we developed a simulation module for designing and optimization of the propulsion system which is in development. The developed solver considered the instabilities including pseudo-shocks in the isolator and thermal choking in the combustor. The flight conditions consisting of altitude, Mach number, and angle of attack (AOA) are set as the inputs in a solver and are given as variables in the simulation.

5.2. Mathematical modeling

The one-dimensional compressible governing equations in the differential form were considered for the chemically reacting flow including equations of continuity (Eq. 1), momentum (Eq. 2), equation of state (Eq. 3), molecular weight (Eq. 4), added mass in the combustor (Eq. 5), energy (Eq. 6), species transport (Eq. 7), and progress rate of species (Eq. 8):

$$\frac{1}{\rho}\frac{d\rho}{dx} = \frac{1}{\dot{m}}\frac{d\dot{m}}{dx} - \frac{1}{U}\frac{dU}{dx} - \frac{1}{A}\frac{dA}{dx} \tag{1}$$

$$\frac{1}{U}\frac{dU}{dx} = \frac{-1}{\gamma M^2}\left(\frac{1}{p}\frac{dp}{dx} + \frac{2\gamma M^2 C_f}{D} + \frac{\gamma M^2(1-\varepsilon)}{\dot{m}}\frac{d\dot{m}}{dx}\right) \tag{2}$$

$$\frac{1}{P}\frac{dP}{dx} = \frac{1}{\rho}\frac{d\rho}{dx} + \frac{1}{T}\frac{dT}{dx} - \frac{1}{\overline{MW}}\frac{d\overline{MW}}{dx} \tag{3}$$

$$\frac{d\overline{MW}}{dx} = -\overline{MW}^2 \sum_i \frac{1}{MW}\frac{dY_i}{dx} \tag{4}$$

$$\frac{d\dot{m}}{dx} = \sum_i \left(\frac{d\dot{m}_{i,added}}{dx}\right) \tag{5}$$

$$\frac{dT}{dx} = \frac{1}{c_p}[-\sum_i (h_i \frac{dY_i}{dx}) + \frac{1}{\dot{m}} \sum_i (h_i \frac{dm_{i,added}}{dx})$$

$$- \frac{h_0}{\dot{m}} \frac{d\dot{m}}{dx} - \frac{2C_f c_p (T_{aw} - T_w)}{\mathrm{Pr}^{2/3} A} - U \frac{dU}{dx}] \tag{6}$$

$$\frac{dY_i}{dx} = \frac{\dot{\omega}_i MW_i A}{\dot{m}} + \frac{1}{\dot{m}} \frac{d\dot{m}_{i,added}}{dx} - \frac{Y_i}{\dot{m}} \frac{d\dot{m}}{dx} \tag{7}$$

$$\dot{\omega}_i = \frac{dC_{Q_i}}{dt} = \sum_j k_{f,j} (v_{ij}'' - v_{ij}') \prod_i C_i^{v_{ij}'} \tag{8}$$

In above equations (1-8), T is the temperature, P is pressure, ρ is density, v is velocity, $\dot{m}$ is mass flow rate, $\overline{MW}$ is the molecular weight of the mixture, Y_i is species mass fraction, $\dot{\omega}_i$ is the production rate of the species, C_f is wall friction coefficient, ε is fuel jet orientation factor, T_{aw} is adiabatic wall temperature, h_0 is stagnation enthalpy, Pr is Prandtl number, respectively.

The governing equations were implemented in the Python code and were solved using the built-in 5th-order implicit Runge-Kutta solver [7]. 30-step reaction mechanism of hydrogen [8] consists of 11 species was used for the combustion of injecting fuels, and therefore, was introduced in the solving processes of equations (7) and (8).

The combustion reaction rate highly depends on the initial conditions of inlet flows, which were determined from the flight conditions. The combustion process should be within the predictable range for the stable flight of the hypersonic vehicle. Therefore, algorithms that can identify the mode of the propulsion system should be specified in advance. In the dual-mode scramjet engine, scramjet mode and ramjet mode combustion exist, where ramjet mode indicates the flow enters the combustor with a subsonic speed and scramjet mode indicates the flow enters the combustor with a supersonic speed. The increase of the fuel flow rate into the combustor causes the Mach number to reach unity, resulting in thermal choking and ram-to-scram transition. In the ramjet mode

combustion, the pre-combustion shock train (PCST) generates in the isolator, which affects the combustor inlet flow. Therefore, in the ramjet mode combustion, interactions between the isolator and combustor should be considered. The PCST is not captured and must be assumed in the one-dimensional solver, the psudo-shock model proposed by Ikui $et\ al.$ [9] was used in the isolator part. In the psudo-shock model, the flow velocity and pressure at the combustor outlet was calculated based on the relations using Crocco's number w_i:

$$w_i = \frac{u_i}{\sqrt{2C_p T_t}} \quad (i=1,2) \tag{9}$$

$$w^* = \frac{\sqrt{\gamma-1}}{\sqrt{\gamma+1}} \tag{10}$$

$$w_1 w_2 = w^{*2} \tag{11}$$

$$\frac{p_2}{p_1} = \frac{w_1^2/w^{*2} - w^{*2}}{1 - w_1^2} \tag{12}$$

where w_i is Crocco's number at the inlet (i=1) and outlet (i=2) of the isolator, u_i is flow speed, T_t is total temperature, P is pressure, γ is ratio of specific heat, C_p is specific heat capacity.

The schematic of the implemented algorithm in a current work module is shown in Fig. 5.1.


9 3
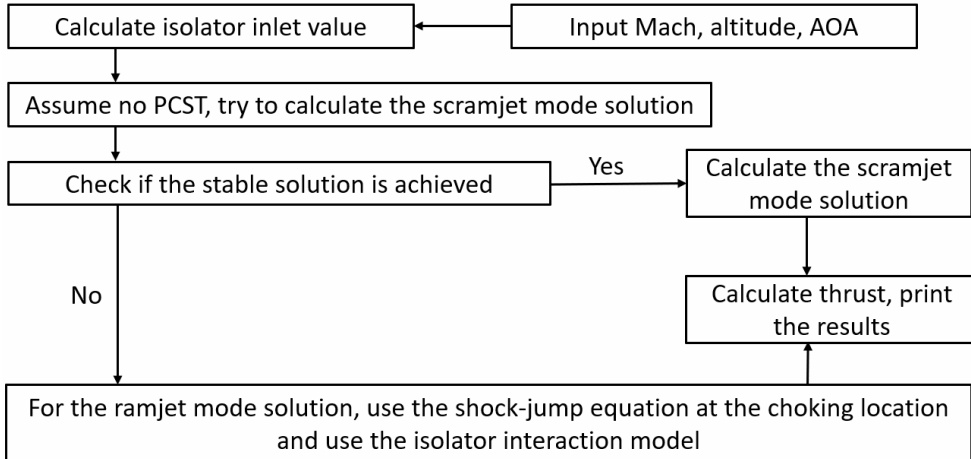
Fig. 5.1. Algorithm in the simulation module.

When the Mach number in the combustor goes below unity, the stable supersonic solution is not achieved in the combustor. Therefore, ramjet mode combustion is shown in the combustor and prediction of the thermal choking location is required. In this work, a shooting method proposed in the previous research [5] to find transonic solution and thermal choking location. Mach number equation and forcing function in Eqs. (13−16) proposed by Shapiro [10] were used for the prediction of thermal choking location.

$$\frac{1}{M^2}\frac{dM^2}{dx} = -\frac{2\{1+[(\gamma-1)2]M^2\}}{1-M^2}\frac{1}{A}\frac{dA}{dx}$$
$$+\frac{(1+\gamma M^2)\{1+[(\gamma-1)2]M^2\}}{1-M^2}\frac{1}{T_0}\frac{dT_0}{dx}$$

(13)

$$\frac{1}{M^2}\frac{dM^2}{dx} = \frac{G(x)}{1-M^2}$$

(14)

$$\frac{M^3}{(M-1)^2}\frac{d(M-1)^2}{dx} = \frac{-G(x)}{(M-1)^2(M+1)}$$

(15)

$$G(x) = (1-\frac{\rho u^2}{\gamma p})(\frac{2}{u}\frac{du}{dx}+\frac{1}{\rho}\frac{d\rho}{dx}-\frac{1}{p}\frac{dp}{dx})$$

(16)

where M is Mach number of the flow, G is forcing function, and T_0 is stagnation temperature. Values from the governing equations of Eqs. (1−3) were used to compute the forcing function. From the Eq. (15), which is derived from Eq. (14), it is shown that positive value of G forces the Mach number toward unity and negative value of G forces the Mach number away from unity. Therefore, at the sonic point, G must move from positive to negative and has the value of zero.

The equations and algorithms in the simulation module were applied for the simulation of the dual−mode scramjet engine, which design is in progress (Fig. 5.2).
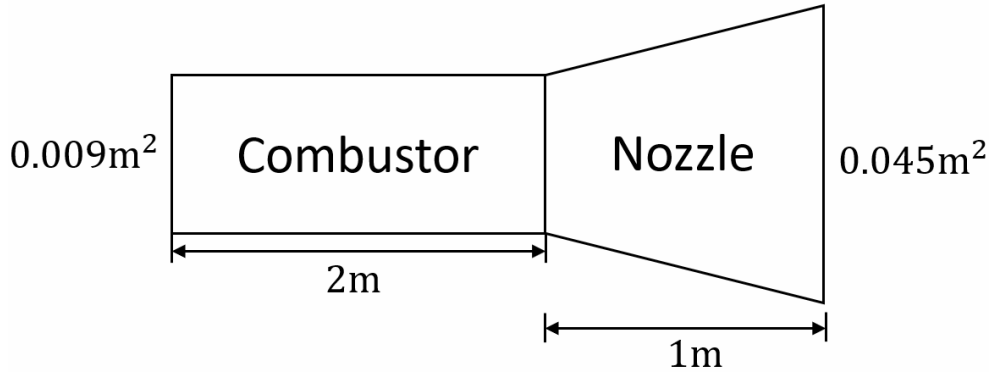
Fig. 5.2. Schematic of a computational domain

5.3. Results and discussions

The developed solver was validated to compare the calculated ignition delay with the previous work [8]. In the reference [8], the calculation using the same combustion model predicted the measured ignition times of chemical mixtures. The ignition time is defined as the time at which the concentration of CO_2 exceeds certain values, as shown in Fig. 5.3a. The calculated ignition delay times in the current solver were compared with reference data, as shown in Fig. 5.3b.
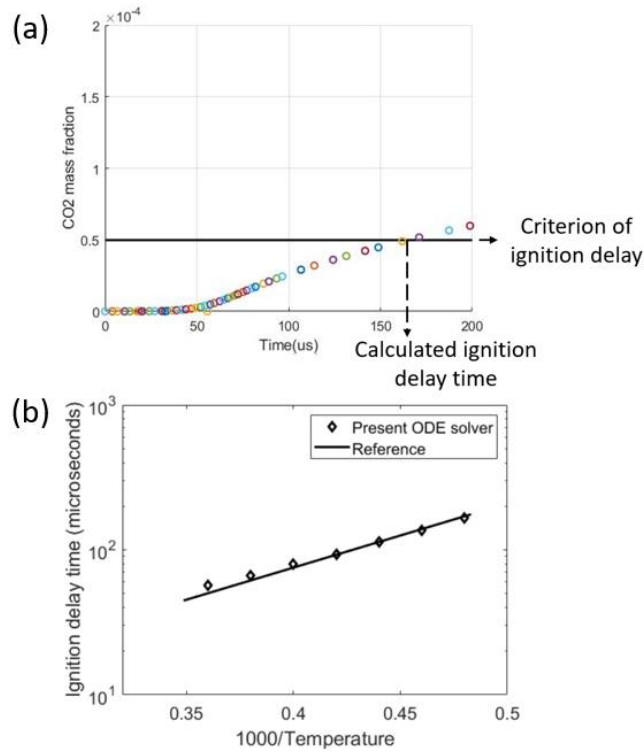
Fig. 5.3. (a) The concentration of CO_2 representing ignition delay and (b) ignition delay profile for various initial temperature.

The results in Fig. 5.3b show decrease of ignition delay time with increase of initial temperature. Profiles in log-scale are in good agreement with the reference data, which shows the reliability of the current combustion solver.

One-dimensional simulations were subsequently carried out to obtain information of thrust, combustion mode, and thermal choking location. Flight conditions for the simulations are shown in Table 5.1.

Table 5.1. Flight conditions applied in the simulation.

	Case 1	Case 2	Case 3
Flight altitude (km)	25	25	27
Mach number	6	6	6
Angle of attack (°)	0	6	8
Air flowrate (kg/s)	6.391	7.466	5.484

In Table 5.1, case 1 flight condition was arbitrary selected and case 1,2 flight conditions were calculated from the trajectory optimization model.
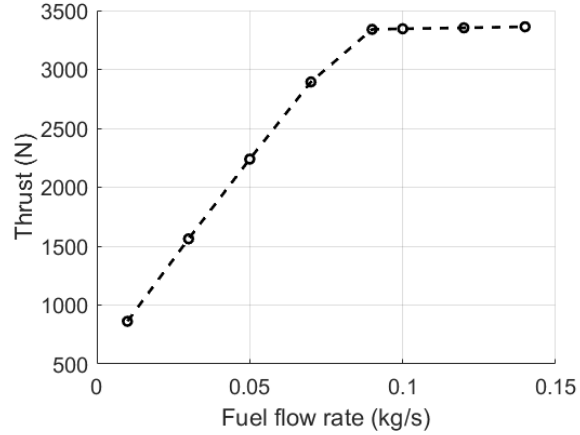
Fig. 5.4. The thrust profile in case 1 condition.

In case 1, the inlet air flow rate was calculated as 7.188 kg/s, which was set as the boundary condition in the combustor. Figure 5.4 shows the computed thrust with the change of equivalence ratio in case 1. The thrust continuously increased due to the increase in the supplying fuel and the equivalence ratio. The thrust has a maximum value near 3,400 N. It indicates that additional fuel beyond the equivalence ratio of 0.5 was not burned due to the high-speed flow in the combustor. Mode transition was not shown since the Mach number in the combustor did not go below unity.
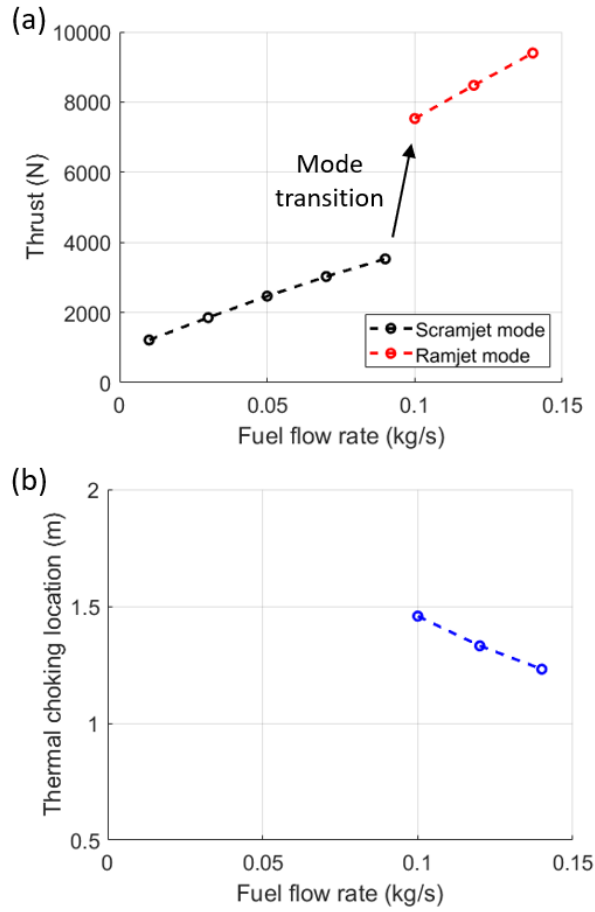
Fig. 5.5. The thrust and thermal choking location in case 2 condition.

In case 2, the inlet flow rate was changed to 7.466 kg/s due to the increase in AOA. Unlike case 1, ram-to-scram mode transition appeared at the fuel flow rate of 0.1 kg/s, which corresponds to an equivalence ratio of 0.46. Due to the transition, the thermal choking location was calculated at the sonic point. The thermal choking first appeared downstream of the combustor and continuously moves upstream due to the increased flow rate.
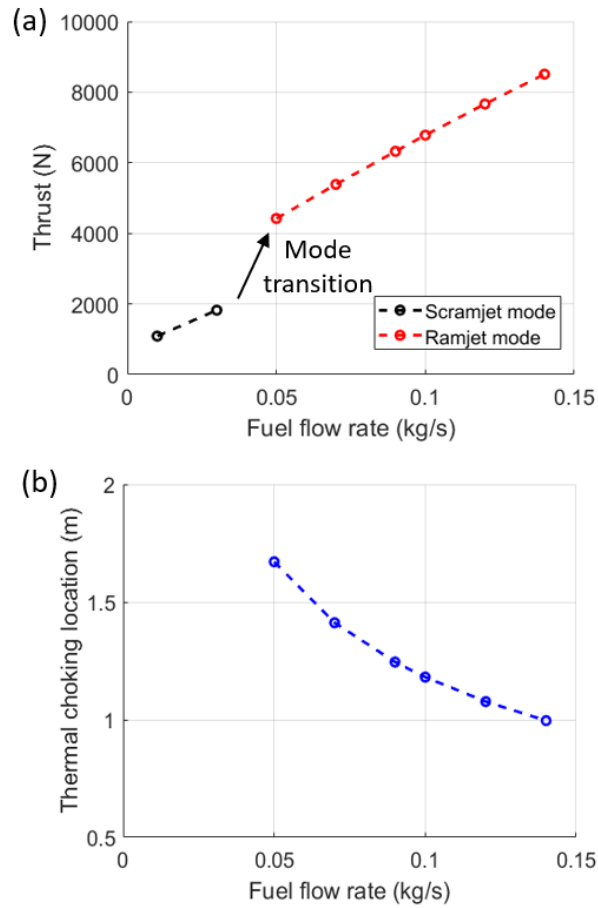
Fig. 5.6. The thrust and thermal choking location in case 3.

In case 3 with a higher altitude, the inlet flow rate was calculated as 5.484 kg/s. Mode transition appeared at a smaller fuel flow rate compared with case 2, due to the less air flow rate and combustor Mach number in case 3. After the mode transition, thrust increased to 9 kN as the increased of fuel flow rate, while the thermal choking location moved the combustor upstream.
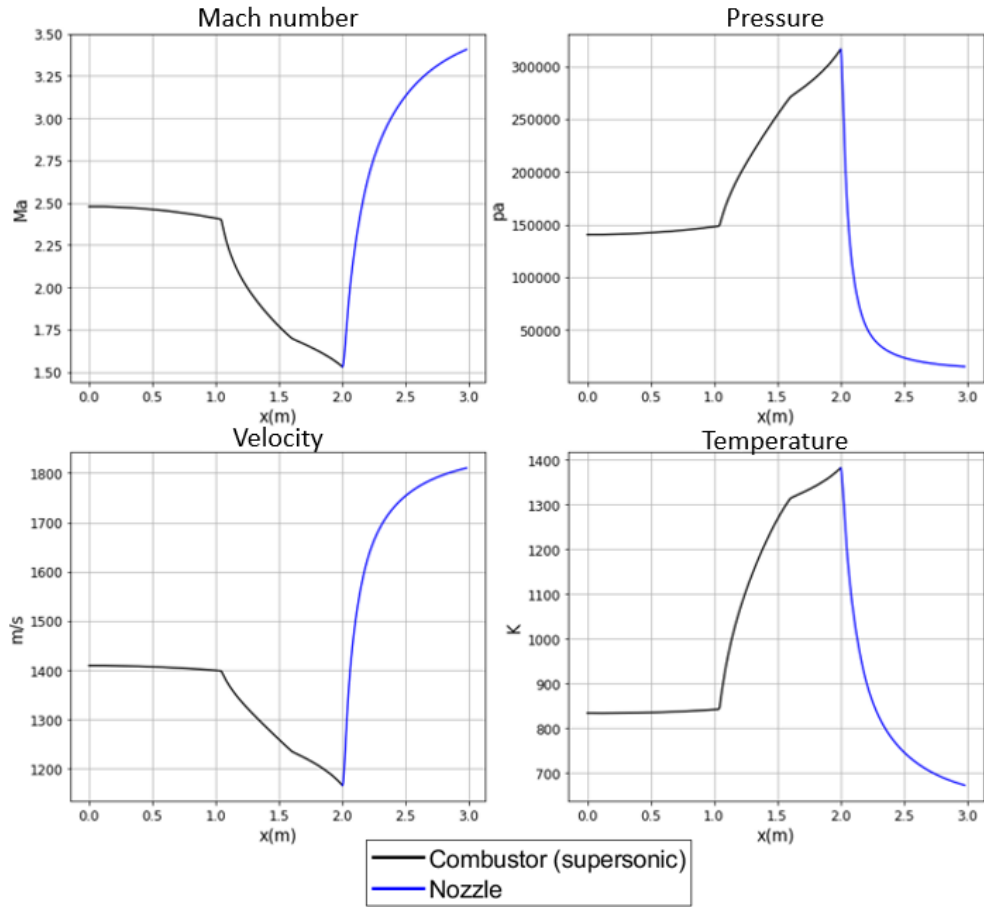
Fig. 5.7. Flow variables in the scramjet combustion mode.

Figure 5.7 shows the distribution of computed flow variables in a fuel mass flow rate 0.09kg/s in case 2. At the combustor entrance, the flow did not ignite due to the low temperature of the air flow. The high-temperature cavity region with 1400 K was assumed at the middle of the combustor, and therefore, combustion occurred at the corresponding region. The Mach number of the flow did not go below unity and the combustor was in scramjet mode. The flow conditions on the combustor outlet were set as inputs of the nozzle model, and the flow information in the nozzle was calculated as blue lines in Fig. 5.7.
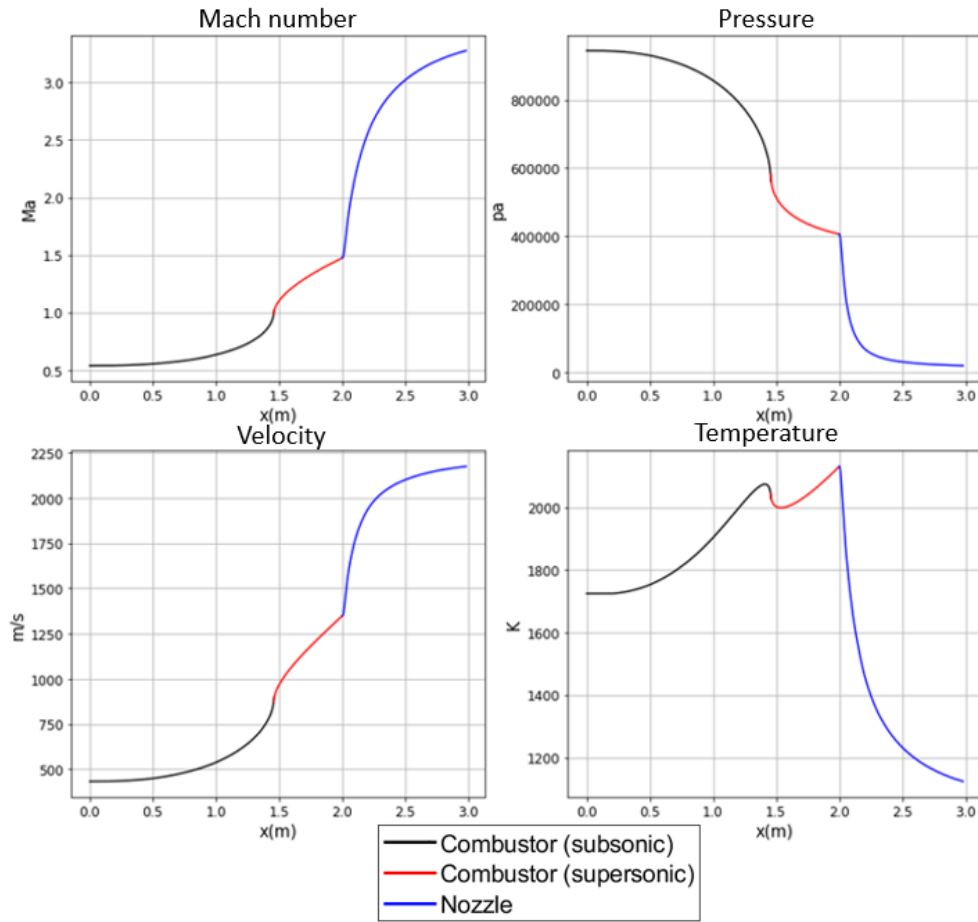
Fig. 5.8. Flow variables in the ramjet combustion mode.

The subsonic flow is shown at the combustor entrance in ramjet combustion mode of Fig. 5.8. The fuel flow rate in Fig. 5.8 was 0.1kg/s, similar to the fuel flow rate in Fig. 5.6. It indicates that small change in fuel condition results in the drastic change in the combustion process. Pressure and temperature at the combustor entrance were high due to the PCST in the isolator. Therefore, combustion immediately starts as the fuel supply began through the combustor. Thermal choking appeared at the 1.5m from the entrance satisfying M=1 and G=0 conditions simultaneously. After the choking, supersonic combustion appeared and continuously accelerated.

5.4. Conclusions

In this work, the reduced-order combustion solver is developed to simulate the dual-mode scramjet combustor. One-dimensional governing equations with the finite-rate chemistry model are implemented to solve high-speed reacting flow in the combustor. The solver is able to interpret the unstableness of combustion mode transition and thermal choking, which are formed due to intense combustion of injecting fuel and change of Mach number. Validation of the solver is done by calculating ignition delay in different temperature conditions. Flight conditions of the solver are calculated from the trajectory optimization model and the inlet boundary condition of the flow is calculated using the scramjet intake model. The simulation results show the increase of the thrust and occurrence of mode transition as the fuel flow rate increases. Thermal choking location is calculated downstream of the combustor and moves upstream as the fuel flow rate increases. The developed solver could contribute to the development of hypersonic vehicle in Korea, which is design in progress. The current solver is based on previous experiments and numerical models. Therefore, additional modeling based on experiments, especially on the mixing model, is required in future studies. Also, the validation of the mode-transition algorithm is left in future studies, which are planned using related experimental and CFD data.

Chapter 6. Conclusion

In this research, the main goal is to understand the causes of combustion instability by simulating unstable turbulent combustions with reliable accuracy. The role of fuel composition, mixing, flow speed, and geometry in triggering combustion instability is clarified through numerical simulation. In the simulation, the change of flame structure depending on hydrogen composition is confirmed. The short and intense swirl flame is simulated in high hydrogen composition due to fast flame speed and high diffusivity of hydrogen. The self-excited combustion instability is numerically captured in certain hydrogen composition, and it accompanies intense flame fluctuation. In this condition, the interaction of flame and vortices in the recirculation zone is investigated, which results in intense heat release fluctuation. The equivalence ratio fluctuation observed inside the fuel-air mixing area also results in heat release fluctuation of flames, which contributes to increasing heat release fluctuations. The fluctuation of the equivalence ratio is the same spectrum as combustion instability, showing linear interaction between the equivalence ratio and heat release fluctuations. FTF simulations excluding acoustics are subsequently performed, and the periodic formation of vortices in the fuel supply system is observed in the oscillation frequency of 50 Hz. Those vortices interrupt the flow supply through the combustor, resulting in rigorous flame response and high FTF gain. The simulation domain is further expanded to the can-annular type complex gas turbine system. The combustion instabilities due to symmetric inlet condition and presence of a cross-talk area are investigated. Unstable combustion characteristics from the simulation show good agreement with the experiment. From the numerical work, the role of symmetry and a cross-talk area is clarified, and methods of attenuating instability are discussed. Meanwhile, the reduced-order solver is developed to study the ram-to-scram transition, which occurs due to the internal/external disturbance of the hypersonic

combustion system. The developed solver consists of a one-dimensional governing equation with combustion, mixing model, and mode-determining algorithm. Flight conditions and fuel mass flow rate are set up as variables in the solver. The simulation results show the increase in equivalence ratio causes the increase of thrust and the ram-to-scram mode transition. Also, the changes in air inflow speed and transition point are confirmed with the change in flight conditions. The present research contributes to the control of combustion instability and the operation and design of the combustion system.

Bibliography

Chapter 2

[1] IEA, Key World Energy Statistics 2021, (2021).

[2] G. Richards, M. McMillian, R. Gemmen, W. Rogers, S. Cully, Issues for low-emission, fuel-flexible power systems, Prog. Energy Combust. Sci. 27 (2001) 141-169.

[3] T. Lieuwen, V. McDonell, E. Petersen, D. Santavicca. Fuel flexibility influences on premixed combustor blowout, flashback, autoignition, and stability, J. Eng. Gas Turbines Power 130 (2008) 011506.

[4] G.W. Crabtree, M.S. Dresselhaus, The H_2 fuel alternative, MRS Bull. 33 (2008) 421-428.

[5] C.K. Law, O.C. Kwon, Effects of hydrocarbon substitution on atmospheric hydrogen-air flame propagation, Int. J. Hydrogen Energ. 29 (2004) 867-879.

[6] R.L. Speth, A.F. Ghoniem, Using a strained flame model to collapse dynamic mode data in a swirl-stabilized syngas combustor, Proc. Combust. Inst. 32 (2009) 2993-3000.

[7] H.S. Kim, V.K. Arghode, M.B. Linck, A.K. Gupta, Hydrogen addition effects in a confined swirl-stabilized methane-air flame, Int. J. Hydrogen Energ. 34 (2009) 1054-1062.

[8] S.R. Bell, M. Gupta, Extension of the lean operating limit for natural gas fueling of a spark ignited engine using hydrogen blending, Combust. Sci. Technol. 123 (1997) 23-48.

[9] R.W. Schefer, D.M. Wicksall, A.K. Agrawal, Combustion of hydrogen-enriched methane in a lean premixed swirl-stabilized combustor, Proc. Combust. Inst. 23 (2002) 843-851.

[10] S. Hong, S.J. Shanbhogue, A.F. Ghoniem, Impact of fuel composition on the recirculation zone structure and its role in lean premixed flame anchoring, Proc. Combust. Inst. 35 (2015) 1493-1500.

[11] F. Cozzi, A. Coghe, Behavior of hydrogen-enriched non-

premixed swirled natural gas flames, Int. J. Hydrogen Energ. 31 (2006) 669-677.

[12] M. Emadi, D. Karkow, T. Salameh, A. Gohil, A. Ratner, Flame structure changes resulting from hydrogen-enrichment and pressurization for low-swirl premixed methane-air flames, Int. J. Hydrogen Energ. 37 (2012) 10397-10404.

[13] R.W. Schefer, D.M. Wicksall, A.K. Agrawal, Combustion of H_2-enriched methane in a lean premixed swirl-stabilized combustor, Proc. Combust. Inst. 23 (2002) 843-851.

[14] E. Karlis, Y. Liu, Y. Hardalupas, A.M.K.P. Taylor, H_2 enrichment of CH_4 blends in lean premixed gas turbine combustion: An experimental study on effects on flame shape and thermoacoustic oscillation dynamics, Fuel 254 (2019) 115524.

[15] P.M. Allison, J.F. Driscoll, M. Ihme, Acoustic characterization of a partially-premixed gas turbine model combustor: Syngas and hydrocarbon fuel comparisons, Proc. Combust. Inst. 34 (2013) 3145-3153.

[16] M.C. Lee, J. Yoon, S. Joo, J. Kim, J. Hwang, Y. Yoon, Investigation into the cause of high multi-mode combustion instability of $H_2/CO/CH_4$ syngas in a partially premixed gas turbine model combustor, Proc. Combust. Inst. 35 (2015) 3263-3271.

[17] Z. Mansouri, M. Aouissi, T. Boushaki, Numerical computation of premixed propane flame in a swirl-stabilized burner: Effects of hydrogen enrichment, swirl number and equivalence ratio on flame characteristics, Int. J. Hydrogen Energ. 41 (2016) 9664-9678.

[18] F.E. Hernandez-perez, C.P.T. Groth, O.L. Gulder, Large-eddy simulation of lean hydrogen-methane turbulent premixed flames in the methane-dominated regime, Int. J. Hydrogen Energ. 39 (2014) 7147-7157.

[19] Y. Zheng, M. Zhu, D.M. Martinez, X. Jiang, Large-eddy simulations of mixing and combustion in a premixed swirling combustor with synthesis gases, Comput. Fluids 88 (2013) 702-714.

[20] E.R. Hawkes, J.H. Chen, Direct numerical simulation of hydrogen-enriched lean premixed methane-air flames, Combust.

Flame 138 (2004) 242-258.

[21] B. Franzelli, E. Riber, L.Y.M. Gicquel, T. Poinsot, Large Eddy Simulation of combustion instabilities in a lean partially premixed swirled flame, Combust. Flame 159 (2012) 621-637.

[22] X. Han, J. Li, A.S. Morgans, Prediction of combustion instability limit cycle oscillations by combining flame describing function simulations with a thermoacoustic network model, Combust. Flame 162 (2015) 3632-3647.

[23] C.Y. Lee, L.K.B. Li, M.P. Juniper, R.S. Cant, Nonlinear hydrodynamic and thermoacoustic oscillations of a bluff-body stabilized turbulent premixed flame, Combust. Theory Model. 20 (2015) 131-153.

[24] C. Kraus, L. Selle, T. Poinsot, Coupling heat transfer and large eddy simulation for combustion instability prediction in a swirl burner, Combust. Flame 191 (2018) 239-251.

[25] N. Zettervall, N.A. Worth, M. Mazur, J.R. Dawson, C. Fureby, Large eddy simulation of CH_4-air and C_2H_4-air combustion in a model annular gas turbine combustor, Proc. Combust. Inst. 37 (2019) 5223-5231.

[26] M. Boyce, Gas turbine engineering handbook. Elsevier, 2012.

[27] H.G. Weller, G. Taber, H. Jasak, C. Fureby, A tensorial approach to computational continuum mechanics using object-oriented techniques, Comput. Phys. 12 (1998) 620-631.

[28] S. Chapman, T.G. Cowling, The mathematical theory of non-uniform gases: an account of the kinetic theory of viscosity, thermal conduction and diffusion in gases, Cambridge: Cambridge University Press (1970).

[29] J.D. Anderson, Hypersonic and high temperature gas dynamics, Reston, VA: AIAA (2000).

[30] V. Novaresio, M. Garcia-Camprubi, S. Izquierdo, P. Asinari, N. Fueyo, An open-source library for the numerical modeling of mass-transfer in solid oxide fuel cells, Comput. Phys. Commun. 183 (2012) 125-146.

[31] F. Nicoud, F. Ducros. Subgrid-scale stress modelling based on the square of the velocity gradient tensor, Flow Turb. Combust. 62

(1999) 183-200.

[32] F.N. Egolfopoulos, P. Cho, C.K. Law, Laminar flame speeds of methane-air mixtures under reduced and elevated pressures, Combust. Flame 76 (1989) 375-391.

[33] V.I. Golovitchev, N. Nordin, R. Jarnicki, J. Chomiak, 3-D diesel spray simulations using a mew detailed chemistry turbulent combustion model, SAE Technical Paper, 2000.

[34] O.L. Gulder, Turbulent premixed flame propagation models for different combustion regimes, Proc. Combust. Inst. 23 (1990) 743-750.

[35] A.R. Kerstein, W.T. Ashurst, Propagation rate of growing interfaces in stirred fluids, Phys. Rev. Lett. 68 (1992) 934-937.

[36] H. Kolla, J.W. Rogerson, N. Swaminathan, Validation of a turbulent flame speed model across combustion regimes, Combust. Sci. Technol. 182 (2010) 284-308.

[37] J. Chomiak, K. Karlsson, Flame liftoff in diesel sprays, Proc. Combust. Inst. 26 (1996) 2557-2564.

[38] H.C. Yee, A class of high-resolution explicit and implicit shock-capturing methods, TM-101088, NASA Technical Reports, 1989.

[39] C.J. Dasch, One-dimensional tomography: a comparison of Abel, onion-peeling, and filtered back projection methods, Appl. Opt. 31 (1992) 1146-1152.

[40] J. Yoon, S. Joo, J. Kim, M.C. Lee, J.G. Lee, Y. Yoon, Effects of convection time on the high harmonic combustion instability in a partially premixed combustor, Proc. Combust. Inst. 36 (2017) 3753-3761.

[41] H.M. Altay, R.L. Speth, D.E. Hudgins, A.F. Ghoniem, Flame-vortex interaction driven combustion dynamics in a backward-facing step combustor, Combust. Flame 156 (2009) 1111-1125.

[42] A.M. Kypraiou, P.M. Allison, A.G.E. Mastorakos, Response of flames with different degrees of premixedness to acoustic oscillations, Combust. Sci. Technol. 190 (2018) 1426-1441.

[43] M.K. Kim, J. Yoon, J. Oh, J. Lee, Y. Yoon, An experimental study of fuel-air mixing section on unstable combustion in a dump

combustor, Appl. Therm. Eng. 62 (2014) 662-670.

[44] J. Nam, Y. Lee, S. Joo, Y. Yoon, J.J. Yoh, Numerical analysis of the effect of the hydrogen composition on a partially premixed gas turbine combustor, Int. J. Hydrogen Energ. 44 (2019) 6278-6286.

Chapter 3

[1] K.R. McManus, T. Poinsot, S. Candel, A review of active control of combustion instabilities, Proc. Energy. Combust. Sci. 19 (1993) 1-29.

[2] J.P. Moeck, J.F. Bourgouin, D. Durox, T. Schuler, S. Candel, Nonlinear interaction between a precessing vortex core and acoustic oscillations in a turbulent swirling flame, Combust. Flame 159 (2012) 2650-2668.

[3] H.M. Altay, R.L. Speth, D.E. Hudgins, A.F. Ghoniem, Flame-vortex interaction driven combustion dynamics in a backward-facing step combustor, Combust. Flame 156 (2009) 1111-1125.

[4] P.M. Allison, J.F.Driscoll, M.Ihme, Acoustic characterization of a partially-premixed gas turbine model combustor: Syngas and hydrocarbon fuel comparisons, Proc. Combust. Inst. 34 (2013) 3145-3153.

[5] T. Poinsot, Prediction and control of combustion instabilities in real engines, Proc. Combust. Inst. 36 (2017) 1-28.

[6] L. Crocco, Theoretical studies on liquid-propellant rocket instability, Proc. Combust. Inst. 10 (1968) 1101-1128.

[7] S. Hermeth, G. Staffelbach, L.Y.M. Gicquel, V. Anisimov, C. Cirigliano, T. Poinsot, Bistable swirled flames and influence on flame transfer functions, Combust. Flame 161 (2014) 184-196.

[8] F. Dupuy, M. Gatti, C. Mirat, L. Gicquel, F. Nicoud, T. Schuller, Combining analytical models and LES data to determine the transfer function from swirled premixed flames, Combust. Flame 217 (2020) 222-236.

[9] H.J. Krediet, C.H. Beck, W. Krebs, S. Schimek, C.O. Paschereit, J.B.W. Kok, Identification of the Flame Describing Function of a

Premixed Swirl Flame from LES, Combust. Sci. Technol. 184 (2012) 888-900.

[10] X. Han, J. Li, A.S. Morgans, Prediction of combustion instability limit cycle oscillations by combining flame describing function simulations with a thermoacoustic network model, Combust. Flame 162 (2015) 3632-3647.

[11] S. Joo, S. Kwak, J. Lee, Y. Yoon, Thermoacoustic instability and flame transfer function in a lean direct injection model gas turbine combustor, Aerosp. Sci. Technol. 116 (2021) 106872.

[12] J. Yoon, S. Joo, J. Kim, M.C. Lee, J.G. Lee, Y. Yoon, Effects of convection time on the high harmonic combustion instability in a partially premixed combustor, Proc. Combust. Inst. 36 (2017) 3753-3761.

[13] J. Yoon, S. Joo, J. Kim, M.C. Lee, J.G. Lee, Y. Yoon, A study of the flame transfer function characteristics using cold-flow transfer function in a partially premixed model gas turbine combustor, J. Korean Soc. Propuls. Eng. 21 (2017) 54-60.

[14] T.J. Poinsot, S.K. Lele, Boundary conditions for direct simulations of compressible viscous flows, J. Comput. Phys. 101 (1992) 104-129.

[15] F.N. Egolfopoulos, P. Cho, C.K. Law, Laminar Flame Speeds of Methane-Air Mixtures Under Reduced and Elevated Pressures, Combust. Flame 76 (1989) 375-391.

[16] F. Nicoud, F. Ducros, Subgrid-scale stress modelling based on the square of the velocity gradient tensor, Flow Turbul. Combust. 62 (1999) 183-200.

[17] S.M. Correa, Turbulence-Chemistry Interactions in the Intermediate Regime of Premixed Combustion, Combust. Flame 93 (1993) 41-60.

[18] H.G. Weller, G. Taber, H. Jasak, C. Fureby, A tensorial approach to computational continuum mechanics using object-oriented techniques, Comput. Phys. 12 (1998) 620-631.

[19] I.B. Celik, Z.N. Cehreli, I. Yavuz, Index of resolution quality for Large eddy simulation, J. Fluids Eng. 127 (2005) 949-958.

[20] M. Ismailov, S.D. Heister, Dynamic Response of Rocket Swirl

Injectors, Part I: Wave Reflection and Resonance, J. Propul. Power 27 (2011) 402-411.

[21] K.S. Kedia, H.M. Altay, A.F. Ghoniem, Impact of flame-wall interaction on premixed flame dynamics and transfer function characteristics, Combust. Flame 33 (2011) 1113-1120.

Chapter 4

[1] K.I. Matveev, F.E.C. Culick, A model for combustion instability involving vortex shedding, Combust. Sci. Technol. 175 (2003) 1059-1083.

[2] S. Hemchandra, S. Shanbhogue, S. Hong, A.F. Ghoniem, Role of hydrodynamic shear layer stability in driving combustion instability in a premixed propane-air backward-facing step combustor, Phys. Rev. Fluids. 3 (2018) 063201.

[3] S. Srinivasan, R. Ranjan, S. Menon, Flame dynamics during combustion instability in a high-pressure, shear-coaxial injector combustor, Flow. Turbul. Combust. 94 (2015) 237-262.

[4] M.K. Kim, J. Yoon, J. Oh, J. Lee, Y. Yoon, An experimental study of fuel-air mixing section on unstable combustion in a dump combustor, Appl. Therm. Eng. 62 (2014) 662-670.

[5] T.J. Poinsot, A.C. Trouve, D.P. Veynante, S.M. Candel, E.J. Esposito, Vortex-driven acoustically coupled combustion instabilities, J. Fluid Mech. 177 (1987) 265-292.

[6] T. Lieuwen, H. Torres, C. Johnson, B.T. Zinn, A mechanism of combustion instability in lean premixed gas turbine combustors, J. Eng. Gas Turb. Power 123 (2001) 182-189.

[7] J. Nam, J.J. Yoh, A numerical investigation of the effects of hydrogen addition on combustion instability inside a partially-premixed swirl combustor, Appl. Therm. Eng. 176 (2020) 115478.

[8] S. Taamallah, Z.A. LaBry, S.J. Shanbhogue, A.F. Ghoniem, Thermo-acoustic instabilities in lean premixed swirl-stabilized combustion and their link to acoustically coupled and decoupled flame macrostructures, Proc. Combust. Inst. 35 (2015) 3273-3282.

[9] Y. Huang, V. Yang, Effect of swirl on combustion dynamics in a lean-premixed swirl-stabilized combustor, Proc. Combust. Inst. 30 (2005) 1775-1782.

[10] K.T. Kim, Combustion instability feedback mechanism in a lean-premixed swirl-stabilized combustor, Combust. Flame 171 (2016) 137-151.

[11] G. Ghirardo, C.D. Giovine, J.P. Moeck, M.R. Bothien, Thermoacoustics of can-annular combustors, J. Eng. Gas Turb. Power 141 (2019) 011007.

[12] K. Moon, H. Jegal, J. Gu, K.T. Kim, Combustion-acoustic interactions through cross-talk area between adjacent model gas turbine combustor, Combust. Flame 202 (2019) 405-416.

[13] G.Ghirardo, J.P. Moeck, M.R. Bothien, Effect of noise and nonlinearities on thermoacoustics of can-annular combustors, J. Eng. Gas Turb. Power 142 (2020) 041005.

[14] F. Farisco, L. Panek, J.B.W. Kok, Thermo-acoustic cross-talk between cans in a can-annular combustor, Int. J. Spray Combust. Dynamics 9 (2017) 452-469.

[15] N. Thomas, S. Mondal, S.A. Pawar, R.I. Sujith, Effect of noise amplification during the transition to amplitude death in coupled thermoacoustic oscillators, Chaos 28 (2018), 093116.

[16] B. Franzelli, E. Riber, L.Y.M. Gicquel, T. Poinsot, Large eddy simulation of combustion instabilities in a lean partially premixed swirled flame, Combust. Flame 159 (2012) 621-637.

[17] J.M. Lourier, M. Stohr, B. Noll, S. Werner, A. Fiolitakis, Scale adaptive simulation of a thermoacoustic instability in a partially premixed lean swirl combustor, Combust. Flame 183 (2017) 343-357.

[18] C. Kraus, L. Selle, T. Poinsot, Coupling heat transfer and large eddy simulation for combustion instability prediction in a swirl burner, Combust. Flame 191 (2018) 239-251.

[19] Z.X. Chen, I. Langella, N. Swaminathan, M. Stohr, W. Meier, H. Kolla, Large eddy simulation of a dual swirl gas turbine combustor: Flame/flow structures and stabilization under thermoacoustically stable and unstable conditions, Combust. Flame 203 (2019) 279-

300.

[20] D. Noh, E. Karlis, S. Navarro-Martinez, Y. Hardalupas, A.M.K.P. Taylor, D. Fredrich, W.P. Jones, Azimuthally-driven subharmonic thermoacoustic instabilities in a swirl-stabilized combustor, Proc. Combust. Inst. 37 (2019) 5333-5341.

[21] N. Zettervall, N.A. Worth, M. Mazur, J.R. Dawson, C. Fureby, Large eddy simulation of CH_4–air and H_2–air combustion in a model annular gas turbine combustor, Proc. Combust. Inst. 37 (2019) 5223-5231.

[22] E.L. Schiavo, D. Laera, E. Riber, L. Gicquel, T. Poinsot, Effects of liquid fuel/wall interaction on thermoacoustic instabilities in swirling spray flames, Combust. Flame 219 (2020) 86-101.

[23] F. Nicoud, F. Ducros, Subgrid-scale stress modelling based on the square of the velocity gradient tensor, Flow. Turbul. Combust. 62 (1999) 183-200.

[24] F.N. Egolfopoulos, P. Cho, C.K. Law, Laminar flame speeds of methane-air mixtures under reduced and elevated pressures, Combust. Flame 76 (1989) 375-391.

[25] J. Chomiak, A. Karlsson, Flame liftoff in diesel sprays, Proc. Combust. Inst. 26 (1996) 2557-2564.

[26] A. Sandu, J. Verwer, J. Blom, E. Spee, G. Carmichael, F. Potra, Benchmarking stiff ode solvers for atmospheric chemistry problems II: Rosenbrock solvers, Atmos. Environ. 31 (1997) 3459-3472.

[27] P. Palies, T. Schuller, D. Durox, L.Y.M. Gicquel, S. Candel, Acoustically perturbed turbulent premixed swirling flames, Phys. Fluids 23 (2011) 037101.

[28] D.G. Goodwin, R.L. Speth, H.K. Moffat, B.W. Weber, Cantera: An object-oriented software toolkit for chemical kinetics, thermodynamics, and transport processes, https://www.cantera.org, 2018, Version 2.4.0.

[29] H. Jegal, J. Gu, L.K.B. Li, K.T. Kim, Influence of asymmetric flame transfer functions on can-to-can acoustic interactions between two lean-premixed combustors, Proc. Combust. Inst. 38 (2021) 6051-6058.

[30] V. Bellucci, B. Schuermans, D. Nowaks, P. Flohr, C.O.

Paschereit, Thermoacoustic modeling of a gas turbine combustor equipped with acoustic dampers, J. Turbomach. 127 (2005) 372−379.

Chapter 5

[1] M. Berglund, C. Fureby, LES of supersonic combustion in a scramjet engine model, Proc. Combust. Inst. 31 (2007) 2497−2504.
[2] K. Nordin−Bates, C. Fureby, S. Karl, K. Hannemann, Understanding scramjet combustion using LES of the HyShot II combustor, Proc. Combust. Inst. 36 (2017) 2893−2900.
[3] T. Nilsson, S. Zhong, C. Fureby, LES of H2−air jet combustion in high enthalpy supersonic crossflow, Phys. Fluids 33 (2021) 035133.
[4] T.F. O'Brien, R.P. Starkey, M.J. Lewis, Quasi−one−dimensional high−speed engine model with finite−rate chemistry, J. Propul. Power 17 (2001) 1366−1374.
[5] S.M. Torrez, J.F. Driscoll, M. Ihme, M.L. Fotia, Reduced−order modeling of turbulent reacting flows with application to ramjets and scramjets, J. Propul. Power 27 (2011) 371−382.
[6] C. Birzer, C.J. Doolan, Quasi−one−dimensional model of hydrogen−fueled scramjet combustors, J. Propul. Power 25 (2009) 1220−1225.
[7] E. Hairer, G. Wanner, Solving ordinary differential equations II: Stiff and differential−algebraic problem, Springer, New York (1996).
[8] P. Saxena, F.A. Williams, Testing a small detailed chemical−kinetic mechanism for the combustion of hydrogen and carbon monoxide, Combust. Flame 145 (2006) 316−323.
[9] T. Ikui, K. Matsuo, M. Nagai, The mechanism of pseudo−shock waves, Bulletin of JSME 17 (1974) 731−739.
[10] A.H. Shapiro, Dynamics and thermodynamics of compressible fluid flow, Ronald, New York (1953).

Abstract

본 연구에서는 연소기 내부에서 발생하는 불안정성의 원인을 규명하기 위하여 다양한 연소시스템에 대한 수치해석적 연구를 수행하였다. 부분예혼합 가스터빈 연소기, 다중 예혼합 가스터빈 연소기, 이중모드 스크램제트 연소기를 포함한 세 가지 종류의 연소기가 해석을 위해 고려되었다. 가스터빈 연소기 내에서 발생하는 난류 화염을 모사하기 위하여 대와류모사(LES) 기법을 활용한 해석이 수행되었으며, 이중모드 스크램제트 연소기의 해석을 위하여 근사적인 해석 기법이 개발되었다.

부분예혼합 연소기에서 발생한 불안정의 원인으로서 연료 내 수소 함량의 영향이 집중적으로 연구되었다. 가스터빈 내 수소가 포함된 선회 화염의 해석을 위하여 LES 난류 모델 및 유한화학반응 모델, 난류-연소 연계 모델이 솔버 내에 적용되었다. 세 종류의 수소 조성이 고려되었으며, 이에 따른 화염구조 및 연소불안정의 변화가 조사되었다. 해석 결과의 검증을 위하여 과거 실험 결과와의 대조를 통한 검증이 수행되었으며, 높은 일치도가 확인되었다. 해석 결과로부터 수소 조성의 변화에 따른 화염 구조의 급격한 변화가 확인되었다. 구체적으로, 수소 함량의 증가에 따라, 수소의 빠른 연소 속도로 짧은 선회 화염이 연소기 내에 나타났다. 또한, 특정 수소 조정에서는 강력한 연소불안정이 발생하였으며 이에 따른 불안정한 화염이 확인되었다. 이와 같은 경우, 벽면 주변의 재순환 영역으로 부분예혼합 유동의 주기적인 공급이 일어났으며, 이에 따른 화염-와류 연계현상이 확인되었다. 반면, 수소 조성이 변화하거나 연료 유량이 감소하였을 경우 화염 구조가 변화하였으며, 이에 따라 화염-와류 연계현상이 일어나지 않았고 연소불안정이 감쇠되었음이 확인되었다. 이와 같은 결과로부터, 선회 화염구조의 변화 및 재순환 영역과의 연계가 연소불안정 발생에 있어 주요한 요인이 되었음을 확인할 수 있다.

동일 연소기에 대한 추가적인 해석이 완전 예혼합 조건에서 수행되었으며 예혼합도 및 당량비 섭동의 영향이 조사되었다. 해석 결과에 따르면,

예혼합 조건으로 변경 시 수소 조성이 화염 구조에 상대적으로 적은 영향을 가하는 것이 확인되었다. 또한, 달라진 화염 구조 및 분사 조건이 연소불안정 특성을 변화시켰음이 확인되었다. 부분예혼합 연소기 내 연료-공기 혼합 구간에서는 당량비의 섭동이 확인되었으며 해당 섭동 주파수 분포는 연소불안정과 동일하게 나타났다. 이와 같은 당량비의 섭동 현상은 연소불안정 발생의 주요 원인이 되는 화염 구조의 섭동을 야기한다. 당량비의 섭동 현상은 예혼합 연소 조건에서는 발생할 수 없으며, 이에 따라 예혼합 연소기 내부에서는 연소불안정이 확인되지 않았다. 이로부터 수소 조성 및 혼합 조건의 두 요인이 연소불안정 발생 원인이 되었으며, 가스터빈 작동에 있어 고려되어야 함을 확인할 수 있었다.

이어서 수행된 연소기 내 화염응답함수(FTF) 및 비연소 전달함수(CTF)의 해석은 연소공급계 내부에서 나타나는 불안정이 부분예혼합 선회화염 응답 특성의 원인이 되었음을 규명하였다. FTF 해석을 위해 외부 가진을 준 경계 조건이 연소기 입구에 고려되었으며, 50 Hz 부터 400 Hz 까지의 가진 주파수가 설정되었다. 해석 결과로부터, 특정 가진 주파수에서 FTF 및 CTF 함수의 강한 응답이 나타났음이 확인되었다. 구체적으로, 스월러 형상으로 인하여 스월러 입구 주변에 와류가 발생하였고, 이 와류는 공급 라인의 난류로 인하여 생성과 소산을 반복하였음이 확인되었다. 생성된 와류들은 스월러로의 유동 공급을 방해하였으며 이로 인해 연소기로의 유동 공급 섭동이 나타났다. 와류의 섭동 주파수는 강한 화염응답이 나타난 주파수와 일치하였으며, 이로부터 연료공급계 내부 불안정이 화염응답의 주요 원인이 되었음을 알 수 있다. 이와 같은 FTF 및 CTF 해석 결과는 실험 결과와 검증되었고 높은 신뢰성이 확인되었다.

이어서, 두개의 예혼합 연소기 및 크로스톡 영역으로 이루어진 대형 가스터빈 연소시스템에 대한 연소불안정 해석이 수행되었으며, 이로부터 연소불안정에 대한 연소기 간의 연계 현상이 조사되었다. 두 연소기의 입력조건이 대칭인 조건 및 비대칭인 조건에서 해석이 수행되었고 이와 같은 대칭 현상이 화염 섭동 및 연소불안정 모드에 주는 영향을 확인하

고자 하였다. 대칭 입구 조건에서는 연소기 축방향에서 나타난 연소불안정이 화염 섭동을 야기하였으며, 연소시스템 내에는 두 연소기의 불안정 위상이 서로 동일한 push-push 모드가 나타났다. 비대칭 해석 조건에서는 연소불안정과 반대되는 위상의 섭동이 하나의 연소기에 추가적으로 입력되었고, 이로부터 크로스톡 영역을 통한 전체 연소시스템에서의 연소불안정 억제가 확인되었다.

추가적으로, 이중모드 스크램제트 연소기의 설계 및 내부 불안정 분석을 위하여 일차원 연소해석 솔버가 개발되었다. 개발된 솔버는 일차원 지배방정식을 바탕으로 하여 구축되었고 연소, 혼합, 램제트-스크램제트 모드 천이에 대한 근사적인 모델을 포함하였다. 솔버의 입력조건으로서 비행임무조건이 설정되었고, 계산을 통하여 유동 분포, 추력, 열질식 위치에 대한 정보들이 해석되었다. 해석으로부터 입력 당량비 및 비행임무조건에 따른 모드 천이 현상과 추력의 변화가 확인되었다. 초기온도에 따른 점화지연시간 해석을 통하여 솔버의 검증을 수행하였으며, 실험 결과와의 검증이 향후 계획되고 있다.

주요어: 연소불안정, 대와류모사, 난류 연소, 수소, 가스터빈 연소기, 스크램제트 연소기

학번: 2017-25866